
Electronic Thesis and Dissertation Repository

1-11-2018 9:30 AM

Syngas Chemical Looping Combustion Using A Fluidizable Oxygen Carrier: Reactivity, Kinetics, Reactor Simulation

Imtiaz Ahmed, *The University of Western Ontario*

Supervisor: de Lasa, Hugo I., *The University of Western Ontario*

A thesis submitted in partial fulfillment of the requirements for the Doctor of Philosophy degree
in Chemical and Biochemical Engineering

© Imtiaz Ahmed 2018

Follow this and additional works at: <https://ir.lib.uwo.ca/etd>

 Part of the [Catalysis and Reaction Engineering Commons](#)

Recommended Citation

Ahmed, Imtiaz, "Syngas Chemical Looping Combustion Using A Fluidizable Oxygen Carrier: Reactivity, Kinetics, Reactor Simulation" (2018). *Electronic Thesis and Dissertation Repository*. 5990.
<https://ir.lib.uwo.ca/etd/5990>

This Dissertation/Thesis is brought to you for free and open access by Scholarship@Western. It has been accepted for inclusion in Electronic Thesis and Dissertation Repository by an authorized administrator of Scholarship@Western. For more information, please contact wlsadmin@uwo.ca.

ABSTRACT

Biomass gasification yields a blend of H_2 , CO , CH_4 and CO_2 , designated as syngas. Syngas can be further combusted using fluidizable oxygen carriers (OCs) during power generation via Chemical Looping Combustion (CLC). To improve syngas CLC and establish its application, a new Ni-based oxygen carrier with a Co and La modified $\gamma-Al_2O_3$ support was studied. This type of OC considerably limits the $NiAl_2O_4$ formation. Therefore, the oxygen carrier was engineered using a special preparation methodology to eliminate $NiAl_2O_4$ species formation. This promising Highly Performing Oxygen Carrier (HPOC) was characterized using XRD, BET, H_2 -TPR, NH_3 -TPD and pulse chemisorption.

Isothermal CLC runs were carried out in the CREC Riser Simulator which is a novel mini-batch fluidized bed reactor. A computational fluid dynamics (CFD) simulation was developed using the COMSOL Multiphysics® module to analyse gas-solid mixing patterns in the CREC Riser Simulator. This CFD model allowed to calculate the axial and circumferential gas velocities, the pressure changes and the geometrical modifications required in the reactor.

Reactivity runs using the CREC Riser Simulator, were developed as follows: a) 2-40s reaction times, b) 550-650°C, c) H_2/CO ratios at 2.5 and 1.33 and d) 0.5 and 1 fuel to HPOC oxygen stoichiometric ratios. Encouraging results were obtained employing a 2.5 H_2/CO ratio with a 92% CO_2 yield and 90% CO , 95% H_2 and 91% CH_4 conversions. As well, the HPOC showed an oxygen transport capacity in the 1.84-3.0 wt% (gO_2/gOC) range, with a 40-70% oxygen conversion.

A thermodynamic based model was established to predict the CLC syngas conversion limits. Additionally, a kinetic model was proposed for syngas CLC using the HPOC. This solid state kinetics considers a Nucleation and a Nuclei Growth Model (NNGM). This kinetics led to a ten intrinsic kinetic parameter model. These parameters were determined via numerical regression within a 95% confidence interval and with small cross-correlation coefficients. As a result, the kinetic rate constants showed that the reactivity of the syngas species could be expressed following the $H_2 > CO > CH_4$ order.

Given the high performance and stability of the developed HPOC and the successful established kinetics, a computational particle fluid dynamics (CPFD) simulation for a 100kW CLC facility was developed. This simulation used a hybrid Barracuda VR CPFD model featuring “single particles” and “clustered particles”. According to the simulated CLC performance, it is anticipated that 90% CO₂ yields can be achieved as follows: a) in a 25-m length downer unit simulated using the “single particle” model, b) in a 30-m downer unit simulated with the “clustered particles” model. Furthermore, it was observed that a L-type loop seal with air-pulse system eliminates the CO₂ gas leakage, which usually occurs when the syngas moves from the fuel reactor to the air reactor.

Keywords: Chemical Looping Combustion, Syngas, Nickel Oxide, Nickel Aluminate, Negative CO₂ emission, CREC Riser Simulator, Kinetic Modelling, Reactor Simulation.

Dedication

This dissertation is dedicated to:

My Mother (Mahmuda Akther)

and

My Father (Md. Fazlul Hoque)

উৎসর্গ করলাম আমার আশু ও আবু কে

ACKNOWLEDGMENTS

By the blessing of Almighty Allah, I have successfully completed my PhD dissertation in due time at University of Western Ontario (UWO). I would like to express my sincere appreciation to all who supported me to achieve the successful accomplishment.

At first, I would like to express my endless gratitude to my advisor Dr. Hugo I. de Lasa for providing me the opportunity on a challenging project at Chemical Reactor Engineering Center (CREC), UWO. His knowledge, encouragement, technical discussion, and hardworking highly motivated me to enrich my research journey. I am also thankful to the financial support provided by the NSERC-Canada Strategic grant program (2015-H. de Lasa grant) and RECAT Technologies Inc. at the UWO.

I am thankful to Dr. Rezwanul Quddus, Dr. Jahirul Mazumder, Dr. Angel Lanza for making me knowledgeable in dealing with my research activities. Special thanks to my wife and also my colleague Dr. Samira Rostom who always supported me with her love, appreciation and patience. Her critical reviews to my research and technical advices made this dissertation successful. Also, I am glad to Cesar Medina and Nicolas Torres, for their valuable advice and support regarding particle fluidization and CPFD Software.

I am thankful to Florencia de Lasa for her valuable assistance in the editing of this manuscript. My gratefulness go to Jose Munoz and Pastor Solano for assisting and advising me to solve several technical issues in CREC Laboratory. I am indebted to all of my colleagues and friends for providing inspirations and supports. Special thanks to Souheil Afara for the anytime coffee that kept me alive during research.

At the end profound gratitude goes to my parents, sister and family members in my home country Bangladesh for their kind supports, encouragement and prayers. I wish them all for a long and happy life.

Imtiaz Ahmed

December 2018

Table of Contents

ABSTRACT.....	i
ACKNOWLEDGMENTS	iv
LIST OF TABLES	ix
LIST OF FIGURES	ix
CHAPTER 1 LITERATURE REVIEW	1
1.1 Introduction.....	1
1.2 Chemical Looping Combustion (CLC).....	2
1.3 Thermodynamic Efficiency of CLC Process	3
1.4 Oxygen Carrier Requirements	5
1.5 Syngas CLC	7
1.6 Novel Tool for CLC Studies	8
1.7 CLC Reaction Network.....	10
1.8 Thermodynamic Limit of Syngas CLC and Ni-based OC.....	11
1.9 Kinetic Modeling of CLC System	13
1.10 Large Scale and Demonstration Unit Simulation	16
1.11 Conclusions.....	18
CHAPTER 2 SCOPE OF RESEARCH.....	19
2.1 Specific Objectives	19
2.1.1 CFD Simulation of Novel CREC Riser Simulator: Mixing Patterns.....	19
2.1.2 Enhanced Oxygen Carriers: Preparation, Characterization	19
2.1.3 CLC performance using Syngas and Highly Performing Oxygen Carrier	19
2.1.4 CLC using Syngas: Detailed Reaction Mechanism and Kinetic Modelling	20
2.1.5 CPFD Barracuda Simulation of Large Demonstration Scale Air-Fuel Reactors.....	20
2.2 Accomplishments of Research Objectives.....	20
CHAPTER 3 EXPERIMENTAL METHODOLOGY	22
3.1 Introduction.....	22
3.2 Method of Oxygen Carrier Preparation	22
3.3 Temperature-Programmed Reduction (TPR) and Oxidation (TPO).....	23
3.4 H ₂ Pulse Chemisorption.....	23

3.5	Temperature-Programmed Desorption (TPD)	24
3.6	Surface Area and Pore Size Distribution	25
3.7	X-ray Diffraction (XRD)	25
3.8	CREC Riser Simulator for Oxygen Carrier Evaluation	25
3.8.1	Reactor Preparation for Reaction	27
3.8.2	Performing Reaction	27
3.8.3	Product Analysis System	28
3.8.3.1	Sample Analysis	28
3.8.3.2	Post-Analysis Calculations	28
3.9	Conclusions	29
CHAPTER 4	CFD MODEL FOR CREC RISER SIMULATOR	30
4.1	Introduction	30
4.2	Modeling Strategy	30
4.2.1	Gas and Solid Phases Considered	30
4.2.2	Geometry Considerations	30
4.2.3	Geometry Considerations	31
4.2.4	Model Development	31
4.2.4.1	Laminar Flow Model-Navier Stokes Equation	32
4.2.4.2	Turbulent Flow Model-Navier Stokes Equation	33
4.2.4.3	Flow through the Basket Grids and Particle Bed	33
4.3	Initial Values and Boundary Conditions	34
4.3.1	Initial Values for Computations	34
4.3.2	Boundary Conditions	35
4.3.2.1	Laminar Flow Model	35
4.3.2.2	Turbulent Flow Model	35
4.4	Numerical Approach	37
4.4.1	Computational Tools	37
4.4.2	Rotating Machinery Problem	37
4.4.3	Symmetric Geometry	38
4.4.4	Mesh Selection	39
4.4.5	Numerical Solution Strategy	40

4.5	Mesh Independence and Model Verification	40
4.6	Results and Discussion	42
4.6.1	Mixing Patterns	42
4.6.2	Velocity and Pressure Profiles	44
4.6.3	Impeller Rotation with Loaded Particles	45
4.6.4	High Temperature Effect on Mixing Pattern	46
4.7	Conclusions	47
CHAPTER 5	OXYGEN CARRIER DEVELOPMENT AND SYNGAS CLC	49
5.1	Oxygen Carrier for Syngas	49
5.1.1	Preparation of the OC of Reference (OC-Ref)	50
5.1.2	Preparation of the Fluidizable HPOC	51
5.1.3	Characterization of OC-Ref and HPOC	52
5.1.4	Stability of the HPOC	56
5.2	Syngas CLC Test Using CREC Riser Simulator	57
5.2.1	Syngas source and composition	57
5.2.2	Pressure profile of Syngas CLC	57
5.2.3	Effect of ψ ratio and temperature	58
5.2.3.1	Syngas-250 ($H_2/CO=2.5$)	58
5.2.3.2	Syngas-133 ($H_2/CO=1.33$)	62
5.2.4	Coke deposition	64
5.3	Conclusion	64
CHAPTER 6	KINETIC MODELLING	66
6.1	Rate Limiting Steps	67
6.2	Thermodynamic Equilibrium Analysis	69
6.3	Kinetic Model Assumptions	71
6.4	Kinetic Model Development	73
6.5	Numerical Method Used	75
6.6	Results and Discussions	76
6.6.1	Estimated Kinetic Parameters	76
6.6.2	Model Verification and Validation	79
6.7	Conclusions	82

CHAPTER 7	LARGE AND DEMONSTRATION SCALE SIMULATION	83
7.1	Materials and Methods.....	83
7.1.1	CLC Riser and Downer System.....	83
7.1.2	Oxygen Carrier Particle	85
7.1.3	Particle and Fluid Dynamic Models	86
7.1.4	Reaction Kinetic Model Used.....	88
7.1.5	Geometry Consideration	89
7.1.6	Initial and Boundary Conditions.....	91
7.1.7	Numerical Approach.....	92
7.2	Simulation Results and Discussion.....	93
7.2.1	Solid Circulation and Loop Seal	93
7.2.2	Pressure Profiles.....	95
7.2.3	Velocity Profiles and Volume Fraction	96
7.2.4	Simulated Reaction Analysis	98
7.3	Conclusions.....	102
CHAPTER 8	CONCLUSIONS AND RECOMMENDATIONS.....	103
8.1	Conclusions.....	103
8.2	Recommendations.....	104
NOMENCLATURE		105
REFERENCES		109
APPENDICES		121
Appendix A	Gas Chromatograph (GC) and Mass Balance	121
Appendix B	Oxygen Carrier (OC) Preparation Equipment.....	125
CURRICULUM VITAE.....		128

LIST OF TABLES

Table 1-1: Summary of Syngas CLC with a Nickel-Based Oxygen Carrier [5]	8
Table 1-2: Reported Kinetic Parameters for Reduction and Oxidation using Ni-based Oxygen Carriers and a Gaseous Fuel	14
Table 1-3: Summary of the Different Reactor Sizes and Configurations [78]	16
Table 1-4: A Summary of Recent Work on Large-Scale Simulations Using the CLC Process [5]	17
Table 4-1: Mesh Parameters for Different Configurations	39
Table 5-1: Characterization of γ -Al ₂ O ₃ , OC-Ref and HPOC	53
Table 6-1: Parameters Used to Determine the Negligible External and Internal Mass Transfer Limitations for the HPOC of the Present Study.....	69
Table 6-2: Kinetic Parameters Determined for Syngas-250 and Syngas-133, Separately	76
Table 6-3: Summary of Apparent Intrinsic Kinetic Parameters for the Proposed Kinetic Model and Cross-correlation Matrix	79
Table 7-1: Physical Properties of HPOC Particles	85
Table 7-2: Kinetic Parameters Applied in CLC Large Scale Simulation	89

LIST OF FIGURES

Figure 1-1: Schematic diagram of typical Chemical Looping Combustion process	3
Figure 1-2: Schematic Diagram of an Ideal CLC System for Power Production [10]	4
Figure 1-3: Equilibrium Constant as a Function of Temperature	13
Figure 3-1: Schematic Diagram of CREC Riser Simulator: a) Reactor system showing CLC application and b) Catalyst/oxygen carrier basket (<i>4PV: four-port valve, 6PV: six-port valve, MFC: mass flow controller</i>).....	26
Figure 3-2: Schematic Flow Diagram of Product Analysis System	28
Figure 4-1: Geometry Considerations for the CREC Riser Simulator Modeling.....	31
Figure 4-2: Computational Domains: a. Rotary fluid domain, b. Stationary fluid domain.	37
Figure 4-3: Symmetry Selection for Reactor “Slices”	38
Figure 4-4: Typical Mesh Pattern Indicating Boundary Layer Mesh	39

Figure 4-5: Mass Balance Established on the Basis of the % Difference of the Surface Integrated Mass Flow Rates for: a) Downward axial flow (annular outlet section) and b) Upward axial flow upflow inner reactor (basket).	40
Figure 4-6: Comparison of Experimental Axial Velocity (Original Configuration) and Model Axial Velocity inside the Catalyst Basket	42
Figure 4-7: CREC Riser Simulator Mixing Patterns at 4200 rpm for Air at 25° C and 1 atm a) Original Configuration (with vertical baffles with grids) b) Proposed Configuration (Without vertical baffles with grids)	42
Figure 4-8: Simulated Average Axial Velocity inside the Catalyst Basket.....	43
Figure 4-9: Velocity Profile inside the Catalyst Basket for Air at 25° C and 1 atm a) “Original Configuration b) New “Proposed Configuration”	44
Figure 4-10: Pressure Field and Velocity Magnitude of the new “Proposed” Configuration (“without vertical baffles with grids”) at 4200 RPM with air at 25° C and 1 atm.	45
Figure 4-11: Changes of Pressure Drop with RPM in the New “Proposed” CREC Riser Simulator Unit.	46
Figure 4-12: Mixing Patterns at 4200 rpm for Different Temperatures in the new "Proposed Configuration. a) 25° C, 1 atm b) 500° C,1 atm c) 500° C, 2 atm.....	46
Figure 5-1: H ₂ -TPR Profiles for the HPOC and the Oxygen Carrier used as the Reference (OC-Ref). Operating conditions: 10% H ₂ -Ar, 50 cm ³ /min., and a temperature ramp of 15°C/min up to desired level with 10 min. holding time.....	52
Figure 5-2: XRD Patterns for the HPOC and the OC-Ref under Oxidized State Conditions. The dotted line represents signal baseline.....	53
Figure 5-3: Nitrogen (N ₂) Adsorption–Desorption Isotherms for HPOC, OC-Ref and γ -Al ₂ O ₃ . All data are in the same linear scale with a shifted baseline.....	54
Figure 5-4: Pore Size Distribution (PSD) of the HPOC, the OC-Ref and the γ -Al ₂ O ₃ Support Determined by the BJH Desorption Pore Volume.....	55
Figure 5-5: NH ₃ -TPD Profiles of the HPOC, the OC-Ref and the γ -Al ₂ O ₃ support. Notes: a) NH ₃ was adsorbed at 100°C, b) NH ₃ was desorbed at 20°C/min heating rate.	55
Figure 5-6: Consecutive TPR/TPO Cycles using the HPOC at 15°C/min heating rate with a flow rate 50 cm ³ /min. (a) TPR: 10 vol.% H ₂ /Ar as a reducing agent (b) TPO: 5 vol.% O ₂ /He as an oxidizing agent.....	56

Figure 5-7: Pressure Profile in CREC Riser Simulator: Reactivity Test with HPOC and Syngas.	57
Figure 5-8: CO ₂ Yield from a Syngas-250 CLC Reaction at 600° C for $\psi=0.5$ and $\psi=1$. Reported data corresponds to at least 3 repeats with vertical bars showing standard deviations.....	59
Figure 5-9: OC oxygen conversion at 600° C for $\psi=0.5$ and $\psi=1$. Reported data corresponds to at least 3 repeats with vertical bars showing standard deviations.....	59
Figure 5-10: Syngas-250 Conversion (CO, H ₂ and CH ₄) at 600° C for $\psi=0.5$ and $\psi=1$. Reported data corresponds to at least 3 repeats with vertical bars showing standard deviations.....	60
Figure 5-11: Temperature Effect on CO ₂ Yield and OC oxygen conversion for $\psi=0.5$ Reported data corresponds to at least 3 repeats with vertical bars showing standard deviations.....	61
Figure 5-12: Temperature Effect on Syngas Conversion (CO, H ₂ and CH ₄) for $\psi=0.5$. Reported data corresponds to at least 3 repeats with vertical bars showing standard deviations.....	61
Figure 5-13: CO ₂ yield and OC oxygen conversion at different temperatures and with ψ for Syngas-133. Reported data corresponds to at least three repeats with vertical bars showing standard deviations.....	62
Figure 5-14: Comparison between the CO ₂ yield and OC oxygen conversion for syngas-250 and syngas-133 at 650°C. Reported data corresponds to at least three repeats with vertical bars showing standard deviations. Note: CO ₂ yields and the OC oxygen conversion of Syngas-250 are from [117].	63
Figure 5-15: Syngas-133 conversion by CO, H ₂ and CH ₄ at three temperatures (550, 600 and 650 °C), and 0.5 and 1 ψ ratios. Reported data corresponds to at least 3 repeats with vertical bars showing standard deviations.	63
Figure 6-1: Schematic Diagram Illustrating the Value of CREC Riser Simulator Experiments for the Development of a Kinetic Model Applicable in a Downer Reactor Unit.	67
Figure 6-2: Equilibrium dry gas composition of NiO-Syngas system at 1 atm (a) CO and H ₂ vol% (b) CO ₂ , CH ₄ and Coke mole % (Syngas: 20% CO, 10% CH ₄ , 20% CO ₂ , 50% H ₂ by mol)	70
Figure 6-3 : Comparison of change in equilibrium amount of compounds by temperatures.	70
Figure 6-4: Description of the Reaction Mechanism on the HPOC Surface describing various interaction of H ₂ , CO and CH ₄ with OC oxygen lattice	72

Figure 6-5: Parity Plot Comparing Experimental Chemical Species Partial Pressures with Model Predictions using Syngas-250 and HPOC. Data: 250 average data points for at least 3 repeats runs. Note: Standard Deviation=2.9%.	77
Figure 6-6: Parity Plot Comparing Experimental Chemical Species Partial Pressures with Model Predictions using Syngas-133 and HPOC. Data: 250 average data points for at least 3 repeats runs. Note: Standard Deviation=3.9%.	77
Figure 6-7: Comparison of Experimental Chemical Species Partial Pressures with those of Model Predictions at Various Conditions using the Syngas-250 Feed and a HPOC.	78
Figure 6-8: Comparison of Experimental Chemical Species Partial Pressures with those of Model Predictions at Various Conditions using Syngas-133 Feed and a HPOC	78
Figure 6-9: Parity Plot Comparing the Experimental Chemical Species Partial Pressures with Model Predictions for both Syngas-250 and Syngas-133. Data base: 500 averaged data points for at least 3 repeat runs. Note: Standard Deviation=5.4%.	80
Figure 6-10: Comparison of Experimental Data and Model Predictions using the HPOC of this Study and Syngas-250. Note: Parameters estimated use both Syngas-250 and Syngas-133 data.	81
Figure 6-11: Comparison of Experimental Data and Model Predictions using the HPOC of this Study and Syngas-133. Note: Parameters estimated use both Syngas-250 and Syngas-133 data.	81
Figure 7-1: Schematic Diagram of an Air Reactor (Riser) and Fuel Reactor (Downer) Considered in the Present Study for CLC Simulation	84
Figure 7-2: HPOC Particle Size Distribution.....	85
Figure 7-3: Clustered Particle Information: a) Distribution of number of particles in clusters for a gas velocity of 1.5 m/s and a particle mass flux 50 kg/m ² /s [86] b) Expressed as cluster size distribution (cluster sphericity 0.64).	86
Figure 7-4: Geometrical Characteristics of the Proposed Syngas CLC System	90
Figure 7-5: Schematic Diagram of a CLC Riser-Downer Configuration Indicating Boundary Conditions (BC)	91
Figure 7-6: Typical Computational Mesh Pattern: a) Upper part of the CLC system b) Lower part of the CLC system	93
Figure 7-7: Simulated HPOC Circulation in the CLC: a) Particle volume fractions in various unit locations, b) HPOC flow rates at various simulation times, c) HPOC mass fluxes through the	

reactors at various simulation times. Notes: i) Data or solid circulation reported using a 1 second averaging , ii) Dotted line shows a logarithm variation of both mass flow and mass flux.....	94
Figure 7-8: Pressure Levels at Different Locations of the CLC Process	96
Figure 7-9: (a) Radial Gas and Particle Velocity Profiles and (b) Radial Particle Volume Fractions in the CLC Downer Unit using the “Single Particle” Model . Note: Observation times during downer operation were 1s, 2s, 3s.....	97
Figure 7-10: Axial Fluid and Particle Velocities along the Fuel CLC Downer Length: a) Particle and fluid velocity b) Particle volume fraction.	98
Figure 7-11: Simulated Total Gas Species Mass Flow in a Complete CLC Process using a 5 m downer. Note: a) The negative sign indicates a mass flow rate defined in downward direction, b) The CLC reaction module was activated after 28 second, c) Simulation time steps are: 0.002s .	99
Figure 7-12: Simulated Total Gas Species Mass Flow Rates at Different Downer Height Levels of 5m and 20m. Notes: a) downer height is defined in the downward direction and from the top of the unit, b) the negative sign is assigned to mass flow shows in the downward direction.....	100
Figure 7-13: Total Simulated Gas Species Mass Flow Rates at Different Downer Height Levels using Particle Clusters only in the Downer. Note: The negative sign indicates mass flows in a downward direction.	101

CHAPTER 1 LITERATURE REVIEW

1.1 Introduction

Energy demands are expected to rise 60% by 2030, with 85% of that energy anticipated to come from fossil fuels [1]. Among the greenhouse gases (e.g. CO₂; NO_x; CH₄), CO₂ is the one that has the largest impact on global warming. Fossil-fueled power plants contribute to the significant CO₂ world emissions (~33-40%) [2]. Fortunately, technologies, such as CO₂ sequestration and Chemical Looping Combustion (CLC) have been developed to mitigate CO₂ emissions. However, for an effective CO₂ sequestration, highly concentrated CO₂ is required, which adds additional costs to CO₂ capture.

In this respect, Chemical Looping Combustion (CLC) is a promising technology which can maximize combustion efficiency, separate CO₂ inherently and reduce CO₂ capture costs significantly (100\$/ton CO₂) [3,4]. In addition to this, CLC can provide: a) a high thermal efficiency b) flameless combustion and c) the formation of small amounts of nitrogen oxide (NO_x).

However, suitable oxygen carriers are still an issue for large-scale CLC applications. Ni, Cu, Co, Fe and Mn are well known metal candidates that can perform as oxygen carriers for CLC. A detailed review on this issue can be found elsewhere [5,6]. Recently, a novel Ni-based oxygen carrier with a La-Co modified γ -Al₂O₃ support was reported by Quddus et al. [7] for methane combustion.

Several fossil fuels can be used for energy production such as natural gas, coal and biomass. However, as large amounts of fossil fuel derived CO₂ emissions continue to steadily increase, it is of primary importance to improve CO₂ capture processes. One valuable alternative is to use renewable feedstock such as biomass, in power stations. Biomass is the result of CO₂ capture in plants from the atmosphere via photosynthesis. Biomass can be converted into syngas, which can in turn, be used as a fuel in power stations. Syngas contains mostly CO and H₂ with some CH₄ and CO₂. On balance, complete combustion of syngas leads to net zero CO₂ fossil fuel based emissions.

Thus, it is the goal of this PhD research to investigate the performance of this Ni-based oxygen carrier (La-Co modified γ -Al₂O₃ support) for syngas combustion. Furthermore, it is also the aim of this research to consider for this OC in terms of its reactivity, its thermal stability and its carbon deposition.

To address these issues, the present chapter reviews the state-of-the-art considering: a) a CLC process development, b) the evaluation of suitable oxygen carriers, c) the bench-scale reactors to analyze oxygen carrier performance, d) the kinetic modeling, and e) the large scale CLC performance simulations.

1.2 Chemical Looping Combustion (CLC)

Lewis et al, first suggested the concept of CLC. Subsequently, the approach for the production of pure CO₂ from a hydrocarbon gas was proposed [8]. CLC enables one to increase the number of fossil fuel based power plants, obtaining higher thermal efficiency with minimum energy losses [9]. In addition, significant electrical efficiency (50-60%) can be achieved by using a CLC integrated power generation system where the CO₂ emission rate is rather low (0.33 kg/kWh). This appears to be the case while compared with a conventional fossil fuel power plant [10].

CLC typically employs a dual circulating fluidized bed system configured of two interconnected fluidized bed reactors known as *air reactor* and *fuel reactor* (refer to Figure 1-1). The solid oxygen carrier is circulated between the air and fuel reactors to be oxidized by air and reduced by fuel, respectively. Thus, the supported metal oxide oxygen carrier is circulated through a loop and carries oxygen for the purpose of efficient combustion. This yields a flue gas composed primarily of carbon dioxide and water vapor as well as other trace pollutants. Therefore, the CO₂ can easily be recovered by condensing water vapor. This eliminates the need of an additional energy intensive CO₂ separation process step. The free of water CO₂ can be sequestrated and used for other applications.

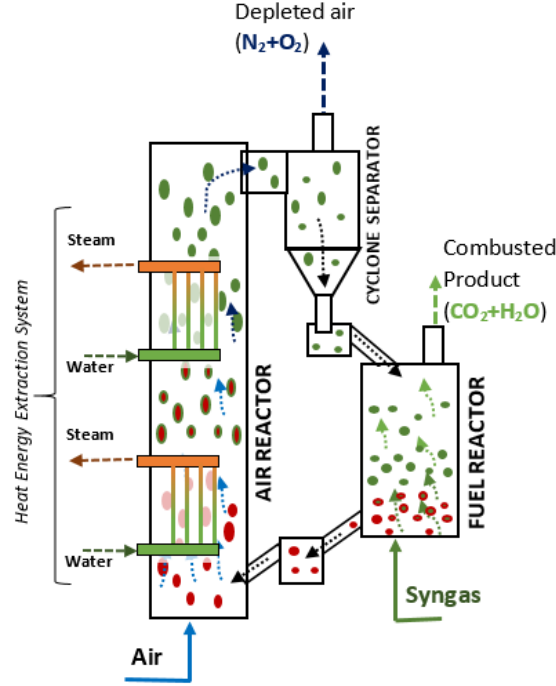
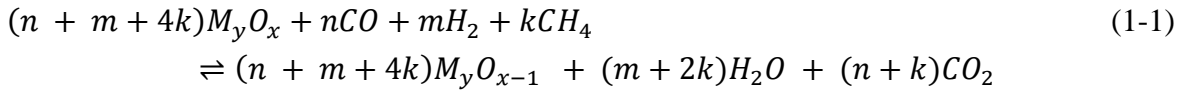


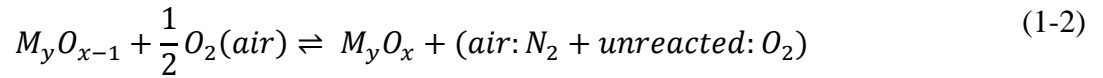
Figure 1-1: Schematic diagram of typical Chemical Looping Combustion process

A description of the overall reaction stoichiometry in the fuel reactor can be considered using Eq. (1-1):

Fuel Reactor: reduction



Air Reactor: oxidation



After the completion of fuel combustion, the reduced metal-oxide M_yO_{x-1} (or metal) is transported to the air reactor. Then, the M_yO_{x-1} is re-oxidized according to Eq. (1-2). This yields an outlet gas stream from the air reactor containing nitrogen and unreacted oxygen. These gases can be released to the atmosphere with minimum negative environment impact.

1.3 Thermodynamic Efficiency of CLC Process

As mentioned previously in this chapter, CLC consists of two interconnected reactors. A comprehensive thermodynamic analysis of the CLC process was reported in technical literature

[11]. This model represented the overall process as an internal combustion (IC) engine. The objective of this study was to determine the overall efficiency as shaft work generation.

Regarding oxygen carrier selection, there are two important thermodynamic criteria to be considered: a) equilibrium temperatures of the redox reactions involved have to be below the anticipated materials metallurgical limits b) the CLC must take place at temperatures high enough to obtain important CLC reaction rates.

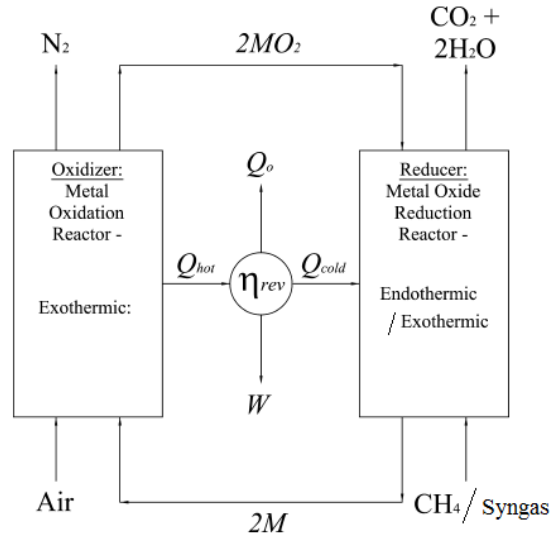


Figure 1-2: Schematic Diagram of an Ideal CLC System for Power Production [11]

Figure 1-2 reports a schematic representation of methane or syngas CLC using metal (species M) based oxygen carriers. As shown in Figure 1-2, methane CLC may typically lead to heat released (Q_{hot}) in the air reactor and heat consumed (Q_{cold}) in the fuel reactor (McGlashan 2008). However, in the case of syngas, CLC may involve slightly exothermic reactions in the fuel reactor (Ref). Thus, the syngas CLC process has to be evaluated with a Q_{cold} close to zero.

Furthermore, and as shown in Figure 1-2, shaft work (W) evaluations, involve the algebraic addition of air reactor enthalpy, fuel reactor enthalpy and heat losses (Q_o). As a result, thermodynamics provide shaft work availability. This can be established assuming that a) $\Delta S_o \approx 0$ and b) $\Delta S_o < 0$, where S is an absolute entropy.

In particular and for $Q_o \approx 0$ (adiabatic case for oxidizer and reducer reactors), one can define an overall efficiency for an IC engine as $\eta_{CLC} = W_{net}/(-\Delta H_o)_{fuel}$, with W_{net} being the work output from the heat engine. Thus, $W_{net,HC} = Q_{hot} \eta_{th,engine} = -(\Delta H_o)_{oxid} \eta_{th,engine}$.

Thus, $\eta_{CLC,HC} = \Psi \eta_{th,engine}$, where, $\Psi = (\Delta H_o)_{oxid}/(\Delta H_o)_{fuel}$. As a result, the process thermal efficiency has to be multiplied by an oxygen carrier and fuel system dependent factor.

Finally, by applying Hess' law, the Carnot efficiency of the heat engine in a CLC system can be written as:

$$\eta_{th,Carnot,CLC,rev,HC} = \frac{\psi - \Omega}{\psi(1 - \Omega)}, \text{ where } \Omega = \frac{(\Delta S_o)_{oxide}}{(\Delta S_o)_{fuel}}$$

Detailed discussions including the case of $\Delta S_o < 0$, are reviewed by McGlashan [11]. This manuscript reports the $\eta_{th,Carnot,CLC}(\%)$ as 82.05, for the system using NiO as oxygen carrier with coal as fuel. This appears to be indeed, an attractive industrial application for CLC.

1.4 Oxygen Carrier Requirements

The various requirements for a better oxygen carriers performance are listed below [5,6]:

- Adequate oxygen transport capacity,
- Favorable thermodynamics regarding the fuel conversion to CO_2 and H_2O at CLC temperatures,
- Good fluidizability of the oxygen carrier under expected operating conditions,
- High reactivity for reduction and oxidation reactions, in order to reduce the solid inventory in the fluidized bed reactors, keeping this reactivity during many successive redox cycles,
- Resistance to attrition with minimum losses of elutriated solids and negligible particle agglomeration,
- Negligible carbon deposition. This deposited carbon can be released as CO_2 in the air reactor, thus reducing overall CO_2 capture efficiency,
- Environment friendly characteristics and economic feasibility.

Unsurprisingly, pure metal oxides do not meet the above described characteristics, with oxidation and reduction reaction rates quickly decreasing in a few cycles [12]. This shows the need of a proper metal support, providing a high surface area and increased attrition resistance [13].

In all these respects, preparation methods have desirable effects on reaction performance and oxygen carrier stability. Several well-established methods can be found in the literature (Bartholomew et al. 2006) such as impregnation, adsorption/ion exchange, precipitation, sol-gel, spray drying and others. When considering the pros and cons of these techniques, the incipient wet impregnation method is considered as appropriate to achieve high metal dispersion over a desired support [14–16]. In addition, all the methods listed above, provide easy control of metal loading, being feasible for large-scale oxygen carrier production. However, one has to consider that special care has to be taken when implementing incipient wet impregnation, given that this leads to a non-uniform metal dispersion in the pore support.

Furthermore, numerous research studies have been performed when choosing metals such as Co, Cu, Mn and Fe as oxygen carriers, for industrial applications. As well, different metal supports (e.g. TiO_2 , SiO_2 , Al_2O_3) were tested to find stable and fluidizable oxygen carriers. Nevertheless, while oxygen carrier reactivity is a desirable property, it is not the only consideration criteria. Oxygen carriers may agglomerate or form undesirable species via metal-support interactions [17–19].

Given the above, and based on thermodynamics, reactivity and stability analysis, NiO was found to be attractive for CLC applications. However, unsupported NiO has shown poor performance in repeated redox cycles, as Ni crystallites agglomerate [20]. Thus, dispersed NiO over an Al_2O_3 support could be considered as an attractive alternative, given the alumina high thermal stability at high temperatures [21–23]. Furthermore, $\gamma\text{-Al}_2\text{O}_3$ support can be manufactured with good fluidization properties, which make it most suitable for fluidized bed CLC.

Nevertheless, undesirable metal support interactions may occur, leading to undesirable nickel aluminate formation. To address this issue, in literature using of NiAl_2O_4 as a support is found

[24]. This NiAl_2O_4 support increases nickel content requirements, making CLC less predictable. Thus, there are still significant challenges in the implementation of the NiAl_2O_4 oxygen carriers.

Regarding Ni-based oxygen carriers, it has been shown that these OCs can provide 1.84-6wt% oxygen transport capacity and 40-50wt% solid oxygen conversion at 750°C-1000°C under excess oxygen conditions [25,26]. Nevertheless, these OCs displayed low stability due to metal support interactions. In contrast, carefully designed Ni-based OCs, modified with La and Co, can display high thermal stability and less metal support interactions as shown by our research team at the CREC Laboratories, University of Western Ontario [14,27]. It was demonstrated that methane CLC with these OCs, yields 1.84-3.45% oxygen transport capacity and 40-72% solid conversion at 600-680°C. Nevertheless, the observed NiAl_2O_4 formed still presents a significant drawback for the oxygen carrier [14,15,27].

Given all of the above and the incentives for the syngas CLC, the aim of the present study is to develop a novel fluidizable HPOC having the following properties: a) High performance at 550-650°C within a 40s reaction time range, b) Enhanced oxygen transport capacity and OC oxygen conversion, c) Excellent CO_2 yields for efficient CO_2 sequestration, d) An OC free of NiAl_2O_4 formation.

1.5 Syngas CLC

Syngas is a mixture of CO and H_2 , can be produced from hydrocarbons and coal. As well, syngas can be manufactured via biomass gasification. Depending on the source, syngas may contain CH_4 , CO_2 and other undesired species as well. Syngas is as beneficial as natural gas in terms of an energy conversion application. However, to establish a syngas CLC system, highly performing oxygen carriers are a prime requirement. This PhD research considers CLC experiments using a syngas with a composition representative of those found in biomass gasification.

It is apparent that a nickel-based oxygen carrier is promising with respect to high reactivity, and stability. While several studies were already affected with methane CLC, there is very limited research carried out on syngas CLC and nickel-based oxygen carriers. Table 1-1 reports a summary of syngas CLC, with nickel-based supported oxygen carriers.

Table 1-1: Summary of Syngas CLC with a Nickel-Based Oxygen Carrier [6]

Metal Oxide Loading (%)	Support Material	Preparation Method	Reacting Agent	Reactor System	References
35	Al ₂ O ₃	COP	Coal, syngas + H ₂ S, CO, O ₂	TGA, CLC	[28–30]
2.5-20	α -Al ₂ O ₃	IMP	CH ₄ , H ₂ , O ₂	TPR, TPO, CREC-RS	[15,31,32]
18	α -Al ₂ O ₃	IMP	Syngas, CH ₄ , H ₂ , CO	TGA, bFB, CLC 300 W	[33–35]
5	Co-Al ₂ O ₃	IMP	CH ₄ , O ₂	CREC-RS	[27,36]
20	La-Al ₂ O ₃	IMP	CH ₄ , Biomass	CREC-RS	[37]
30	MgAl ₂ O ₄	SC+MM	CH ₄ , Syngas	TGA	[26]
20-40	NiAl ₂ O ₄	SC+MM	CH ₄ , H ₂ , Syngas	TGA	[26,38]
60	NiAl ₂ O ₄	DIS+SD	CH ₄ , H ₂ , Syngas	TGA, pFxB	[20,39,40]

CREC-RS: Chemical Reaction Engineering Centre Riser Simulator (a batch fluidized bed reactor), COP: co-precipitation, IMP: impregnation, FG: freeze granulation, SC: solution combustion, MM: mechanical mixing, DIS: dissolution, SD: spray drying, pFxB: pressurized fixed bed, TGA: thermogravimetric analyzer, TPR: temperature programmed reduction, TPO: temperature programmed oxidation

To understand syngas CLC, it is very important to perform reactivity studies in a batch fluidized bed reactor unit. This can help to develop valuable kinetic models for future applications as well as to develop designs of large-scale CLC reactors. Investigation on methane CLC using the CREC Riser Simulator, has already being developed by several researcher [7,36]. However, there is no prior article we are aware of, where syngas CLC was studied in the CREC Riser Simulator reactor.

1.6 Novel Tool for CLC Studies

The CREC Riser Simulator is a novel bench-scale reactor unit especially designed to determine catalyst performance under very short contact times (typically 2-40s). This novel device has been invented by de Lasa [41]. It was initially developed to determine the kinetic parameters of the catalytic cracking of hydrocarbons [42].

In the last 10 years, the CREC Riser Simulator has been applied to study a diversity of catalytic reactions including: a) chemical looping combustion, a) the steam and dry reforming of methane, c) the catalytic and thermal gasification of biomass, e) the oxy-dehydrogenation of light gases, f) the catalytic desulfurization of gasoline; among others [14,43,52–54,44–51].

In the CREC Riser Simulator as described in CHAPTER 3, a rotating impeller creates adequate up flow gas conditions. Due to this, particles contained in a centrally placed basket, are fluidized. The special engineering of this unit provides both fluidized particles and high gas mixing. Under a typical 4000-6000 rpm speed, the high gas recirculation yields a quasi-constant reactant concentration for all gas phase species.

Because of the intensive gas and particle fluidization in CREC Riser Simulator basket, the CREC Riser Simulator can be considered as a “fluidized batch reactor” described by the following equation:

$$V_T \frac{dC_i}{dt} = r_i W \quad (1-3)$$

Where, V_T represents the total reactor volume in cm^3 , C_i stands for the mass concentration of “ i ” species in g/cm^3 , t denotes the reaction time in seconds, r_i is the rate of either the formation or the consumption of “ i ” in grams of “ i ” species/(gcat s), and W stands for the mass of oxygen carrier in grams.

Thus, and in agreement with Eq.(1-3), the CREC Riser Simulator has to operate with approximately the same gas species compositions in all reactor locations, at every reaction time. In this respect, one can consider that reaction times in the CREC Riser Simulator are equivalent to the residence times in an industrial riser or an industrial downer unit. This similarity of reactions and residence time in the 2-40s range mimics the anticipated oxygen carrier conversion and syngas conversion rates. As a result, the CREC Riser Simulator provides an excellent basis for reaction kinetics and catalyst performance studies under the conditions of downers and risers.

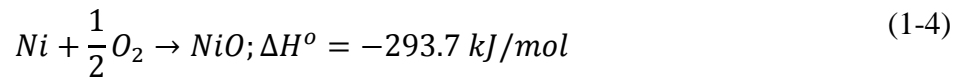
Gas mixing and particle fluidization in the CREC Riser Simulator were studied using hot wire anemometry, fiber optic techniques and a Plexiglas unit [55]. Fiber optics, hot wire anemometry and pressure drop measurements were implemented to establish both fluidization and gas recirculating flows [41]. Using this method axial downward gas velocities in the outer reactor section were measured. This allowed calculation of the recirculating gas flows and the mixing times. Good fluidization and mixing times were observed at a 6300 rpm impeller speed rotation. Mixing times with high gas recirculation were smaller than 0.1 seconds.

On the other hand, CFD offers unique opportunities for the understanding of flows in the CREC Riser Simulator (CHAPTER 4). This allows one to therefore, introduce a CREC Riser Simulator “without vertical baffles”. On this basis, a double vortex fluid structure can be computed as follows: a) an upflow vortex promoted by a rotating impeller, in the center section of the CREC Riser Simulator, b) a downflow vortex generated at the tip of the rotating impeller blades centrifugal forces. One should notice that the second downflow vortex becomes a rotating upflow at the bottom of the CREC Riser Simulator. Altogether, this leads, to strong gas mixing in the inner and outer reactor spaces as well as intense fluidization in the reactor basket. Thus, a fluid flow in the chamber of CREC Riser Simulator can be viewed as two vortices, a central spiraling upflow and a peripheral spiraling downflow. With this end in mind, a CFD model based on COMSOL Multiphysics® is considered in the present study. Using CFD, a double vortex structure with high mixing patterns is described as shown in CHAPTER 4.

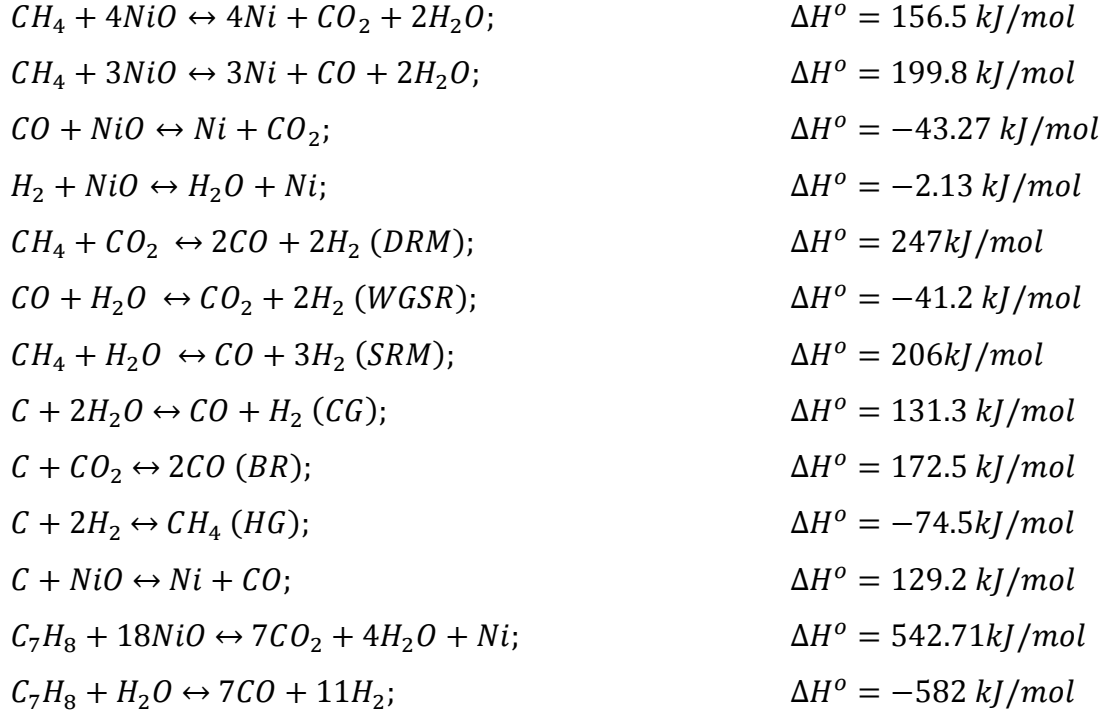
1.7 CLC Reaction Network

The CLC reaction mechanism is a fundamentally based description required for the development of a kinetic model.

In a CLC system, the oxidation reaction rate, under the anticipated operating conditions (550-650°C), is high enough not to show a dependency of the reduction cycle on the thermal level [56,57] . Thus (1-4), represents the best stoichiometry to describe the oxidation of the NiO oxygen carrier is as follows:



Furthermore, in the fuel reactor (FR), there are a number syngas (CO, H₂, CH₄, CO₂) reactions with NiO oxygen carrier, those take place. All of them contribute to the overall reduction CLC process as follows:



with BR: Boudouard Reaction; CG: Char Gasification; DRM: Dry Reforming; HG: Hydrogenating Gasification; SRM: Steam Reforming; WGSR: Water Gas Shift Reaction

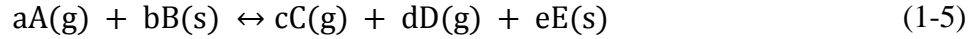
The above-described reactions, based on observable species, are the ones often used for kinetic modelling. This is the case even when acknowledging that actual reaction mechanisms may involve intermediates including radical species [7,58]. One should not however, that the selection of observable chemical species, as main contributors of the nickel based kinetic model, could be a function depend on the specific oxygen carrier employed.

1.8 Thermodynamic Limit of Syngas CLC and Ni-based OC

A thermodynamic analysis can be developed to calculate equilibrium products of syngas and NiO oxygen carrier reactions within a range of 25-700°C at 1 atm pressure. Equilibrium refers to the stable condition of chemical reactions after which no overall reaction takes place. This is achieved by minimizing the Gibbs Free Energy [59]. There are two approaches for analyzing the equilibrium

condition: a) the stoichiometric approach b) the non-stoichiometric approach. The first approach requires well-defined reactions with balanced stoichiometric equations.

One can write a generic chemical reaction as in Eq.(1-5):



Assuming that Eq.(1-5) applies at chemical equilibrium, an equilibrium constant can be calculated as follows:

$$K_c = \frac{[C]^c [D]^d [E]^e}{[A]^a [B]^b}$$

where, $[A]$, $[B]$, $[C]$, $[D]$ and $[E]$ represent activities of both gas and solid reactants and products. At high temperatures and close to atmospheric pressure conditions, the reactants and the products activities in the gas phase can be approximated to their partial pressures. In addition, the activity of solid compounds can be considered as a unity. Then, the equilibrium constant can be rewritten as follows:

$$K_p = \frac{[P_C]^c [P_D]^d}{[P_A]^a}$$

where, B and E are solids and $[P_B]^B=1$, $[P_E]^E=1$

A similar approach for the CLC thermodynamic analysis can be found in [60,61].

Furthermore, the equilibrium constant K_p can be determined from the Gibbs free energy of reaction (ΔG_r) using $K_p = \exp[-\Delta G_r/RT]$; with , $\Delta G_r = \sum(\Delta G_f)_{final} - \sum(\Delta G_f)_{initial}$ and $R=8.314 \text{ J/(mol.K)}$. One should note that the ΔG_f for pure substances can be obtained from the thermodynamic property available database [62].

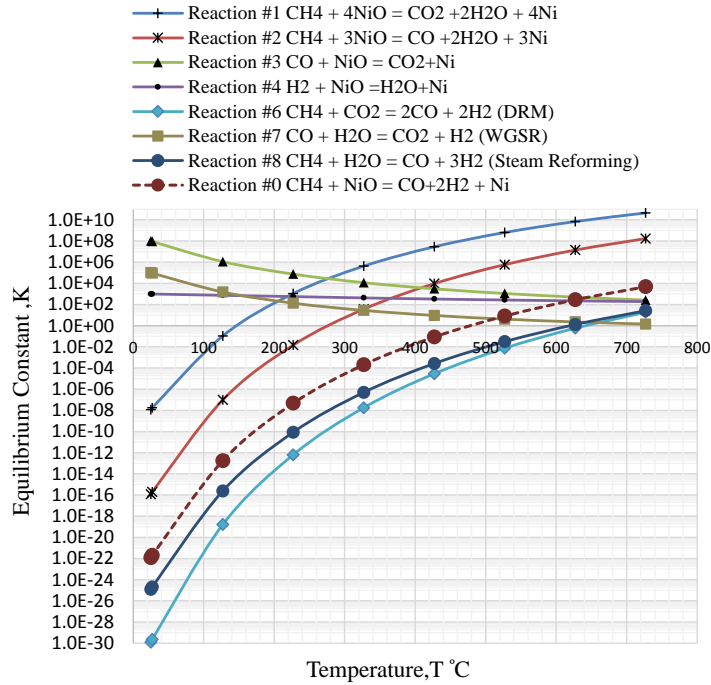


Figure 1-3: Equilibrium Constant as a Function of Temperature

Figure 1-3 reports the change in the equilibrium constant with temperature, for eight possible syngas CLC reactions. This analysis was developed with a 20% CO, 10% CH₄, 20% CO₂ and 50% H₂ syngas. It also considered the stoichiometric amounts of NiO oxygen carrier required for syngas combustion into CO₂ and H₂O.

Thus, one can see that while equilibrium constants for various CLC syngas reactions can be calculated as shown in Figure 1-3, using the formation Gibbs free energies and formation enthalpies, there is still a lack of numerical solutions for solving the independent set of resulting equations. A numerical solution for this set of independent equations using nickel oxide is reported later in CHAPTER 6 of the present PhD dissertation.

1.9 Kinetic Modeling of CLC System

A kinetic model provides important information regarding mass and heat transfer processes inside the oxygen carrier particles by time. This can be accomplished by analyzing reaction performance during the reduction and oxidation cycles of CLC. In this respect, the kinetic model has to be specific enough to include oxygen transport capacity and OC physicochemical properties. Thus,

to accomplish this, various kinetic parameters have to be assessed for the various reactions involved. Table 1-2 reports a brief review on kinetic data for Ni-based oxygen carriers on Al_2O_3 support. Kinetic parameters for other oxygen carriers can be found elsewhere [6].

Table 1-2: Reported Kinetic Parameters for Reduction and Oxidation using Ni-based Oxygen Carriers and a Gaseous Fuel

Oxygen Carrier (wt%)/Support	Experimental Condition	Kinetic model*	Activation Energy kJ/mol	References
NiO(60)/ Al_2O_3	TGA (600-950°C)	SCM	$E_{\text{CH}_4}=78$, $E_{\text{H}_2}=26$	[63,64]
NiO(20)/ Al_2O_3	TPR-TPO (200-750°C)	NNGM	$E_{\text{H}_2}=53$, $E_{\text{O}_2}=45$	[32]
NiO(20)-Co/ Al_2O_3	TPO-TPR(200-750°C) CREC Riser (650°C)	NNGM	$E_{\text{CH}_4}=49$, $E_{\text{H}_2}=45$, $E_{\text{O}_2}=44$	[65]
NiO(20)/Al_2O_3	CREC Riser (680°C)	SCM, NNGM, PLM	$E_{\text{CH}_4}=51$, 44, 39	[15]
NiO(20)/La- Al_2O_3	TPR-TPO (200-750°C) CREC Riser (650°C)	NNGM	$E_{\text{H}_2}=73$, $E_{\text{CH}_4}=70$,	[52]
NiO(40)/Ni Al_2O_4	TPR (300-600°C)	SCM	$E_{\text{H}_2}=96$,	[38]
NiO(65)/ Al_2O_3	TGA (800-950°C)	SCM	$E_{\text{CH}_4}=55$, $E_{\text{H}_2}=28$, $E_{\text{CO}}=28$	[66]
NiO(15)/ Al_2O_3	Fixed Bed (600-900°C)	MVM	$E_{\text{CH}_4}=77$, $E_{\text{H}_2}=26$, $E_{\text{CO}}=27$	[67]
NiO(40)/NiAl_2O_4	TGA (750-1000°C)	SCM	$E_{\text{CH}_4}=70$, $E_{\text{H}_2}=35$, $E_{\text{CO}}=34$	[68]
NiO(18)/Al_2O_3	TGA (700-950°C)	SCM	$E_{\text{H}_2}=20$, $E_{\text{CO}}=18$, $E_{\text{O}_2}=24$	[25]
NiO(21)/$\gamma\text{Al}_2\text{O}_3$	TGA (700-950°C)	SCM	$E_{\text{H}_2}=5$ (NiO), 235 (Ni Al_2O_4) $E_{\text{CO}}=5$ (NiO), 89 (Ni Al_2O_4) $E_{\text{CH}_4}=5$ (NiO), 375 (Ni Al_2O_4) $E_{\text{O}_2}=22$	[69]
*MVM: Modified Volumetric Model, NNGM: Nucleation and Nuclei Growth Model, PLM: Power Law Model, SCM: Shrinking Core Model				

As an OC support, gamma alumina has received much attention due to its high surface area (190 m^2/g) [52,70]. However, the potential formation of nickel aluminate may be an eventual issue,

reducing OC reactivity. In addition, high temperature ($>750^{\circ}\text{C}$) CLC operation may be required to reduce nickel aluminate [16,71].

Preventing the formation of NiAl_2O_4 by incorporating a cobalt additive in the OC, was reported by Quddus et al. [14]. It was found however, that controlling temperatures during OC preparation and CLC operation has a great effect on nickel aluminate formation and as a result, OC performance.

Considering these issues, this PhD thesis reports a development of a HPOC in CHAPTER 5, where the NiAl_2O_4 is excluded very effectively. The stable performance of this HPOC was demonstrated using a syngas with H_2/CO ratios of 2.5 and 1.33, at $550\text{-}650^{\circ}\text{C}$. This HPOC had at least, a 90% CO_2 yield.

An OC reaction rate model should also include a mechanistic solid state kinetic model accounting for: a) nucleation b) geometrical contraction, c) diffusion d) reaction order and e) power law [72,73]. In this respect, OC and CLC operating conditions must be selected to obtain an overall CLC reaction rate unaffected by either external or internal mass transfer.

Given the above, the Nucleation and Nuclei Growth Model (NNGM) [52,74,75] and the Shrinking Core Model (SCM) [64,66,69] have been considered to describe the solid state changes of the OCs. The SCM considers the CLC reaction initiation at the outer surface of the NiO crystallites, where NiO is converted into Ni^0 . This process continues inward until the crystallite metal core is reached.

As an alternative and according to the NNGM, the gas-solid reaction proceeds by nucleation, which means that once the reduction of a site is achieved, the reduction of neighboring unreacted NiO is initiated. Metal crystals dispersed in the porous support may have imperfections (e.g. cracks, surface, and point defects) [76]. It is at these metal sites, known as nucleation sites, that the activation energy displays a minimum value [77]. Therefore, the NNGM model has been found to be more suitable, especially with OCs where there is no influence of internal mass transfer on the overall CLC rate [73].

Regarding the CLC, it can be described as a function of the degree of OC reduction and as a function of the partial pressure of the gas phase chemical species [36,78] On this basis, several possible reactions including non-catalytic and catalytic reactions can be accounted for [6]. This

choice is critical to develop an adequate kinetic model and to determine intrinsic kinetic parameters.

Given the promising results obtained with the new HPOC, a comprehensive kinetic model, which describes the CLC using syngas, was investigated in the present study. The kinetic parameters were evaluated using experimental data obtained in the CREC Riser Simulator. It is anticipated that the proposed kinetic model may facilitate the evaluation of large-scale CLC reactor performance.

1.10 Large Scale and Demonstration Unit Simulation

Computational Particle Fluid Dynamics (CPFD) of the CLC process is considered helpful in the process of designing the air reactor and the fuel reactor at a large scale via the optimization of critical parameters. As well, by incorporating the reaction kinetic model, CPFD can be used to describe the performance of the CLC process with various configurations.

According to the technical literature, a typical air reactor can be designed as a riser while the fuel reactor using low superficial gas velocity can be designed as a bubbling fluidized bed. As well, in some cases, the air reactor can be designed as a small fluidized bed followed by a riser connected on its top. One can notice however, that there are no studies that report an air reactor as a riser and a fuel reactor as a downer. Table 1-3 displays a brief list of pilot scale CLC systems available at different locations. In addition, Table 1-4 presents some recent works on large scale demonstration unit simulation that developed the CLC process using various configurations.

Table 1-3: Summary of the Different Reactor Sizes and Configurations [79]

Designed Capacity (kW)	Fluidization Regime		Location
	Air Reactor	Fuel Reactor	
100	Bubbling bed with riser	CFB in bubbling regime	Chalmers University of Technology
100	Bubbling bed with riser	Bubbling bed	National Energy Technology Laboratory
100	CFB in fast regime	Moving bed	The Ohio State University
120	CFB in fast regime	CFB in fast fluidization regime	Vienna University of Technology

1000	CFB in fast regime	CFB in fast Fluidization regime	Technische Universität Darmstadt
CFB: circulating fluidized bed			

Table 1-4: A Summary of Recent Work on Large-Scale Simulations Using the CLC Process [6]

Oxygen Carrier	Fuel	Reactor Configuration	Reactor Capacity	References
58wt% NiO on bentonite	CH ₄	FR: bFB	Batch Mode	[80]
Fe-Ni on bentonite	CH ₄	FR: bFB; AR: Riser	12 kW _{th}	[81]
30.7wt.% FeO-ilmenite	CH ₄ , H ₂ , CO	FR: DFB; AR: DFB and Riser	1 kW _{th}	[82]
Glass beads (Geldart A and B)	Cold Run	AR: CFB; FR: CFB	42kW	[83]
			10kW	[79]

AR: air reactor; bFB: bubbling fluidized bed; DFB: dense fluidized bed; FR: fuel reactor;

As a result, it was felt that a complete system simulation based on Barracuda VR could be especially valuable. Barracuda VR allows Computational Particle Fluid Dynamics (CPFD) using an Eulerian–Lagrangian approach. CPFD considers a Lagrangian entity in order to define a computational particle. A computational particle involves uniform properties such as composition, size, density, and temperature. This software considers a MP-PIC (multi-phase particle-in-cell) method to model particle-fluid and particle-particle interactions. As well, Barracuda VR allows one to incorporate reaction kinetics and as a result, to simulate a large-scale CLC unit operating at relatively low computational time. A detailed description of the development of momentum equations and numerical approach are reported in the technical literature [84–86].

Regarding the required drag model for circulating fluidized bed simulation, Wen-Yu (spherical particle) [79] and Ganser Model (for non-spherical particle) correlations can be used in CPFD. Furthermore, the formation of particle clusters is also considered in this PhD research. This assessment is based on the particle cluster size distribution determined by Lanza et al. [87] for very similar particles.

Given all of the above, this study makes possible, as will be described in CHAPTER 7, a riser and downer configuration for CLC given: (a) the demonstrated high syngas conversion per pass in the downflow fuel reactor, (b) the manageable oxygen carrier particle circulation; (c) the anticipated low CO₂ gas leaking in the loop-seal between fuel reactor and air reactor.

1.11 Conclusions

The following can be considered to be the main conclusions of this literature review:

- a) Biomass-derived syngas can be used as a fuel in CLC, mitigating the negative CO₂ emissions impact. This approach could be employed very effectively in power stations.
- b) CLC thermodynamic models can be employed to set conversion boundaries for syngas CLC. This is considered of special significance, while using fluidizable oxygen carriers with important potential for industrial scale applications.
- c) Special experimental tools are needed to develop the kinetics that could be employed for CLC processes involving circulating fluidized beds. These experimental tools should be ranked and evaluated using CFD simulations to secure high gas mixing and good OC fluidization.
- d) Phenomenologically based kinetics models based on solid-state reactions, on metal supported oxygen carriers are needed. This is required for an adequate description of chemical changes in syngas CLC.
- e) CPFD simulations such as the one offered by Barracuda VR have to be considered to secure an adequate accounting of the kinetic models and the fluid dynamics while considering riser-downer integrated systems in large-scale CLC units.

CHAPTER 2 SCOPE OF RESEARCH

The opening remarks in CHAPTER 1, state that a highly performance oxygen carrier (HPOC) based on nickel over a fluidizable γ -Al₂O₃ support could become a promising alternative for CLC processes. This is the case, given the anticipated HPOC thermal stability and low metal-support interactions. On this basis, one can speculate that the proposed HPOC will allow large times-on-stream as well as a high syngas combustion performance, making CLC with the proposed HPOC an economically viable process alternative.

2.1 Specific Objectives

2.1.1 CFD Simulation of Novel CREC Riser Simulator: Mixing Patterns

As described in this PhD dissertation, the CREC Riser Simulator reactor will be used as a main experimental tool to evaluate the HPOC performance with syngas. Hence, one of the main objectives of this thesis is to describe unit flow patterns. This will allow assessing gas-solid mixing at high temperatures and pressures as well as evaluating the adequacy of the CREC Riser Simulator unit for HPOC performance evaluations.

2.1.2 Enhanced Oxygen Carriers: Preparation, Characterization

Another important objective of this PhD thesis is to establish the structural and reactivity properties of the HPOC (Ni-Co-La/ γ -Al₂O₃). In this context, one should consider the effect of the HPOC preparation methods on high HPOC reactivity, consistent with the high conversion of nickel aluminate into nickel oxide. With this end, it is planned to characterize the HPOC through the oxidation and reduction cycles, by using TPR and TPO. In addition, the NH₃-TPD, the BET-Adsorption Isotherm, the XRD and the pulse chemisorption analysis will be performed to further establish the HPOC physicochemical properties.

2.1.3 CLC performance using Syngas and Highly Performing Oxygen Carrier

Furthermore, given the importance of demonstrating the value of the HPOC for syngas CLC, a mini-fluidized CREC Riser Simulator will be used. Simulated biomass derived syngas, with different H₂/CO ratios is proposed to be employed during the runs. As well, a broad range of

temperatures and fuel/oxygen stoichiometric ratios will be considered. To complement reactivity studies, a thermodynamic analysis will be developed. Furthermore, this will be done to calculate equilibrium product composition following HPOC syngas combustion.

2.1.4 CLC using Syngas: Detailed Reaction Mechanism and Kinetic Modelling

Based on reactivity runs, a reaction mechanism for the Ni-Co-La/ γ -Al₂O₃ oxygen carrier will be established. This will allow establishing the most suitable conditions for better CLC processes. As well and on this basis, a phenomenologically based kinetic model will be developed using the statistical based evaluation of parameters with the calculation of the 95% confidence intervals and parameter cross-correlation. The proposed kinetic modeling approach could be of special value for the scale-up of CLC in large fluidized bed units.

2.1.5 CPFD Barracuda Simulation of Large Demonstration Scale Air-Fuel Reactors

Finally and using the established kinetics, a large demonstration scale CLC interconnected air-fuel reactor (riser-downer) process model will be established using CPFD Barracuda. Data obtained will allow: (a) The calculation of the riser air reactor and downer fuel reactor performances; (b) The calculation of the required HPOC circulation; (c) The evaluation of the extent of CO₂ gas leaking in the CLC unit at the loop-seal.

2.2 Accomplishments of Research Objectives

The present PhD dissertation includes the following completed research as reported in published and submitted manuscripts:

- a. *Manuscript 1*: **I. Ahmed**, S. Rostom, A. Lanza, H. de Lasa, “Computational Fluid Dynamics study of the CREC Riser Simulator: Mixing patterns, Powder Technology”, Volume 316, **2017**, Pages 641-649, ISSN 0032-5910, <https://doi.org/10.1016/j.powtec.2016.12.030>. IF=3.32

The manuscript mentioned above considers computational fluid dynamics in the mini-fluidized CREC Riser Simulator. These calculations were developed to secure adequate gas mixing while evaluating the HPOC performance. Detailed results are reported in CHAPTER 4 of this thesis.

- b. *Manuscript 2: I. Ahmed*, H. de Lasa, “Syngas Chemical Looping Combustion using a Highly Performing Fluidizable Oxygen Carrier”, *Catalyst Today*, **2019**.
<https://doi.org/10.1016/j.cattod.2019.01.011>, IF: 4.66

This article has recently been accepted with minor revision by the *Catalysis Today* Journal. This was an invited contribution for a Special Issue to Honor Prof. D. Bukur, University of Texas. This manuscript reports the development and characterization of the HPOC and its reactivity using syngas. Detailed results are reported in the CHAPTER 5 of this PhD Dissertation.

- c. *Manuscript 3: I. Ahmed*, H. de Lasa, “Kinetic Model for the Syngas Chemical Looping Combustion using a Nickel-Based Highly Performing Fluidizable Oxygen Carrier”, 2019, *Industrial & Engineering Chemistry Research*, (Accepted, **2019**), IF: 3.14

This invited article has recently been submitted to *Industrial & Engineering Chemistry Research* journal as one of the 110 papers for 110-year anniversary of I&ECR journal first issue. This manuscript describes and evaluate a phenomenologically based kinetic model with special value for the simulation of large-scale downer reactor units using CLC. A reaction mechanism is proposed and kinetic parameters are established using a statistically based analysis. Detailed results are reported in CHAPTER 6 of this PhD Dissertation.

- d. *Manuscript 4: I. Ahmed*, H. de Lasa, “Industrial Scale Riser/Downer Simulation of Syngas Chemical Looping Combustion of using Highly Performing Fluidizable Oxygen Carrier”.

This article is under preparation and will be submitted in early 2019, to Chemical Engineering and Technology (IF: 2.05). This manuscript considers a demonstration scale simulation of syngas chemical looping combustion using the HPOC. The CPFD Barracuda software is employed to account for both the fluid dynamics and the HPOC in a CLC downer unit. Various findings are reported in CHAPTER 7 of this PhD dissertation.

CHAPTER 3 EXPERIMENTAL METHODOLOGY

3.1 Introduction

This chapter describes the several experimental apparatuses and methodologies used in this PhD dissertation. This chapter reports the HPOC preparation method and its detailed physicochemical characterization. Additional details about the development of the fluidizable HPOC are provided CHAPTER 5.

All CLC experiments were performed with simulated biomass derived syngas in a mini-fluidized bed reactor CREC Riser Simulator. Details of the adopted operational procedures, as well as product analysis are also discussed in this section. Furthermore, supplementary information on operational protocols, calibrations and mass balance calculations are provided in Appendix-A.

3.2 Method of Oxygen Carrier Preparation

The Incipient Wetness Impregnation (IWI) method was found to be suitable for the preparation of the HPOC as already reported, in the technical literature [7,36,69]. The IWI provides a simple method, allowing close control of the metal loading in the fluidizable support, limiting coke formation, as will be discussed in CHAPTER 6.

There are four main steps involved in the HPOC preparation: a) support impregnation, b) HPOC precursor drying, c) reduction of the metal precursor loaded in the HPOC and d) HPOC calcination. To accomplish these steps, 20 g of $\gamma\text{-Al}_2\text{O}_3$ were typically added into a sealed conical flask with its lateral outlet exit connected to a 250 mmHg vacuum. Then, metal precursor solutions were prepared to reach the desired nominal metal percentile. For instance, a 0.5 ml/g of support solution was chosen to fill the $\gamma\text{-Al}_2\text{O}_3$ total pore volume. Using a syringe, the precursor solution was added drop-by-drop ensuring homogeneous support impregnation through the flux sealing. After these steps were completed, drying was performed using a 0.5°C/min heating until 140°C was reached, with drying continuing for at least 4h. Then, the HPOC precursor was reduced in a specially designed mini-fluidized bed. This mini-fluidized bed was installed inside a furnace (Thermolyne 48000) to be able maintain a desired temperature according to the preparation techniques. For HPOC reduction, a continuous 10% H_2 and 90% Ar gas flow was circulated throughout the HPOC bed with gas velocities being about 3 times the minimum fluidization velocity. Finally, the HPOC

was calcined in the same furnace under continuous airflow. Additional information regarding metal loading equipment, the mini-fluidized bed system, and the used furnace in the present study is provided in Appendix A.

3.3 Temperature-Programmed Reduction (TPR) and Oxidation (TPO)

TPR and TPO were performed by using a Micromeritics Autochem II 2920 Analyzer. During each experiment, 130-140 mg of an oxygen carrier sample was contacted with a 10% hydrogen (H₂) gas mixture balanced with argon (Ar) for TPR, and 5% oxygen (O₂) balanced with helium (He) for TPO. A flow rate of 50 cm³/min was employed for both TPR and TPO. The sample was heated using a 15°C/min ramp until it reached the desired temperature. The gas leaving the sample tube circulated to the TCD through a cold trap. This step ensured that this gas was comprised of water free H₂. The O₂ consumption was monitored using a thermal conductivity detector (TCD). The amount of H₂ or O₂ uptake by the HPOC sample was calculated via the numerical integration of the TPR and TPO profile areas, respectively. TPR analysis allowed one to know the available lattice oxygen for CLC. Consecutive TPR and TPO were effected to study the stability of the oxygen carrier while being subjected to several oxidation and reduction cycles.

3.4 H₂ Pulse Chemisorption

Pulse chemisorption was performed at a 50°C temperature following TPR runs using the Micromeritics Autochem II 2920 Unit. When utilizing this technique, a stream of argon gas was circulated through a bed containing approximately 130 to 140 mg of oxygen carrier at a 50 cm³/min rate. Then, a series of 1.0 cm³ STP pulses containing 10% hydrogen (H₂) balanced with argon (Ar) gas were injected. Each consecutive pulse injection was effected every 1.5 min. The effluent H₂ peaks were monitored using a TCD. When two consecutive H₂ peaks had essentially the same area, the HPOC sample was considered as hydrogen-saturated, indicating that no additional hydrogen could be chemisorbed.

The amount of chemically adsorbed hydrogen on the active sites of the oxygen carrier was used to calculate the percent metal dispersion as follows:

$$\%D = \frac{\text{Moles of metal on surface of sample}}{\text{Moles of total metal present in sample}} = \left(v \times \frac{V_{ads}}{V_g} \times \frac{MW}{W} \times 100 \right) \times 100$$

where, %*D* is the percent of metal dispersion, *v* is the stoichiometric factor (here, *v*=2, indicating that 1 mole of H₂ is chemisorbed with 2 moles of Ni atoms), *V_{ads}* is the chemisorbed volume of H₂ (cm³/g), *V_g* is the molar gas volume at STP (i.e. 22414 cm³/mole), *MW* is the molecular weight of metal (g/g-mole) and *W* is the % metal loading.

As well, the average crystal size (*d_v*) of the metal on the support was calculated from the percent metal dispersion by using the following equation:

$$d_v = \frac{\phi V_m}{S_m} \times \frac{1}{\%D}$$

where, ϕ is the particle shape constant, *V_m* represents the volume of metal atoms (nm³), and *S_m* is the average surface area (nm²) of metal particles exposed per surface metal atom.

On this basis, pulse chemisorption allowed the calculation of both metal dispersion and average metal crystal size in the HPOC [88].

3.5 Temperature-Programmed Desorption (TPD)

The ammonia (NH₃) TPD technique was used to establish the relative abundance of both Bronsted and Lewis acid sites. A Micromeritics Autochem II 2920 Unit was used for TPD experiments. Before the TPD experiments, the oxygen carrier sample was pre-treated by flowing helium (He) through it at 650°C for 20 min. and then cooled down to 100°C. Following this, a stream of gas containing 5% NH₃ balanced with He, was circulated through a bed containing approximately 170 to 190 mg of the OC sample, at a rate of 50 cm³/min and at 100°C for 1 h. After NH₃ adsorption, the HPOC sample was purged using helium again for 1 h, at the desired adsorption temperature. During the desorption, the temperature in the bed was programmed to rise at a linear rate of 20°C/min from ambient to 650°C, while a stream of He gas was circulated in the bed. Once the temperature in the bed exceeded the desorption energy, NH₃ was released from the HPOC sample surface. A TCD was used to quantify the ammonia in the OC. On this basis, the total acidity of the sample was determined by integrating the eluted ammonia peak representing the volumetric change of NH₃ in cm³ STP/min. with time in min.

3.6 Surface Area and Pore Size Distribution

The specific surface area and pore size distribution (PSD) of the prepared oxygen carrier were determined using Brunauer-Emmett-Teller (BET) and Barrett-Joyner-Halenda (BJH) Methods, respectively. Nitrogen adsorption-desorption was developed at 77.35 K in an ASAP 2010 Analyzer. Before each measurement, a 150–250 mg oxygen carrier sample was degassed at 200°C for 2 h and until the pressure was below 5 mmHg. Adsorption isotherms were measured within a relative pressure range of 0.001 to 1 at 77.35 K.

3.7 X-ray Diffraction (XRD)

X-ray powder diffraction patterns were obtained using a Rigaku Miniflex Diffractometer equipped with a monochromatic Cu K α radiation source (wavelength = 0.15406 nm, 40 kV, 40 mA). The samples were scanned every 0.02° from 10 to 80° with a scanning speed of 2°/min. Identification of the phase was made with the help of the Joint Committee on Powder Diffraction Standards (JCPDS) Files.

3.8 CREC Riser Simulator for Oxygen Carrier Evaluation

The CREC Riser Simulator is a reactor where the performance of a heterogeneous catalyst or oxygen carrier can be analyzed. The amount of catalyst or oxygen carrier used is in the order of 1 gram. Figure 3-1a provides a schematic diagram of CREC Riser Simulator Reactor (50.7 cm³ reactor volume) and its auxiliary components. As shown in Figure 3-1b, the CREC Riser Simulator includes two sections: an upper section and a lower section. These two sections can be easily disassembled allowing the loading and unloading of a HPOC in and from a central basket. Metallic gaskets seal both upper and lower sections of the CREC Riser Simulator.

Two 20-micron grids allow HPOC particles to be confined inside the central basket. The catalyst basket is placed in the lower reactor section. This creates an annulus section in between the catalyst basket and lower shell section. As well, there is an impeller located in the upper reactor section. The impeller rotation produces both a suction effect as well as a compression, causing the gas to move in the upward direction through the inside of the basket and in a downward direction through the outer annulus.

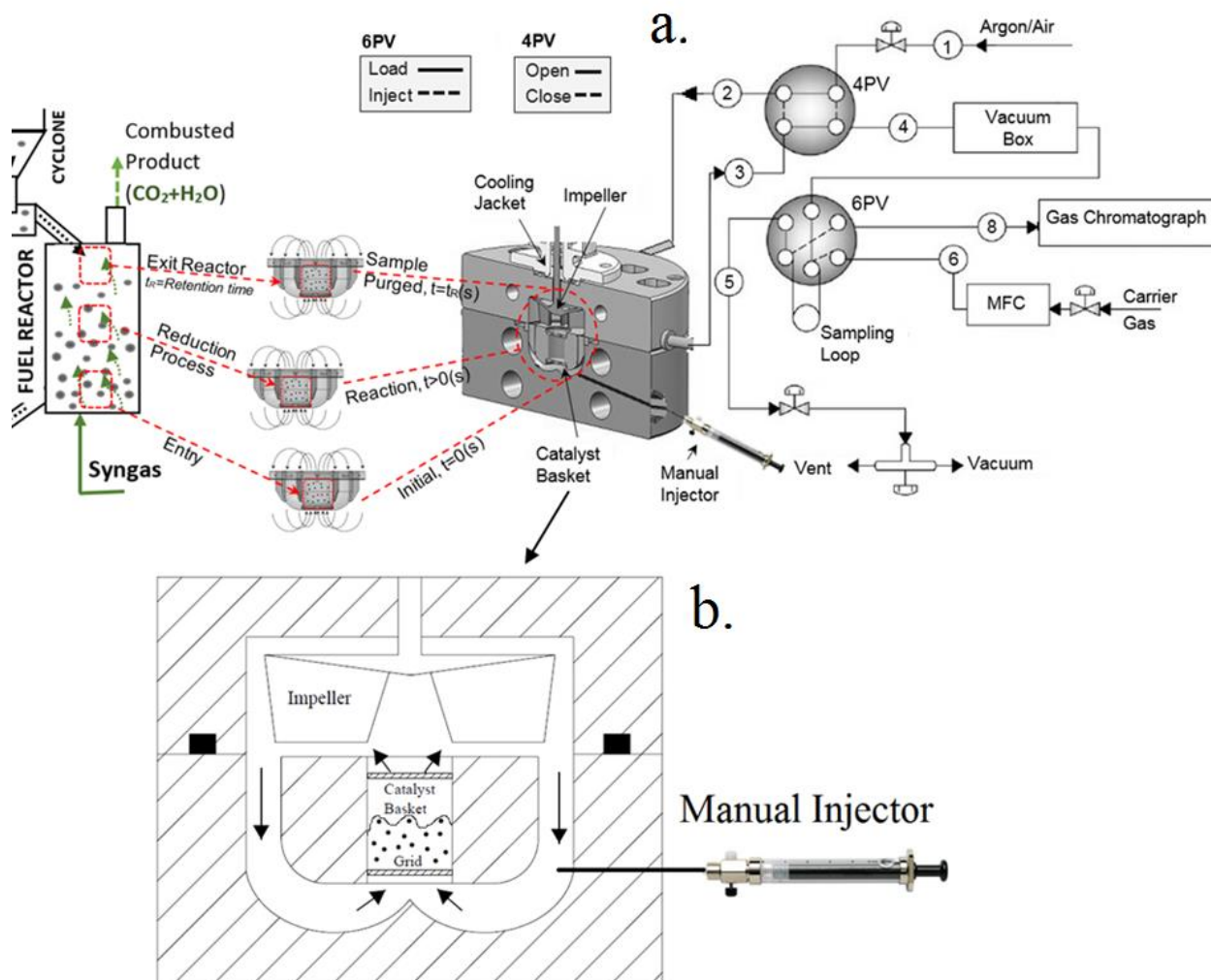


Figure 3-1: Schematic Diagram of CREC Riser Simulator: a) Reactor system showing CLC application and b) Catalyst/oxygen carrier basket (4PV: four-port valve, 6PV: six-port valve, MFC: mass flow controller)

Figure 3-1a also describes the various auxiliary components of the CREC Riser Simulator including the injection port for gases or liquids, the vacuum box, the 4PV and the 6PV. In the CREC Riser Simulator, the reaction time is controlled using an automatic four-port valve (4PV) that opens the reactor to the vacuum box. The vacuum box collects products and helps to transfer the CLC gas phase products into a gas sampling loop (1 cm^3) when the six-port valve (6PV) is in the “load” mode. After loading the gas product sample into the gas-sampling loop, the CLC products were directed to a gas chromatograph (GC) for further analysis, while having the 6PV in the “inject” mode. The CREC Riser Simulator and its auxiliary components altogether provide: a)

an almost instantaneous reactant injection, b) gas-solid reactions under controlled conditions, c) quick product evacuation, and d) “online” product analysis via gas chromatography.

3.8.1 Reactor Preparation for Reaction

For each CLC run, 175 mgs of the HPOC were loaded inside the reactor basket. Then, the lower section of the reactor was attached to the upper section using a metallic seal. This metallic seal ensured the absence of gas leaks during runs. Following this, argon was circulated through the reactor and vacuum box. This argon flow carried away any impurities of chemical species remaining in the CREC Riser Simulator reactor and reactor lines from previous experiments. Following this, the vacuum box was set to 150°C, in order to ensure that all reactant and product species were in the gas-phase.

Once the argon purge was completed, both the upper and lower reactor sections were progressively heated until the reaction temperature was reached. Then, and once the selected temperature was reached, the argon flow was stopped and the reactor was closed at close to atmospheric pressure by manually shutting the 4PV. Following this, the vacuum box was evacuated and set at 3.0 psi using a vacuum pump. Once all these preliminary steps were completed, the reactor was ready for the CLC experiments feeding syngas, with the GC being kept at standby conditions.

3.8.2 Performing Reaction

The injector port of the CREC Riser Simulator Reactor allowed injecting set amounts (5-10 ml) of syngas using a syringe. Following this, and once a pre-selected time was reached; a triggered timer opened the 4PV automatically, releasing all the gas phase products into a vacuum box. Both during the reaction period, as well as during evacuations, the total pressures in the reactor and vacuum box were recorded continuously. Then, a representative CLC product sample was collected inside the sample loop of the 6PV. Once this step was completed, the CLC product held in the sample loop of the 6PV was sent to a GC, equipped with a TCD and FID, for product identification and quantification.

3.8.3 Product Analysis System

3.8.3.1 Sample Analysis

Figure 3-2 reports the flow diagram for product analysis from the CLC experiments.

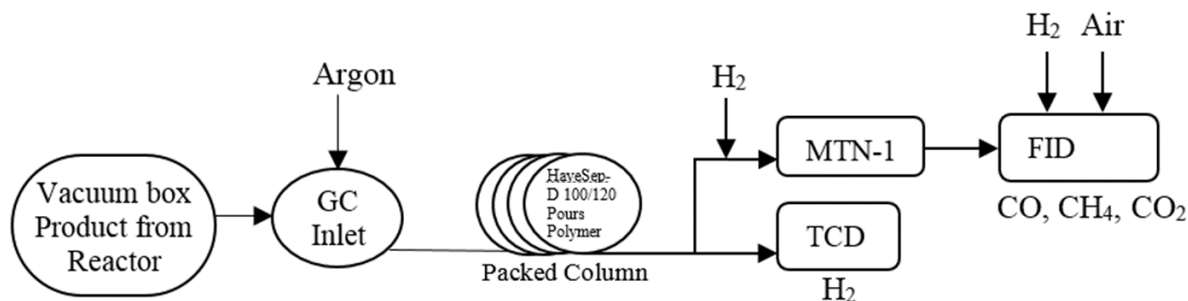


Figure 3-2: Schematic Flow Diagram of Product Analysis System

In the CLC runs, argon was used as a carrier gas, to accurately detect H₂ using a TCD (Thermal Conductivity Detector) and CO, CH₄, CO₂ utilizing a FID (Flame Ionization Detector), configured with a Methanizer (MTN). The MTN converts CO and CO₂ into CH₄. Hence, CO, CH₄ and CO₂ are all detected in FID as CH₄ peaks. Furthermore, different retention times and calibrations help to both identify and quantify individual gas species collected in the GC inlet sample loop in $\mu\text{mole units per cm}^3$ units.

Regarding the GC analysis, a temperature program was developed to obtain efficient species separation using a GC- packed column. Furthermore, to establish quantification and calibration profiles for individual species in the 1 cm^3 sample volume, a standard gas composition with 20vol% CO, 50vol% H₂, 10vol% CO₂ and 10vol% CH₄ was used. The detailed configuration of the GC system, the gas calibration methods and the individual profiles of calibration are all mentioned in Appendix A.

3.8.3.2 Post-Analysis Calculations

Based on the collected data, the HPOC performance was evaluated. The HPOC performance was established based on CO₂ yield, OC oxygen conversion and individual component conversion as per Eqs. (3-1), (3-2) and (3-3), respectively:

$$Yield\ of\ CO_2, Y_{CO_2} \% = \left(\frac{n_{CO_2}}{n_{CO} + n_{CH_4} + n_{CO_2}} \right)_{product} \times 100 \quad (3-1)$$

$$OC\ oxygen\ conversion, \alpha \% = \frac{(Oxygen)_{product}^{gas} - (Oxygen)_{feed}^{gas}}{(Oxygen)_{feed}^{solid}} \times 100 \quad (3-2)$$

$$Species\ Conversion, X_i \% = \left(1 - \frac{n_{i,product}}{n_{i,feed}} \right) \times 100 \quad (3-3)$$

where, n_i = moles of i in the gaseous product/feed, $i=CO, H_2, CH_4$

3.9 Conclusions

This chapter describes the methods of HPOC characterizations and experimental evaluation required for this PhD research. The following are the most important conclusions of this chapter:

- a) An incipient wetness impregnation (IWI) successfully implemented for the preparation of the Ni-based oxygen carrier. This method involved a small-scale fluidized bed where both reduction and calcination of OC precursor were developed. This method secured a targeted amount of metal loadings in the supported OC.
- b) The H_2 -TPR and O_2 -TPO were valuable to determine the amount of active lattice oxygen in OC and also to detect the possible presence of nickel aluminate. Furthermore, consecutive TPR and TPO helped showing the stability of OC under successive oxidation-reduction cycles. The X-ray diffraction (XRD) was also used to confirm the absence of nickel aluminate.
- c) The particle size distribution, BET specific surface area, N_2 -adsorption isotherm, pore size distribution, acidity-basicity (TPD), and metal dispersion by chemisorption were also determined to complete the physicochemical characterization of the HPOC as shown in CHAPTER 5.
- d) The CREC Riser Simulator reactor was used successfully employed to carry out syngas and HPOC reactivity. This allowed us quantification of CLC products at various reaction times, temperatures and fuel to OC stoichiometric ratios. These valuable experimental data led as shown in CHAPTER 6 to the development of a kinetic model for HPOC.

CHAPTER 4 CFD MODEL FOR CREC RISER SIMULATOR

4.1 Introduction

The CREC Riser Simulator Reactor is a novel mini-riser unit. This chapter describes a laminar-turbulent CFD (Computational Fluid Dynamics) simulation using the COMSOL Multiphysics® module to establish gas-solid mixing patterns. The proposed CFD calculations are verified using both experimental data (<10-15% difference) and mass balance errors (< 0.1%). Results show the significant detrimental effect of basket vertical baffles implemented in earlier designs of the CREC Riser Simulator Reactor. Based on this, it is demonstrated that a double vortex flow leading to high gas mixing is favored in a new reactor configuration “without” basket vertical baffles. For instance, at 4200 rpm, in a basket unit loaded with 0.8 gm of catalyst, close to 69 cm/s gas axial velocities were observed. This shows turbulent or fast fluidization conditions with smaller than 0.51s mixing times. In addition, this new suggested design with enhanced mixing, places the CREC Riser Simulator in a new class of laboratory scale fluidized catalytic units.

This CFD model also allows calculating axial and circumferential gas velocities, and pressure changes. Reported results demonstrate that a modified basket “without” vertical baffles provides enhanced gas-phase mixing and particle fluidization. These new findings are valuable to operate the CREC Riser Simulator for extended periods, with intense mixing both in the inner and outer unit reactor chambers, limiting fine particle carry over.

4.2 Modeling Strategy

4.2.1 Gas and Solid Phases Considered

Regarding the developed numerical simulation, air at 25° C and 1 atm were considered. FCC particles with a bulk density of 0.83-1.01 gm/cc and a particle size distribution in the 53-75 micron diameter range were selected for the calculations [89]. These particles belong to group-A particles in the Geldart’s powder classification [90].

4.2.2 Geometry Considerations

Regarding the developed numerical simulation, air at 25° C and 1 atm were considered. FCC particles with a bulk density of 0.83-1.01 gm/cc and a particle size distribution in the 53-75 micron

diameter range were selected for the calculations [89]. These particles belong to group-A particles in the Geldart's powder classification [90].

4.2.3 Geometry Considerations

A reactor and basket geometry was proposed as described in Figure 4-1. This figure describes the various inner reactor components such as the vertical baffles and basket grids. Model simplification assumes that impeller blades and basket vertical baffles are of negligible thickness (e.g. 1.6 mm) as suggested by [91,92]. These assumptions are adequate given the small changes in the flow pattern caused by these extra geometry specifications [93].

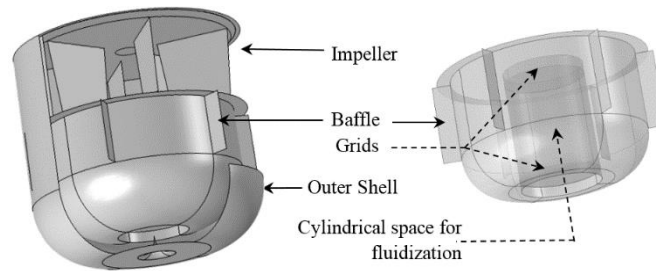


Figure 4-1: Geometry Considerations for the CREC Riser Simulator Modelling

Furthermore, in the CREC Riser Simulator, there is: a) A rotating component (turbine) where a suction effect is followed by a mild compression, b) A static component reactor body where the fluid moves downwards in the periphery and returns upwards in the basket. Thus, the rotating component (impeller) creates the driving force for gas recirculation.

4.2.4 Model Development

To proceed with the CFD simulation, one has to establish a model for the rotating parts, with a potential wide variation of RPM (e.g. from 525 to 6300 rpm). To accomplish this, the following has to be considered:

- Flows may encompass both laminar flow (e.g. at 500 rpm, $Re \sim 900$) and turbulent flow (e.g. at 5000 rpm $Re \sim 9000$). This is the case given the expected laminar and turbulent flows at various impeller speeds and different locations in the CREC Riser Simulator. In this respect, the Reynolds number (Re) can be calculated based on an impeller Reynolds number ($Re = D^2 N \rho / \mu$). As a result, this yields: a) a maximum value for N (rev/s), b) defined set values

for the impeller rotation, c) an impeller diameter D (m) d) a fluid density ρ (kg/m³) and (Pa.s) e) a fluid viscosity μ .

- Flow patterns can be described using mass continuity as per Eq.(4-1). As well, the Navier-Stokes Equation can be used for laminar and turbulent flows, utilizing Eq.(4-2) and Eq.(4-3), respectively. In the latter case, an average Reynolds approximation can be considered, using the turbulent kinetic energy (k) and the turbulent kinetic energy dissipation rates (ε) given by Eq.(4-4) and Eq.(4-5). With this aim, the RANS Standard K- ε model is used [94]. This option is considered adequate to simulate rotational flows in confined spaces with low pressure drops. This model was also proposed for gas-solid fluidization systems [92,95], with $C_\mu = 0.09, C_{e1} = 1.44, C_{e2} = 1.92, \sigma_k = 1.0, \sigma_\varepsilon = 1.3$. This approach showed good numerical calculation convergence within reasonable computational times [92].
- Flow can be assumed isothermal. This is satisfactory given the low mixing energy dissipated. It was experimentally observed that inert fluid mixing (e.g. air) in the CREC Riser Simulator (a batch unit) at 25° C and 1 atm, does not change the reactor temperature.
- Gas flow is simulated assuming that gravitational forces are the only external forces to be accounted for in the numerical solution.
- Wall roughness and its effect on gas flow is hypothesized to be negligible. This is adequate given the inner smooth reactor surface finishing achieved, during the CREC Riser Simulator manufacturing.

For the CREC Riser Simulator, a first available governing equation is given by mass continuity:

$$\frac{\partial \rho}{\partial t^*} + \rho \nabla \cdot \mathbf{u} = 0 \quad (4-1)$$

4.2.4.1 Laminar Flow Model-Navier Stokes Equation

At low impeller rotational speeds, the Navier-Stokes Equation for laminar flow can be reduced to the following:

$$\rho \frac{\partial \mathbf{u}}{\partial t^*} + \rho(\mathbf{u} \cdot \nabla) \mathbf{u} = \nabla \cdot \left[-p \mathbf{I} + \mu(\nabla \mathbf{u} + (\nabla \mathbf{u})^T) - \frac{2}{3} \mu(\nabla \cdot \mathbf{u}) \mathbf{I} \right] + \mathbf{F}; \quad (4-2)$$

Where, ρ is the fluid density, u is the fluid velocity, t^* is the frozen time, μ is the fluid viscosity, F is the volume or body force which acts through the volume of the body.

4.2.4.2 Turbulent Flow Model-Navier Stokes Equation

For the turbulent flow, the Reynolds Average Navier-Stokes equation (RANS) Standard k - ϵ model [96] can be considered as follows:

$$\rho \frac{\partial \mathbf{u}}{\partial t^*} + \rho(\mathbf{u} \cdot \nabla) \mathbf{u} = \nabla \cdot \left[-p\mathbf{I} + (\mu + \mu_T)(\nabla \mathbf{u} + (\nabla \mathbf{u})^T) - \frac{2}{3}(\mu + \mu_T)(\nabla \cdot \mathbf{u})\mathbf{I} - \frac{2}{3}\rho k\mathbf{I} \right] + F \quad (4-3)$$

While using this model, the following considerations apply:

- a) The kinetic energy of turbulence (k) and dissipation rate of turbulent kinetic energy (ϵ) equations are calculated as:

$$\rho \frac{\partial k}{\partial t^*} + \rho(\mathbf{u} \cdot \nabla) k = \nabla \cdot \left[\left(\mu + \frac{\mu_T}{\sigma_k} \right) \nabla k \right] + P_k - \rho \epsilon \quad (4-4)$$

$$\rho \frac{\partial \epsilon}{\partial t^*} + \rho(\mathbf{u} \cdot \nabla) \epsilon = \nabla \cdot \left[\left(\mu + \frac{\mu_T}{\sigma_e} \right) \nabla \epsilon \right] + C_{e1} \frac{\epsilon}{k} P_k - C_{e2} \rho \frac{\epsilon^2}{k} \quad (4-5)$$

- b) The production of turbulent kinetic energy due to the mean flow gradient, P_k is evaluated as:

$$P_k = \mu_T \left[\nabla \mathbf{u} : (\nabla \mathbf{u} + (\nabla \mathbf{u})^T) - \frac{2}{3}(\nabla \cdot \mathbf{u})^2 \right] - \frac{2}{3}\rho k \nabla \cdot \mathbf{u} \quad (4-6)$$

Where, μ_T is the turbulent viscosity which is evaluated as $\mu_T = \rho C_\mu k^2 / \epsilon$. σ_k , σ_e , C_{e1} , C_{e2} , C_μ are turbulence model coefficients.

4.2.4.3 Flow through the Basket Grids and Particle Bed

In order to complete the fluid dynamic description, one has to consider a mass continuity equation and a momentum balance equation applied to the two grids of the CREC Riser Simulator basket as follows:

$$[\rho \mathbf{u} \cdot \mathbf{n}]_{-}^{+} = 0 \quad (4-7)$$

$$\left[p - \mathbf{n}^T \left[\mu(\nabla \mathbf{u} + (\nabla \mathbf{u})^T) - \frac{2}{3}\mu(\nabla \cdot \mathbf{u})\mathbf{I} \right] \mathbf{n} + \rho(\mathbf{u} \cdot \mathbf{n})^2 \right]_{-}^{+} = -\frac{K_{grid}}{2} \rho_{-}(\mathbf{n} \cdot \mathbf{u}_{-})^2 - \Delta p_{bed} \quad (4-8)$$

$$\begin{aligned}
& \left[p - \mathbf{n}^T \left[(\mu + \mu_T)(\nabla \mathbf{u} + (\nabla \mathbf{u})^T) - \frac{2}{3}(\mu + \mu_T)(\nabla \cdot \mathbf{u})\mathbf{I} - \frac{2}{3}\rho k\mathbf{I} \right] \mathbf{n} + \rho(\mathbf{u} \cdot \mathbf{n})^2 \right]_+^+ \\
& = -\frac{K_{grid}}{2}\rho_-(\mathbf{n} \cdot \mathbf{u}_-)^2 - \Delta p_{bed}
\end{aligned} \tag{4-9}$$

Where, σ_s is the fraction of solid area of the basket grid. The grid type has 20 micron size parallel orifices that can be described using a $\sigma_s=0.76$ (opening area fraction 0.24). Pressure drop occurs both in the grids and particle bed. The flow resistance coefficient was determined as, $K_{grid}=0.98((1-\sigma_s)^{-2}-1)^{1.09}$ and Δp_{bed} was approximated with the Δp at minimum fluidization velocity. The signs “-” and “+” indicate the fluid flow conditions at the bottom and top surface of the grids.

One should notice that Eqs. (4-7), (4-8) and (4-9) are valuable to account for the pressure reduction in the various parallel orifices of the basket grids and throughout the particle bed.

4.3 Initial Values and Boundary Conditions

4.3.1 Initial Values for Computations

The fluid flow in the CREC Riser Simulator can be studied under steady state conditions. Given that this reactor operates as a batch unit, one can see that the impeller motion creates both a mild compression and mild suction. This promotes a downwards fluid flow circulation into the outer annulus region, and then an upwards fluid flow through in the center of the unit.

CFD simulations require adequate initial values in order to initiate calculations and to obtain a convergent numerical solution. These initially selected values were as follows: a) atmospheric pressure and ambient temperature, with gas density and viscosity defined at these conditions, b) gas velocity set at a zero value in the entire unit. The first of these initial conditions was considered adequate given the relatively small compressions/decompressions achieved in the unit while in steady operation (pressure change $\pm 0.1\%$). The second of these initial conditions applied to the gas velocity, which was set at zero allowing a progressive increase of both axial and circumferential gas velocities. This “unsteady” numerical solution mimics the physical conditions while turning the impeller on in the CRE Riser Simulator. This was accomplished in a “two stage” numerical solution process as will be described later in section 4.4.5

4.3.2 Boundary Conditions

4.3.2.1 Laminar Flow Model

There are a number of required boundary conditions for laminar flow used in the simulation. They are as follows:

- a) The slip velocity at the fluid-reactor interface and the fluid velocity at the outer reactor wall are zero ($\mathbf{u}=0$). This is acceptable given that the overall CREC Riser Simulator unit is not moving, remaining motionless during experiments [91].
- b) All gas velocity components display a zero value at baffle surfaces ($\mathbf{u}_{b,face}=0$ where $\mathbf{u}_{b,face}$ is the fluid velocity at either the “right face” or “left face” of the baffle). This is adequate given that the 6 vertical baffles in the catalyst basket remain motionless during experimental runs.
- c) The fluid component velocities at the face of the impeller blades are equal to the velocity of the impeller blade surface ($\mathbf{u}_{i,face} = \mathbf{u}_{imp}$, where $\mathbf{u}_{i,face}$ is the fluid velocity at either the “right face” or “left face” of the impeller blade, and \mathbf{u}_{imp} is the velocity of impeller blade wall). This is adequate given the small fluid inertial forces. Thus, the velocity of the impeller can be expressed as $\mathbf{u}_{imp} = (\partial \mathbf{x} / \partial t^*)|_x$ where \mathbf{x} is the displacement vector of the impeller.

4.3.2.2 Turbulent Flow Model

Regarding the boundary conditions of the turbulent flow model, there are velocity changes in the near-wall boundary layer region, with zero relative velocity at the wall. In the case of Low Reynolds Number (LRN), and when the turbulent flow integration method is used, a very fine mesh close to the wall is needed at the boundary layer. In the case of a high Reynolds Number (HRN), given that it becomes computationally intensive [97], a wall function is considered to bridge the near-wall region and the bulk stream.

This reduces computations and provide higher calculation accuracy. In this study, a standard wall function was used. It is applicable the RANS standard $k-\epsilon$ model [96]. This standard wall function has also been used also for several similar applications [98–101]. From a computational viewpoint, this method involves three steps.

A first step considers solving the momentum equation by determining the viscous force near the wall by using eq.(4-10) as follows:

$$\left[(\mu + \mu_T)(\nabla \mathbf{u} + (\nabla \mathbf{u})^T) - \frac{2}{3} \rho k \mathbf{I} \right] \mathbf{n} = - \frac{\rho u_\tau}{\delta_w^+} \mathbf{u}_{tang} \quad (4-10)$$

Where, $u_\tau = \sqrt{\tau_w / \rho}$ is shear velocity or friction velocity, τ_w is shear stress and δ_w^+ is wall lift-off also known as a dimensionless wall unit (y^+).

The second step considers the turbulent kinetic energy (k) change using $k \cdot \mathbf{n} = 0$ where \mathbf{n} is normal unit vector at the wall surface. Once this iterative calculation is completed, and k change is predicted, one can evaluate the energy dissipation rate as $\epsilon = \rho C_\mu k^2 / k_v \delta_w^+ \mu$ where, k_v is Von Karman's constant. A detailed description of this approach can be found in [96,97].

These boundary conditions are applied as a designated “wall function” to all reactor wall boundaries: reactor walls, vertical baffles surface and impeller blades. These boundary conditions have share a “zero-slip” and apply to all reactor walls including vertical baffles and impeller blades. They can be expressed as $\mathbf{u}_{rel} \cdot \mathbf{n} = 0$ and $\mathbf{u}_{rel,tang} = \mathbf{u}_{rel} - (\mathbf{u}_{rel} \cdot \mathbf{n}) \mathbf{n}$, where \mathbf{u}_{rel} is the relative fluid velocity with the wall and $\mathbf{u}_{rel,tang}$ is the relative tangential fluid velocity with the wall. For instance, there is zero slip velocity assigned to the face of vertical baffles, and this can be expressed as $\mathbf{u}_{b,face} \cdot \mathbf{n} = 0$ and $\mathbf{u}_{rel,tang,face} = \mathbf{u}_{rel,face} - (\mathbf{u}_{rel,face} \cdot \mathbf{n}) \mathbf{n}$. One should notice that the subscript “face” refers to either the “right face” of the baffle or the “left face” of the baffle. The same applies for the impeller moving blades.

Furthermore, the near wall regions can be divided into three sections: a) the viscous sublayer ($0 < \delta_w^+ < 5$), b) the buffer layer ($5 < \delta_w^+ < 30$), c) the inertial sub-layer-sublayer ($30 < \delta_w^+ < 500$) [102]. A dimensionless “wall-lift off” parameter can be determined as $\delta_w^+ = \delta_w u_\tau / \nu$ where, δ_w is the distance from the wall and ν is the kinematic viscosity. In this respect, the two laws of wall functions such as linear law and log-law are applicable when $\delta_w^+ = 11$ [97]. Hence, it is recommended to recheck the δ_w^+ magnitude at any stage of the calculations for model verification purposes [103].

4.4 Numerical Approach

4.4.1 Computational Tools

In this study to solve the flow numerically in the CREC Riser Simulator, a commercial software COMSOL Multiphysics® 5.1 CFD module was used. To accomplish this, the built-in tools were used for geometry and mesh design. In order to define fluid material properties (e.g. air), the built-in material library was employed with careful verification of selected equations. To obtain the numerical solutions, a personal computer was employed comprising: a) a processor “Intel® Core™i7-3930K CPU @ 3.20 GHz - 3.20 GHz”, b) physical memory “RAM 16.0 GB” as hardware. A “Windows 7, 64bit” operating system was employed in order to get an enhanced performance of simulation software.

4.4.2 Rotating Machinery Problem

Due to the presence of the rotary impeller in the CREC Riser Simulator, a special technique is required to simulate the impeller [104]. In this study the method of “frozen rotor” was considered. Its main advantage is that it does not require the use of a moving mesh. The “frozen rotor” method describes relative motion velocities. This method considers non-uniform circumferential distribution of pressure and velocity.

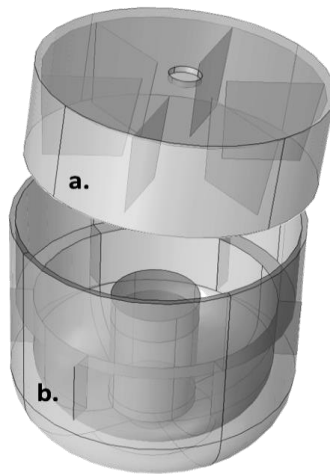


Figure 4-2: Computational Domains: a. Rotary fluid domain, b. Stationary fluid domain.

In the present study, the COMSOL “Rotating Machinery” module was used. This module comprises both the “Laminar Flow” and the “Turbulent flow RANS Standard k-e” model including

the “frozen rotor” approach. Thus, one requires two computational domains for each of these two models, with the rotary fluid domain representing the whole region covered by impeller. This is designated as section “a” in Figure 4-2. The “frozen rotor” technique was thus, applied in this rotary fluid domain. For the stationary fluid domain, designated as section “b” in Figure 4-2, a “stationary conventional model” was employed.

4.4.3 Symmetric Geometry

Before generating the mesh, it is advantageous to identify a unit “slice” which can represent the unit of symmetric portion. This helps to reduce the total computational mesh elements as well as the computational time. This approach is acceptable if one can consider a symmetrical flow domain, as in the case of the CREC Riser Simulator.

In this case as described in Figure 4-3, the reactor can be divided into six symmetric sections. This is possible because the reactor system comprises six blades of the impeller and six vertical baffles at the annular region. One portion out of these six sections as shown in Figure 4b can be considered as a control volume for computation.

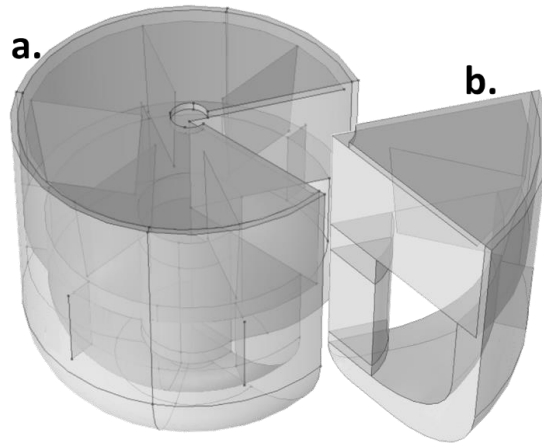


Figure 4-3: Symmetry Selection for Reactor “Slices”

As a result, boundary conditions with periodicity can be construed at the surface of each of the slices. One should mention that this, allows one to use a finer mesh to solve turbulent flows. This approach reduces computational time significantly, with no need of accounting for the full reactor geometry. For instance, in case of the configuration “with vertical baffles and with grids” the

model takes ~2 hr with ~0.6 million numerical elements for each simulation at a certain rpm. Thus, this consideration reduces the requirement of RAM (Random Access Memory or physical memory) significantly.

4.4.4 Mesh Selection

Figure 4-4 describes the “slice” domain and the associated mesh selected. In this respect, COMSOL has a built-in mesh generator adequate for 3D meshes. It is always recommended to use more than one level of meshing to check mesh dependency on the numerical calculation [95,99].

In the present study, two levels of meshes were used: a coarse mesh and fine mesh. Table 4-1 reports elements and an element volume ratio for the three meshes relevant to the present study: a) A basket with vertical baffles and with grids, b) A basket without vertical baffles and without grids c) A basket without baffle and with grids. Figure 4-4a provides an illustration of a typical mesh pattern of a symmetric slice. Figure 4-4b provides a close up of a boundary layer region mesh, critical for getting the desired δ_w^+ value.

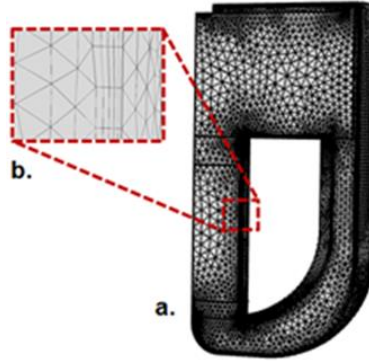


Figure 4-4: Typical Mesh Pattern Indicating Boundary Layer Mesh

Table 4-1: Mesh Parameters for Different Configurations

Basket Geometry Configurations	Element Volume ratio $\times 10^{-7}$		Total Elements	
	Coarse mesh	Fine mesh	Coarse mesh	Fine mesh
1. With <u>vertical baffles</u> and with <u>grids</u>	31.14	8.62	233061	575429
2. Without vertical baffles and without grids	34.53	2.71	192294	464130
3. Without vertical baffles and with <u>grids</u>	25.18	4.72	192005	471881

4.4.5 Numerical Solution Strategy

Initial guesses are very important for convergence. This is particularly true for impeller rotations higher than 1000 rpm. Lack of reasonable initial guesses may: a) generate a mathematically ill-conditioned matrix during the calculation process, b) create high velocities in the rotary reactor section and zero velocities in the stationary reactor section. One possible way to handle this problem is to solve the system for low rpm using the laminar flow model (e.g. <500). Then, one can use these calculated values as initial guesses for the model equation solutions at higher rpm.

Regarding the numerical solution implemented in this study, the steady state simulation FEM (finite element method) was used with the GMRES (Generalized minimal residual) method employed as solver. The FEM method has the ability to subdivide a given simulation into small parts that allows one to test the solution accuracy [105,106]. Regarding the GMRES method, it is an iterative process calculation originally reported by Saad and Schultz [107]. Using this approach, one can obtain good convergence with reasonable computation times.

4.5 Mesh Independence and Model Verification

Model verification was developed in the present study, via mass conservation using different computational mesh sizes. In addition, the wall lift-off (δ^+_w) parameter which is so critical for confirming model adequacy at the wall near region was checked.

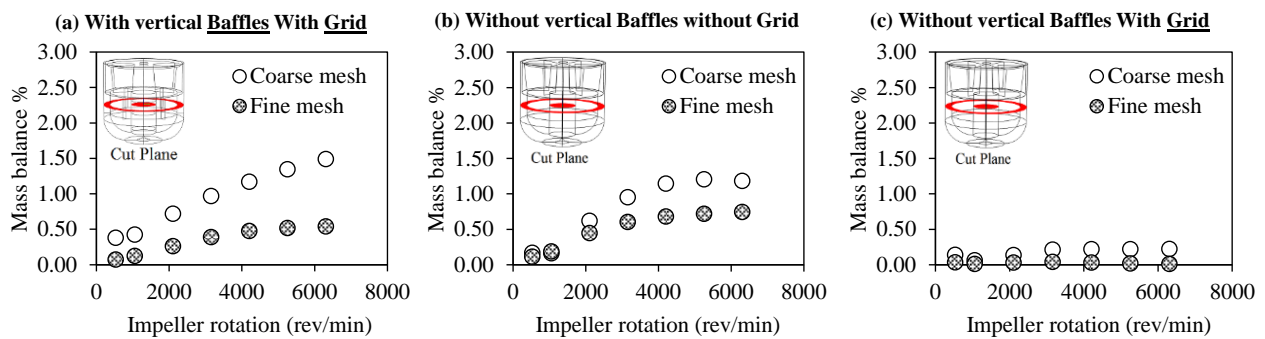


Figure 4-5: Mass Balance Established on the Basis of the % Difference of the Surface Integrated Mass Flow Rates for: a) Downward axial flow (annular outlet section) and b) Upward axial flow upflow inner reactor (basket).

Figure 4-5 reports the % Mass Balance established as the difference between the surface integrated mass flow rates at the annulus section (downward axial flow) and at the inner reactor basket section (axial flow upflow). To check this, two meshes were employed: a) a “fine” one and b) a “coarse” one. Figure 4-5a describes the % Mass Balances for the configuration “with vertical baffles and with grids”. This configuration is close to the one of the originally developed CREC Riser Simulator unit [41].

In this case, the maximum mass balance error is, in all cases, acceptable. This error is reduced from 1.5 to 0.4 %, moving from the fine to coarse mesh. Figure 4-5b refers to the configuration “without vertical baffles and without grids” configuration. The “without baffles and without grid” configuration is a hypothetical one, considered here as a reference. It is noticed that the Mass Balances % differences are more apparent for the “coarse” mesh. These results also show the numerical challenges of introducing both the vertical basket vertical baffles and the basket grids in the numerical calculation. Finally, Figure 4-5c reports the “without baffle with grid” configuration. This shows % Mass Balance errors of 0.25 % for the “coarse” mesh and 0.1% for the “fine” mesh. This further confirms the higher accuracy of calculations, once the preferred CREC Riser Simulator “without vertical baffles” is considered.

Concerning the wall lift-off parameter δ_w^+ , it was found to be ~ 11.06 in all cases simulated, including when using the fine and coarse mesh.

Figure 4-6 provides additional model verification comparing calculated axial velocities with data from [55]. This is the case for the “with vertical baffles with grids” configuration considering particles. One can see that as impeller rotation increases, the model shows close agreement with experiment data. For instance, at an impeller speed of 4200 rpm, the experimental gas velocity was ~ 90.6 cm/s and the model predicting velocity was ~ 102.5 cm/s which yielded a 12% difference only. Given that 4200 rpm is a typical condition used in the CREC Riser Simulator [41], one can see the adequacy of the proposed numerical model to simulate axial fluid velocities in this unit.

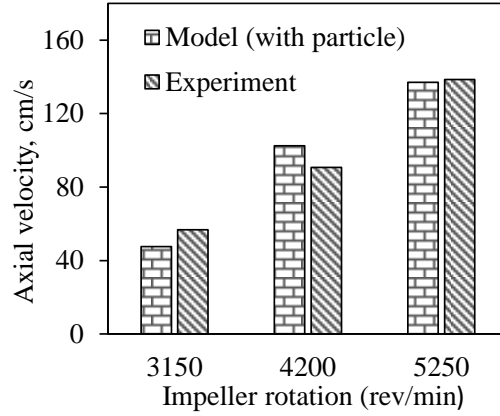


Figure 4-6: Comparison of Experimental Axial Velocity (Original Configuration) and Model Axial Velocity inside the Catalyst Basket

4.6 Results and Discussion

4.6.1 Mixing Patterns

Figure 4-7 reports streamline plots for both the “Original” and the “Proposed” configurations of CREC Riser Simulator, respectively at 4200 rpm for air at 25° C and 1 atm.

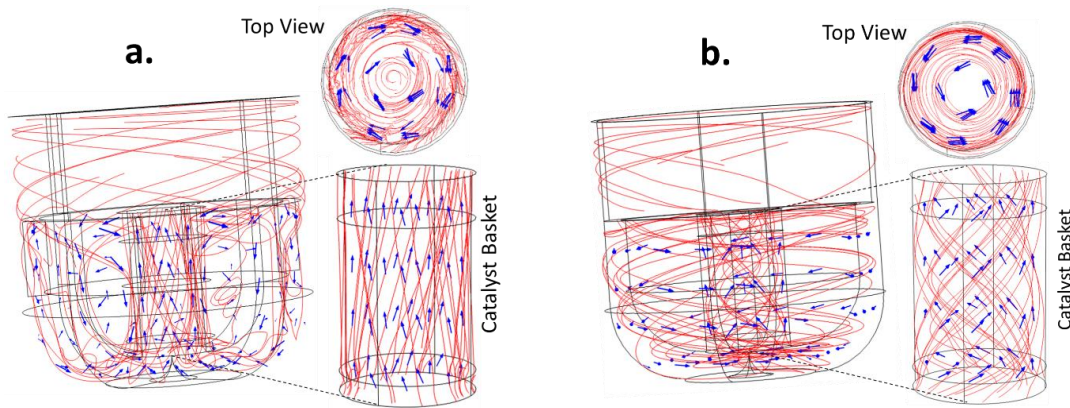


Figure 4-7: CREC Riser Simulator Mixing Patterns at 4200 rpm for Air at 25° C and 1 atm a) Original Configuration (with vertical baffles with grids) b) Proposed Configuration (Without vertical baffles with grids)

One can see in both Figure 4-7a and Figure 4-7b, that the motion of the fluid inside and outside the basket develop consistently forming inner- downwards and outer-upward vortices. Vortices

display spiral like patterns. We can also notice that in the case of the proposed new configuration without vertical baffles (Figure 4-7b), this leads to tighter spirals both inside and outside the basket. Thus, one can argue that the vertical baffles of the original configuration limits circumferential motion and as a result, mixing in the two section of the CREC Riser Simulator. These well mixed patterns are necessary conditions for the full applicability of eq.(1-3).

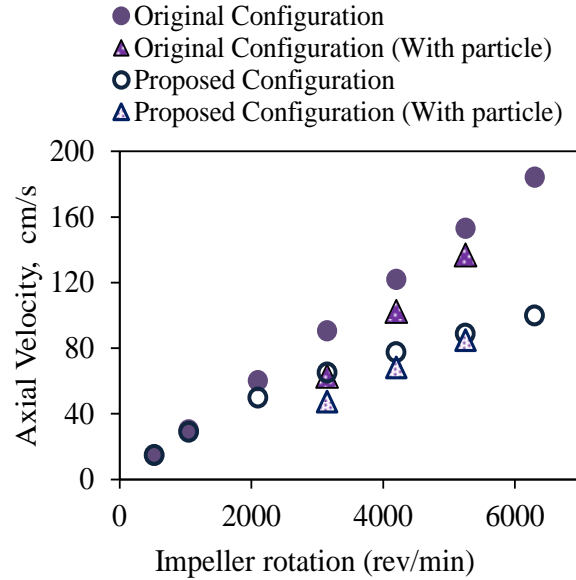


Figure 4-8: Simulated Average Axial Velocity inside the Catalyst Basket

Figure 4-8 describes the average axial velocity inside the catalyst basket. One can see that axial gas velocities increase almost linearly with the impeller rotation in the original configuration. On the other hand, it is shown this same axial velocity augments more progressively in the proposed configuration, with impeller rotation. This allows one to show the following features for the proposed new configuration of the CREC Riser Simulator: a) excellent fluid mixing both inside and an outside the catalyst basket, b) limited axial gas velocity reducing the probability of small catalyst particles entrained plugging the upper grid.

On the basis of the above, and given axial velocities, volumetric flows can be calculated at various rpm. For instance, this study reports an axial velocity of 100 cm/s at 4200 rpm in original configuration with 0.8 gm loaded particles. This yields a 140 cm³/s of volumetric flow and a 0.36s mixing time. Similarly, mixing time of 0.51s can be achieved in the “Proposed” new configuration.

This modest increase in mixing time is considered acceptable, given the enhanced overall mixing pattern in the proposed new configuration of the CREC Riser Simulator.

4.6.2 Velocity and Pressure Profiles

Figure 4-9 reports the axial gas velocity along the basket diameter at different RPMs for both the original and proposed CREC Riser Simulator configuration. For instance, in Figure 10b, one can observe at 3150 RPM, an axial gas velocity in the 80-95 cm/s range.

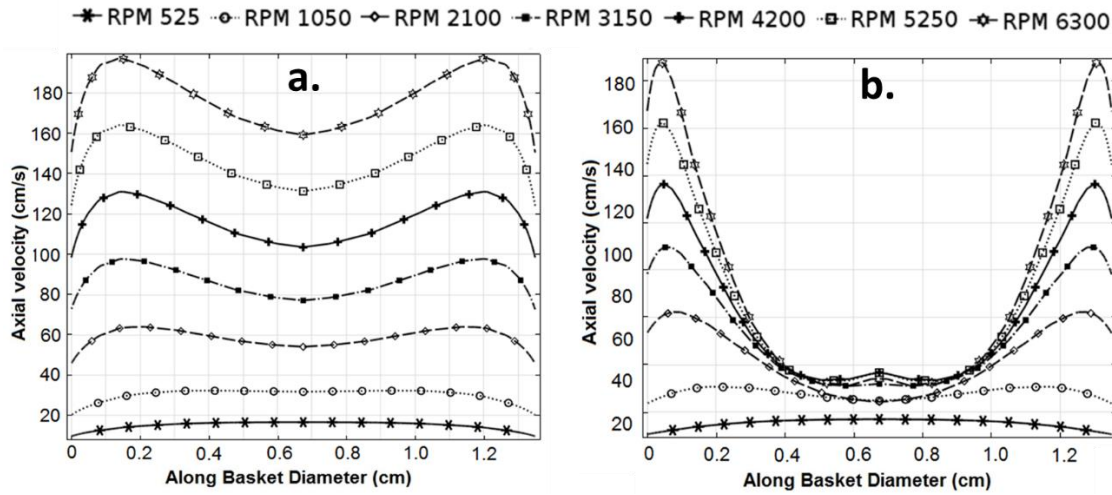


Figure 4-9: Velocity Profile inside the Catalyst Basket for Air at 25°C and 1 atm a) “Original Configuration b) New “Proposed Configuration”

In contrast, if the same axial gas velocity is analyzed in the new proposed configuration at 3150 rpm, it changes in the 40-100 cm/s range which is much greater. Hence, it is anticipated that fluidized particles in the new proposed configuration, will move in a field of changing velocities with: a) upper motion close to the walls and b) downward motion towards the center. Thus, this shows that the proposed CREC Riser Simulator configuration not only enhances gas mixing but as well helps particle mixing considerably. Meeting these two conditions is valuable in the case of studying catalytic reactions where coke formation and adsorption phenomena can contribute. All this, also helps, towards the full applicability of eq.(1-3) so essential for accurate kinetic modeling,

Figure 4-10a and Figure 4-10b describe the pressure field and gas velocities at 4200 RPM, in the new “Proposed” CREC Riser Simulator Reactor “without vertical baffles”.

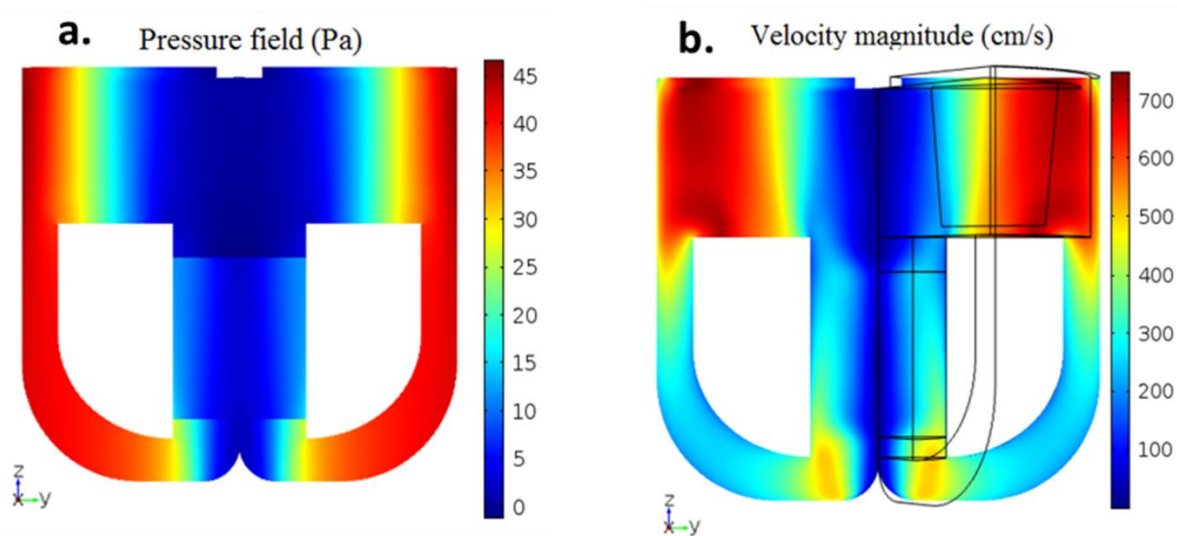


Figure 4-10: Pressure Field and Velocity Magnitude of the new “Proposed” Configuration (“without vertical baffles with grids”) at 4200 RPM with air at 25° C and 1 atm.

Figure 4-10a shows the expected pressure field with a maximum pressure at the impeller blade outer tip and a minimum pressure at “eye” of the impeller (center of the impeller). Furthermore, an additional pressure change across the unit is needed, given extra pressure drop in the two 20-micron grids. In Figure 4-10b, the axial velocity inside the catalyst basket is shown to be lowest at the center and highest at the periphery. This is because of the spiral like flow in the ne “Proposed” CREC Riser Simulator which is responsible for better solid circulation under fluidized conditions.

4.6.3 Impeller Rotation with Loaded Particles

The effect of particle loading is considered for both the original and the new proposed configurations of the CREC Riser Simulator. Figure 4-11 reported the pressure drop change at various RPMs as per the cases simulated in section 4.6.2. Given that the CREC Riser Simulator is a batch reactor, at a certain impeller speed, the total pressure drop along the gas flow has to be the same as the one generated by impeller. One can see that if the flow resistance due to friction in grids and particles increases, the gas velocity is reduced accordingly, to keep the set pressure drop delivered by the impeller.

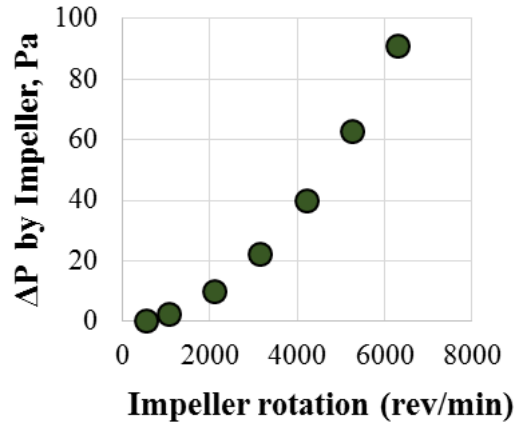


Figure 4-11: Changes of Pressure Drop with RPM in the New “Proposed” CREC Riser Simulator Unit.

As already reported in Figure 4-8, the average axial velocity and its changes with impeller rotation and this for the two proposed CREC Riser Simulator configurations. Simulations include and exclude the particle bed, showing that the particle bed has a mild influence on axial gas velocities. On the other hand, and as already stated in Figure 4-8, the reactor configuration with and without external baffles is an important design factor affecting axial gas velocities. Elimination of baffles leads to a desirable stabilization effect with the impeller speed minimizing excessive particle carry over towards the upper grid.

4.6.4 High Temperature Effect on Mixing Pattern

Figure 4-12 describes the mixing patterns in the proposed CREC Riser Simulator configuration at: a) 25° C and 1atm, b) 500° C and 1 atm, c) 500° C and 2 atm.

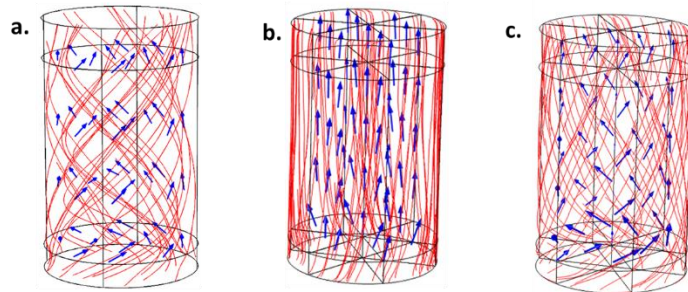


Figure 4-12: Mixing Patterns at 4200 rpm for Different Temperatures in the new "Proposed Configuration. a) 25° C, 1 atm b) 500° C, 1 atm c) 500° C, 2 atm.

Comparing Figure 4-12a and Figure 4-12b, one can see that increasing temperature changes significantly the mixing patterns with: a) higher axial fluid velocities and b) reduced fluid circumferential velocities. However, the characteristic fluid pattern observed at 25°C and 1 atm (Figure 4-12a), is recovered at 500°C and 2 atm, as shown in Figure 4-12c.

Thus, one can argue that a total pressure change or a total gas density change have a major effect on fluid patterns. It is known from experimentation with the CREC Riser Simulator that following feed injection, a typical reactor pressure at 500-600°C range is 2 atm [32,51,108]. Thus, the simulation performed, as described in Figure 13c, can be considered as a characteristic one in the new “Proposed” configuration of the CREC Riser Simulator providing good balance of gas axial velocities and gas circumferential velocities.

4.7 Conclusions

- a) It is shown that computational fluid dynamics using COMSOL Multiphysics® module allow a description of mixing flow patterns in the CREC Riser Simulator.
- b) It is proven, the proposed CFD model is adequate for the CREC Riser Simulator. This is accomplished changing mesh size and using experimental data from a previous study [55].
- c) It is shown that the calculated streamlines and velocity distributions profiles obtained with CFD, allowed calculating both axial and circumferential gas flow patterns.
- d) It is demonstrated that a new configuration of the CREC Riser Simulator with a catalyst basket “without vertical baffles” provides a good balance of axial fluid motion and circumferential fluid circulation.
- e) It is shown that the CREC Riser Simulator with a catalyst basket “without vertical baffles” requires at 25°C and 1atm, a 4200-5250 rpm impeller speed. This is needed for both suitable particle fluidization and good fluid mixing (high circumferential and axial fluid recirculation flows). It is anticipated that this also leads to a safe of eq(1-3) application for kinetic modeling.
- f) It is proven via CFD that temperature has a significant effect on gas mixing patterns in the CREC Riser Simulator. To compensate for higher temperatures (e.g. 500°C), higher total pressures are recommended (e.g. 2atm). These higher pressures allow one to recover the

desirable mixing patterns in the CREC Riser Simulator with a good balance of axial and circumferential recirculation flows.

- g) It is demonstrated that the successful application of the CREC Riser Simulator Reactor requires a CFD model. This would be valuable for assisting researchers to secure kinetic modeling suitable for continuous riser and downer units simulations. This should also be significant to secure in all experiments using the CREC Riser Simulator good mixing and particle fluidization. These are needed conditions for adequate gas-solid kinetics within 2-40 seconds reaction times.

CHAPTER 5 OXYGEN CARRIER DEVELOPMENT AND SYNGAS CLC

Biomass steam gasification yields a blend of H_2 , CO , CH_4 and CO_2 , designated as syngas. Syngas can be further combusted using fluidizable oxygen carriers (OC). This operation which is known as Chemical Looping Combustion (CLC), is valuable for syngas combustion. Because, it involves nickel oxidation and nickel reduction, which are both exothermic reactions provided that syngas contains mostly H_2 and CO . To improve syngas CLC and establish its application, a new Ni-based oxygen carrier was studied using a Co and La modified $\gamma-Al_2O_3$ support. This type of OC considerably limits the $NiAl_2O_4$ formation. This Highly Performing Oxygen Carrier (HPOC) was engineered using a special preparation methodology to exclude $NiAl_2O_4$ species formation.

Regarding reactivity tests, the syngas used in this study, emulates the syngas that can be derived from biomass gasification containing H_2 , CO , CH_4 and CO_2 . To establish the kinetic model, isothermal runs were developed in the CREC Riser Simulator which is a mini-batch fluidized bed reactor. The operating conditions were varied between 2-40s reaction times and 550-650°C, with the H_2/CO ratio being 2.5 and 1.33 with a ψ fuel to HPOC stoichiometric parameter ratio being 0.5 and 1. For the 2.5 and 1.33 H_2/CO ratios, a 92% CO_2 yield with 90% CO , 95% H_2 and 91% CH_4 conversions were achieved. As well, the HPOC showed an oxygen transport capacity ranging between 1.84-3.0 wt% (gO_2/gOC) with a 40-70% solid conversion

5.1 Oxygen Carrier for Syngas

Based on the review and recent works the novel mixed metal oxygen carrier Ni-Co-La/ $\gamma-Al_2O_3$ has better reactivity, enhanced thermal stability, and low metal support interaction with minimum crystallite agglomeration. This novel mixed metal oxygen carrier showed very well performance for methane chemical looping combustion [5,14,52,69]

It is anticipated that this oxygen carrier will have good performance for syngas. However, potential improvements of it are contemplated as part of this research for optimum performance using syngas. This novel oxygen carrier will be investigated for syngas combustion in the CREC Riser simulator. This will be most valuable for the design and implementation of new fluidizable CLC units.

An OC (20Ni1Co5La/ γ -Al₂O₃) was developed which consisted of 20wt% Ni over γ -alumina. It also included 1wt% Co and 5wt% La additives. Co and La additives have valuable effects on both NiAl₂O₄ and carbon formation reduction, respectively. This OC shares some common properties with the OC originally developed by Quddus et al. [14] and can further be referred in the present study, as OC-Ref.

5.1.1 Preparation of the OC of Reference (OC-Ref)

The OC designated as OC-Ref was prepared using an incipient wetness impregnation method as proposed by Quddus et al. [14]. Four main steps were considered: a) precursor impregnation over the support, b) drying, c) reduction of the metal precursor and d) calcination. The preparation of the OC-Ref typically involved 20 g of γ -Al₂O₃ (Sasol CATALOX® SCCa 5/200, sieved in the 125-53 μ m range), which were added into a sealed conical flask. The conical flask used had a lateral outlet connected to a 250-mmHg vacuum laboratory line. Using these materials, the following procedural steps were taken:

a) First Impregnation Step with La Addition:

- A precursor solution was prepared by dissolving 99.999% La (NO₃)₃·6H₂O (Sigma-Aldrich CAS 10277-43-7) in water.
- A precursor La solution was added drop-by-drop to the alumina particles under vacuum and under intense solid mixing, to achieve 5wt% of La loading.
- The obtained paste was dried at 140°C during 4 h, with the solid being reduced at 750°C during 8 h, in a bubbling fluidized bed with 10% H₂ balanced with Ar.

b) Second Impregnation Step with Co Addition

- A precursor solution was prepared with 99.999% pure Co (NO₃)₂·6H₂O (CAS 10026-22-9, Sigma-Aldrich) in water.
- A precursor Co solution was added drop-by-drop to the La-alumina powder under vacuum and under intense solid mixing, to achieve 1wt% of Co loading.
- The drying of the obtained paste occurred at 140°C during 4 h, with the solid being reduced at 750°C during 8 h, in a bubbling fluidized bed with 10% H₂ balanced with Ar.

c) A Third Impregnation Step with Ni Addition

- A precursor Ni solution was prepared by dissolving 99.999% Ni (NO₃)₂·6H₂O (CAS 13478-00-7, Sigma-Aldrich) in water.
- A precursor Ni solution was added drop-by-drop to the La-Co-alumina powder under vacuum and under intense solid mixing. This was done to achieve 10wt%Ni loading.
- The drying of the obtained paste took place at 140°C during 4 h, and the reduction of the solids took place at 750°C during 8 h, in a bubbling fluidized bed with 10% H₂ balanced with Ar.
- In the case of the Ni addition, the previous steps were repeated and this twice to achieve a 20wt% Ni loading. Finally calcination was performed at 750°C which yield an OC with 20wt% Ni, 1wt%Co and 5wt% La.

Unfortunately, and as reported in a previous study by Quddus et al. [14], this OC preparation led to an OC with non-negligible NiAl₂O₄ amounts formed.

5.1.2 Preparation of the Fluidizable HPOC

To circumvent the undesirable formation of NiAl₂O₄ in the OC-Ref, additional treatment steps in the OC-Ref preparation were implemented in the present study as follows: a) the OC was further treated in a tube furnace (Thermolyne 21100) with 10% H₂ balanced with Ar, b) the temperature of the furnace was increased using a 15°C/min ramp b) once 900°C reached, this temperature was kept for 1h, c) the resulting OC was calcined at 650°C.

This yielded an OC with a highly re-dispersed nickel phase with little interaction with the γ -alumina support. This new OC designated as the HPOC in the present study, provides more than 90% of the nominal oxygen lattice at temperatures between 550-650°C. The promising HPOC was characterized using XRD, BET, H₂-TPR, NH₃-TPD and pulse chemisorption as is described later in the manuscript. This methodology ensured, as will be shown in the upcoming sections of this manuscript, the complete decomposition of strongly bonded NiO on the alumina species, as well as the absence of NiAl₂O₄.

5.1.3 Characterization of OC-Ref and HPOC

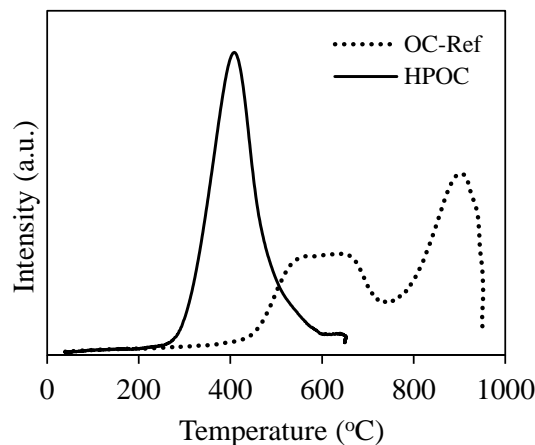


Figure 5-1: H₂-TPR Profiles for the HPOC and the Oxygen Carrier used as the Reference (OC-Ref). Operating conditions: 10% H₂-Ar, 50 cm³/min., and a temperature ramp of 15°C/min up to desired level with 10 min. holding time.

Figure 5-1 reports a typical H₂-TPR analysis. One can observe that the OC-Ref yields 45% of the available lattice oxygen only, in the 300-650°C range, requiring higher thermal levels for complete OC oxygen utilization. Exposing the OCs to thermal levels higher than of 750°C, promotes NiO transformation into NiAl₂O₄ [109,110], making the OC-Ref inherently less reliable. On the other hand, one can also observe as per the TPR for HPOC, that a H₂-uptake of 50 cm³/g was recorded in the 300-650°C range. This H₂-uptake stands close to the expected theoretical uptake value of 57 cm³/g. Thus, it is shown that the HPOC displays a valuable performance, given that it is very reactive in the targeted 300-650°C thermal range, yielding more than 90% of the available lattice oxygen as well as having an H₂-uptake close to theoretical values. It is anticipated that this lower than 650°C OC operation will prevent the formation of NiAl₂O₄.

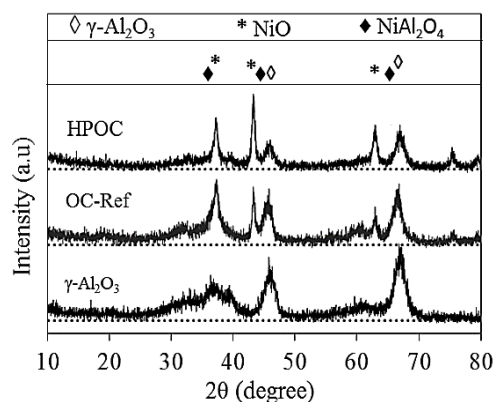


Figure 5-2: XRD Patterns for the HPOC and the OC-Ref under Oxidized State Conditions. The dotted line represents signal baseline.

Figure 5-2 compares the XRD patterns of the new HPOC and the OC-Ref including the γ - Al_2O_3 support. One can observe that smaller nickel aluminate peaks were detected for the HPOC at 37.01 and 45.1 degrees in the 2θ scale, with higher nickel oxide peaks detected at 37.29 and 43.3 degrees in the 2θ scale. This strongly suggests that NiAl_2O_4 is being transformed to NiO via the additional reduction-calcination steps recommended for the HPOC.

Table 5-1: Characterization of γ - Al_2O_3 , OC-Ref and HPOC

	γ - Al_2O_3	OC-Ref	HPOC
BET Surface Area, m^2/g	191.1	107.5	95.2
Pore Volume, cm^3/g	0.53	0.37	0.35
Avg. Pore Diameter, Å	110.2	137.7	146.8
TPR: H_2 Uptake, cm^3/g (STP)	-	54	50
TPD: NH_3 Uptake, cm^3/g (STP)	6.0	3.63	2.89
Ni Dispersion%	-	0.85	1.27
Crystal Size (nm) , d_v	-	115	77

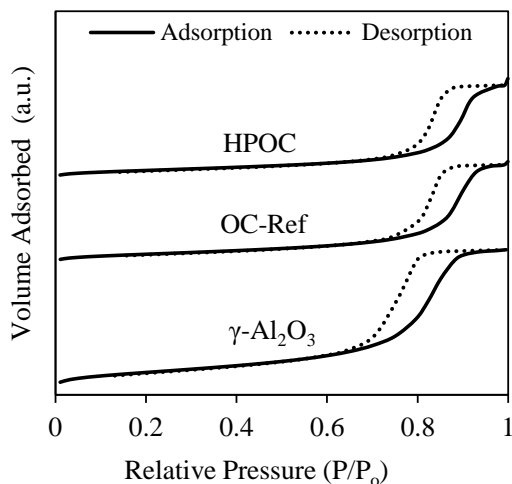


Figure 5-3: Nitrogen (N_2) adsorption–desorption isotherms for HPOC, OC-Ref and $\gamma\text{-Al}_2\text{O}_3$. All data are in the same linear scale with a shifted baseline.

Figure 5-3 reports N_2 adsorption–desorption isotherms for both the new HPOC and the previously studied OC-Ref. According to IUPAC classification, both OCs display type IV-A isotherms. This indicates larger pore width ($>4\text{nm}$), with this being consistent with the mesoporous $\gamma\text{-Al}_2\text{O}_3$ support structure [111,112]. One can also observe that due to the metal additions over the support, some structural changes are observed in the support. However, no significant structural modifications were observed when comparing the HPOC and the OC-Ref N_2 -isotherms. All isotherms showed type H1 hysteresis loops which indicate well defined cylindrical-like pore channels in solid porous materials [111].

One should note that the BET surface area is diminished from $191\text{ m}^2/\text{g}$ in the alumina support, to $95.2\text{ m}^2/\text{g}$ in the HPOC and to $107.5\text{ m}^2/\text{g}$ in the OC-Ref once the various La, Co and Ni additions, are implemented. This is accompanied, as one can see in Figure 5-4, by both a moderate increase in pore diameter and a modest reduction in pore volume. One can postulate that the La, Co and Ni additions yield losses of smaller diameter pores, given that these pores are likely blocked. This results in specific surface area and pore volume losses.

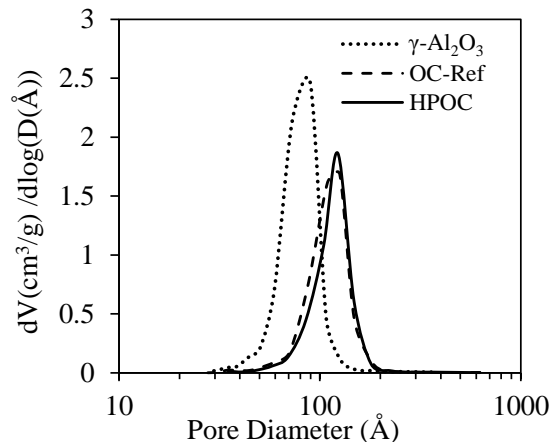


Figure 5-4: Pore Size Distribution (PSD) of the HPOC, the OC-Ref and the γ - Al_2O_3 Support Determined by the BJH Desorption Pore Volume.

Surface acidity has a great importance in CLC given that the potential acidity of the support can contribute to carbon formation. In this respect, the present study considers NH_3 -TPD to evaluate total acidity. Figure 5-5 and Table 5-1 report TPD profiles and total acidity (NH_3 uptake) for the HPOC, the OC-Ref and γ - Al_2O_3 support. NH_3 -TPD shows that the selected preparation techniques for the HPOC contribute to acidity reduction. One should note that the high NH_3 desorption peak at temperatures lower than 250°C has a potential insignificant effect on acidity for the higher than 600°C temperatures anticipated for CLC operation.

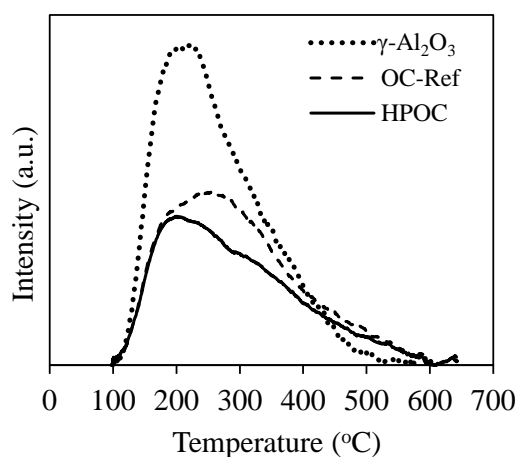


Figure 5-5: NH_3 -TPD Profiles of the HPOC, the OC-Ref and the γ - Al_2O_3 support. Notes: a) NH_3 was adsorbed at 100°C , b) NH_3 was desorbed at $20^\circ\text{C}/\text{min}$ heating rate.

5.1.4 Stability of the HPOC.

Apart from requiring structural integrity, a stable OC performance is especially important for the industrial application of the HPOC. OC particles are reduced-oxidized thousands of times during a day of operation in a CLC plant. Thus, one reliable and valuable experiment to develop is one involving consecutive TPR/TPO cycles. This is relevant in order to assess both HPOC performance and stability.

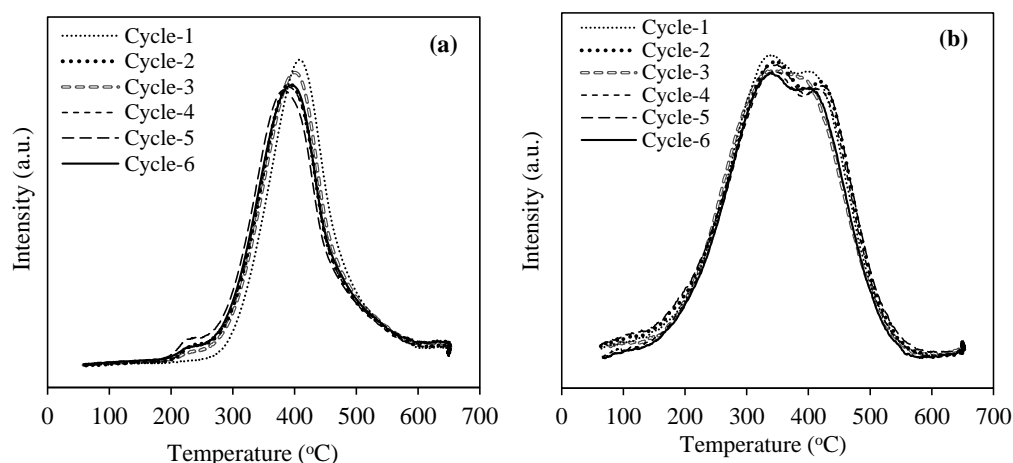


Figure 5-6: Consecutive TPR/TPO Cycles using the HPOC at 15°C/min heating rate with a flow rate 50 cm³/min. (a) TPR: 10 vol.% H₂/Ar as a reducing agent (b) TPO: 5 vol.% O₂/He as an oxidizing agent

Figure 5-6 shows that both TPR and TPO profiles display high reproducibility, in terms of total amounts of H₂ and O₂ consumed. As well, one should note the essentially unchanged TPR and TPO profiles in this diagram, with less than 2% fluctuations in H₂-uptake (50 cm³/g) and O₂-uptake (21 cm³/g).

These results corroborate the progressive transition of nickel crystals to nickel oxide crystals during oxidation and vice versa, the conversion of NiO into Ni. All this is accomplished without OC structural properties being affected. Consistent with this, one can note that the close to 400°C maximum observed peak temperatures for both reduction and oxidation, are adequate to allow fast HPOC reductions and oxidations, with these reactions being complete at desirable temperatures lower than 650°C.

5.2 Syngas CLC Test Using CREC Riser Simulator

CLC runs with the HPOC were carried out using syngas in the fluidized CREC Riser Simulator. Selected operation conditions were slightly above atmospheric pressure, with temperatures in the 550-650°C range and reaction times in between 2-40s. Two different syngas feedstock amounts were employed: a) stoichiometric amount of syngas ($\psi=1$), b) less than stoichiometric amount of syngas ($\psi=0.5$).

5.2.1 Syngas source and composition

Two types of syngas obtained from biomass gasification using a La_2O_3 promoted $\text{Ni}/\gamma\text{-Al}_2\text{O}_3$ catalyst were considered: a) a gas mixture designated as “Syngas-250” with a H_2/CO ratio of 2.5 and 50v% H_2 , 20v% CO , 10v% CH_4 , 20v% CO_2 ($\Delta H_c^\circ = -258 \text{ kJ/mol}$) [113], b) a gas mixture designated as “Syngas-133” with a H_2/CO ratio of 1.33 and 44v% H_2 , 33v% CO , 11v% CH_4 , 12v% CO_2 ($\Delta H_c^\circ = -288 \text{ kJ/mol}$). [114].

5.2.2 Pressure profile of Syngas CLC

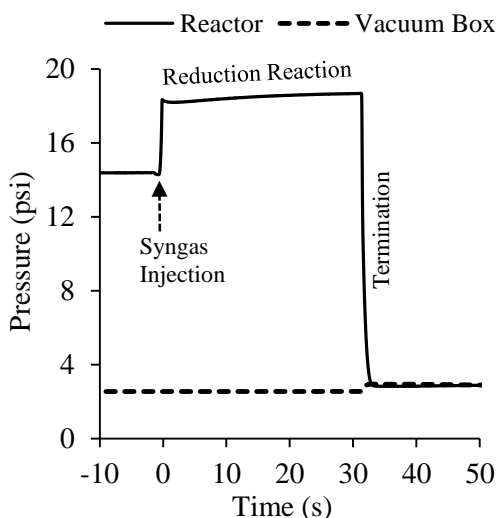
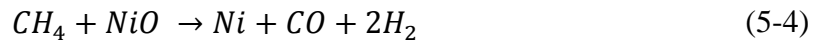
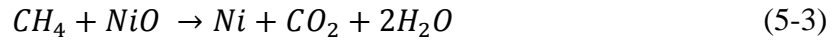
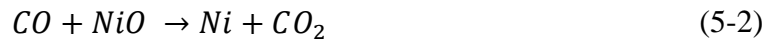


Figure 5-7: Pressure profile in CREC Riser Simulator: Reactivity test with HPOC and Syngas.

Figure 5-7 reports typical pressure profiles in CREC Riser Simulator runs with syngas reacting with the HPOC lattice oxygen. The solid line in Figure 5-7 shows the total pressure in the reactor while the broken line displays the total pressure inside the vacuum box. One can notice that the syngas injection results in a sudden total pressure increase in the reactor unit. Following the syngas

injection, the CLC reduction reaction continues for a certain period until a “termination time” is reached. At this point, all CREC Riser reactor contents except the HPOC, are evacuated towards a vacuum box.

One can also observe in Figure 5-7, that a limited total pressure rise is observed during the reduction period. This can be explained considering that: a) there was no expected molar increase via reactions (5-1) and (5-2), b) there was a modest and anticipated molar rise via reactions (5-3) and (5-4), given that the methane fraction used in the syngas is limited.



One can also see in Figure 5-7 that transfer of product species from the 50 cm³ reactor to the 1000 cm³ vacuum box, at 150°C and 3 psi, decreases the reactor pressure as well as increases mildly the vacuum box pressure. In this respect, the transfer of the product species to the vacuum box was almost instantaneous, with this preventing any further reaction from occurring. Upon completion of the sample evacuation, the product species were transferred from the vacuum box to gas chromatograph for further analysis.

5.2.3 Effect of ψ ratio and temperature

5.2.3.1 Syngas-250 (H₂/CO=2.5)

Figure 5-8 describes the CO₂ yield for $\psi=0.5$ and $\psi=1$. It can be observed that 90% CO₂ yields with the HPOC can be achieved at 600°C and 40s reaction time. Similar yields were claimed by [25,115]. However, those authors require in excess to 800°C temperatures, 900s reaction time and lower than 0.5 ψ ratios.

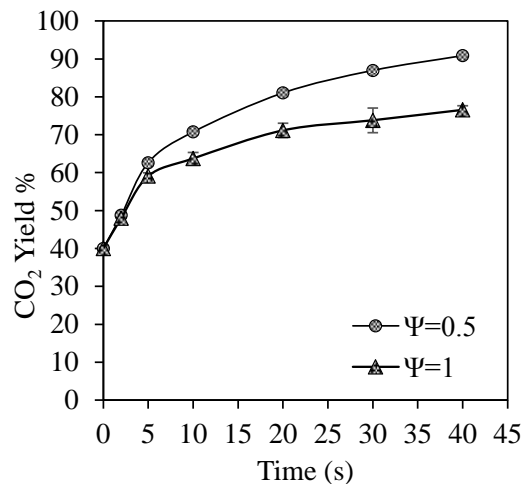


Figure 5-8: CO₂ Yield from a Syngas-250 CLC Reaction at 600° C for $\psi=0.5$ and $\psi=1$. Reported data corresponds to at least 3 repeats with vertical bars showing standard deviations.

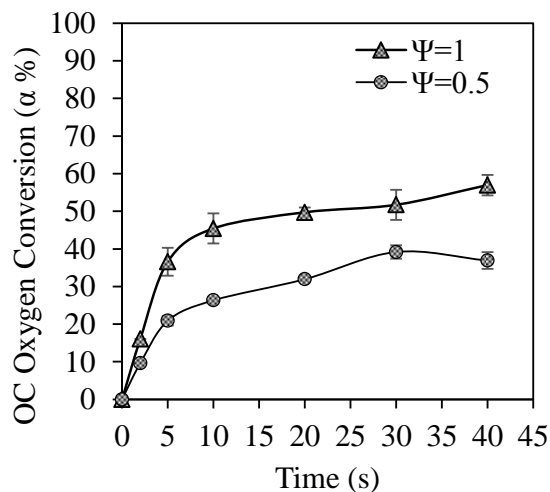


Figure 5-9: OC oxygen conversion at 600° C for $\psi=0.5$ and $\psi=1$. Reported data corresponds to at least 3 repeats with vertical bars showing standard deviations.

In the CLC processes, the extent of OC utilization is of great importance. High extent OC utilization reduces the OC solid recirculation considerably in the CLC plant. In this regard,

Figure 5-9 shows that the OC conversion depends on the ψ stoichiometric ratio. In the case of using the syngas over oxygen on OC ratios of $\psi=1$ or $\psi=0.5$, the observed OC conversion were in the 40-58% at 600°C. One should note that these OC conversions were achieved with an OC essentially free of NiAl₂O₄ species, as confirmed with TPR and XRD. These findings demonstrate

the major advantage of the proposed HPOC, versus other less stable OCs used at higher temperatures where NiAl_2O_4 species are always present [115,116].

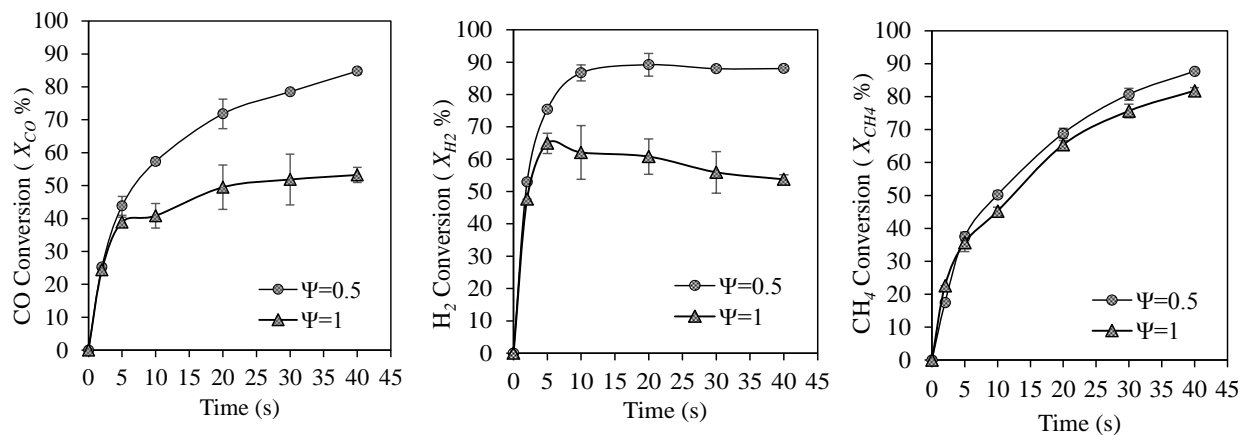


Figure 5-10: Syngas-250 Conversion (CO , H_2 and CH_4) at 600°C for $\psi=0.5$ and $\psi=1$. Reported data corresponds to at least 3 repeats with vertical bars showing standard deviations.

In CLC and from the point of view of syngas conversion, the combustion of individual species is a significant performance parameter. Figure 5-10 reports the CO , H_2 and CH_4 conversions for the $\psi=0.5$ and $\psi=1$ cases at 600°C . In both cases, $\psi=0.5$ and $\psi=1$, at 10s reaction time and below, H_2 reactivity is high. This is the case versus the much slower CO and CH_4 conversion rates. One can also notice however, that once this initial period completed, the H_2 conversion either remains unchanged ($\psi=0.5$) or is reduced slightly ($\psi=1$), while the CO and CH_4 conversions continue to increase. Thus, one can see that to take full advantage of the HPOC with significant combustion of all three-syngas species (H_2 , CO and CH_4), a reaction time of not less than 40s. is required at 600°C . It is on this basis that one can speculate that hydrogen is more prone to be oxidized by the labile surface oxygen species during the initial stages of OC usage.

However, once this labile surface oxygen is consumed, the hydrogen conversion is essentially stopped with remaining CO and CH_4 species being combusted with the OC lattice oxygen. This effect can be explained by considering a different CH_4 conversion mechanism at $\psi=1$, with the OC carrier having a significant density of oxygen deprived Ni sites. Ni species may then promote CH_4 reforming or alternatively NiO species [117] may contribute to both H_2 and CO formation via reaction (5-4). These undesirable effects can however, be circumvented with the HPOC operated at 600°C and $\psi=0.5$, as shown in Figure 5-10.

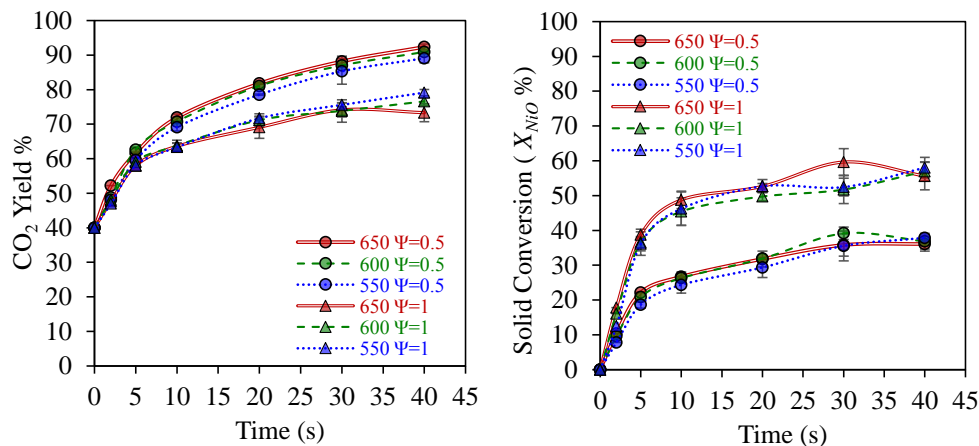


Figure 5-11: Temperature Effect on CO₂ Yield and OC oxygen conversion for $\psi=0.5$ and $\psi=1$. Reported data corresponds to at least 3 repeats with vertical bars showing standard deviations.

Figure 5-11 describes the temperature effect on CO₂ yields. It also shows the solid phase oxygen conversion in the 550 to 650°C range and when using $\psi=0.5$ and 1 ratios. One can notice that there is a significant and consistent effect of the ψ parameter ratio while the influence of thermal levels is limited. This lack of influence of the thermal levels is also apparent in the conversion of individual species forming the syngas, as shown in Figure 5-12. This suggests a combustion process dominated by the diffusion of oxygen in the Ni crystallite lattice.

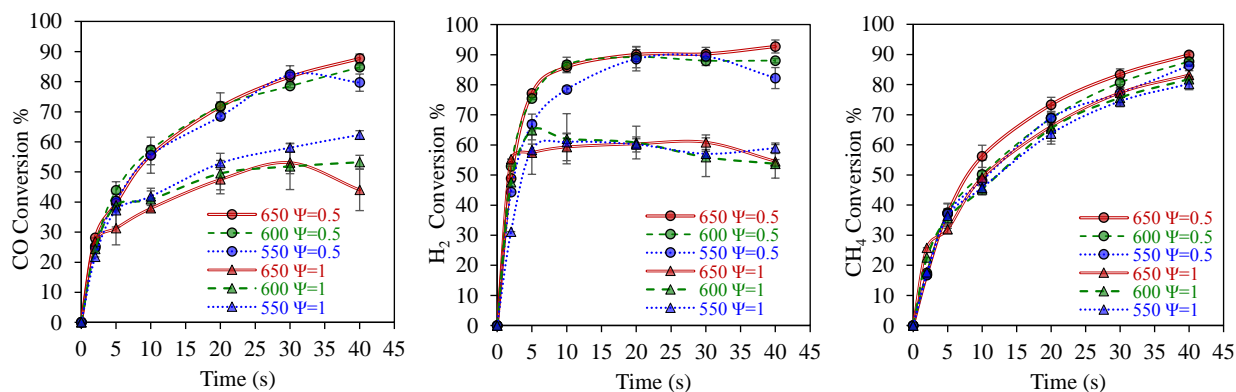


Figure 5-12: Temperature Effect on Syngas Conversion (CO, H₂ and CH₄) for $\psi=0.5$ and $\psi=1$. Reported data corresponds to at least 3 repeats with vertical bars showing standard deviations.

5.2.3.2 Syngas-133 ($H_2/CO=1.33$)

Figure 5-13 reports the CO_2 yield and the OC oxygen conversion using Syngas-133 at different temperatures (550-650°C) with different fuel to oxygen stoichiometric ratios ($\psi=0.5$ and $\psi=1$). One can observe that using a HPOC, CO_2 yields as high as 85-92% are achievable with this being a function of the temperature selected.

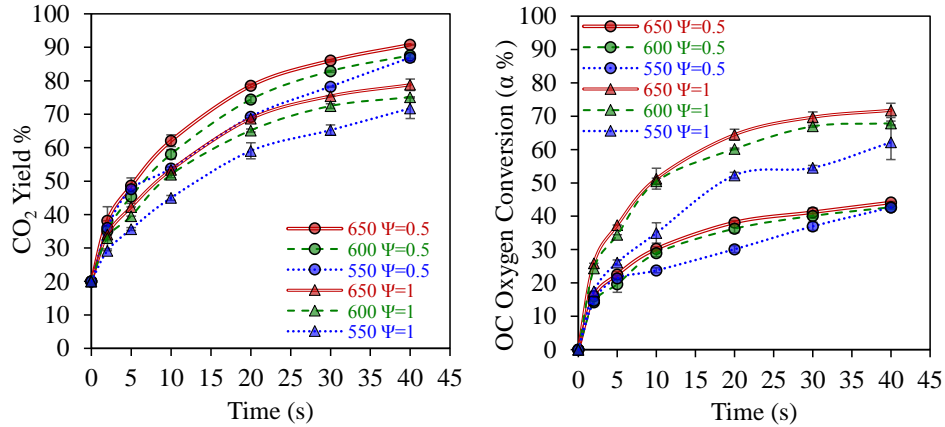


Figure 5-13: CO_2 yield and OC oxygen conversion at different temperatures and with ψ for Syngas-133. Reported data corresponds to at least three repeats with vertical bars showing standard deviations.

In particular one can notice in Figure 5-13 that for all cases reported, the overall CLC rates are moderately promoted as temperature increases and this for the two $\psi=0.5$ and $\psi=1$ stoichiometric ratios.

Figure 5-14 reports the CO_2 yields and the OC oxygen conversion for Syngas-250 CLC and Syngas-133 CLC, at 650°C and at ψ of 0.5 and 1. One can notice that the early CO_2 yields are highly affected by the initial feed compositions. However, after 20s, CO_2 yields become less dependent on the initial H_2/CO ratios with a 92% CO_2 achieved in Syngas-133 and Syngas-250.

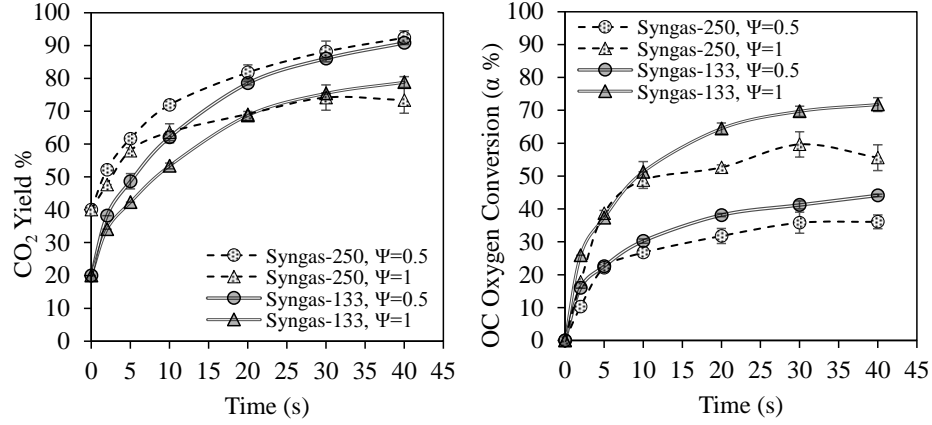


Figure 5-14: Comparison between the CO₂ yield and OC oxygen conversion for syngas-250 and syngas-133 at 650°C. Reported data corresponds to at least three repeats with vertical bars showing standard deviations.

Figure 5-15 shows that the CO, H₂ and CH₄ conversions for syngas-133 are influenced by both temperature and ψ ratio. Thus and based on these experimental results using the HPOC, it can be shown a 90% CO, H₂ and CH₄ conversion for Syngas-133 is achievable.

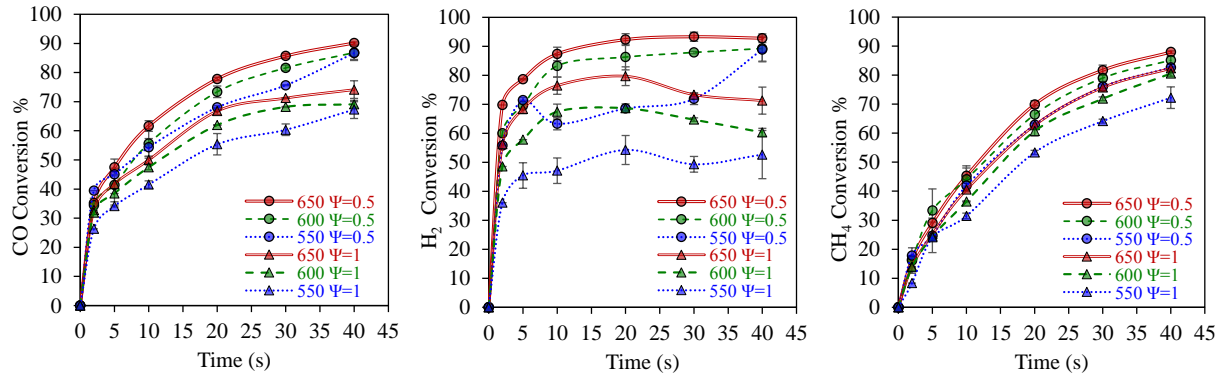


Figure 5-15: Syngas-133 conversion by CO, H₂ and CH₄ at three temperatures (550, 600 and 650 °C), and 0.5 and 1 ψ ratios. Reported data corresponds to at least 3 repeats with vertical bars showing standard deviations.

Based on the observed reaction rates, one can establish an initial order of reactivity as follows: $r_{H_2} > r_{CO} > r_{CH_4}$. However, it was observed that for larger reaction times, this order of reactivity was altered with r_{H_2} becoming in all cases smaller than the r_{CH_4} and r_{CO} consumption. This change in

the CLC rates was assigned to much lower oxygen availability in the OC, at extended reaction periods.

5.2.4 Coke deposition

Coke is a critical parameter for the CLC. Coke formation in the Fuel Reactor leads to coke being transported with the OC from the Fuel Reactor to the Air Reactor. In the Air Reactor, coke is burned forming CO₂ which leaks to the atmosphere, thus negatively affecting the CLC CO₂ capture efficiency.

In the present study, the coke formed was evaluated using a total carbon measuring device (Shimadzu TOC-V_{CPH}/SSM-5000A). Conditions considered were 600°C, 40s reaction time and both $\psi=0.5$ and 1. It was valuable to observe that the coke formed with the HPOC was insignificant in all runs, with less than 0.07wt% carbon per unit weight of OC.

In this respect, the very low coke obtained during all runs with the HPOC was assigned to the following: a) a very effective La modification, reducing support surface acidity and thus, coking as suggested by Dossumov et al. [117], b) coke formation being limited via transition coke gasification ($C+H_2O \rightarrow CO + H_2$) as suggested by Wang et al. [118].

Thus, the reported results show that the 550-650°C range provides an ample temperature range for the application of the proposed HPOC with the highest 650°C temperature level being favored to help best possible CLC plant thermal efficiency. Even though comparably high H₂, CO and CH₄ conversions may also be possible with the HPOC at higher temperatures such as 700-750°C, these thermal levels are not recommended and this to strictly limit NiAl₂O₄ formation [109] which is one of the main issues in CLC.

5.3 Conclusion

- a) A 20wt%Ni 1wt%Co 5wt%La/ γ -Al₂O₃ fluidizable and highly performing Oxygen Carrier (HPOC) was synthesized using an enhanced preparation method. This led to an OC essentially free of nickel aluminate. This was confirmed using XRD and TPR/TPO. Also

psychochemical properties were discuss based on BET N₂-adsorption isotherm, NH₃-TPD and H₂-Pulse Chemisorption.

- b) Two types of synthesis gas were used as fuel with H₂/CO=2.5 and H₂/CO=1.33 in a present study. The HPOC showed excellent performances with either syngas at a stoichiometric ratio of $\psi=0.5$. The reaction produced a high CO₂ yield (92%), CO conversion (90%), H₂ conversion (95%) and CH₄ conversion (91%). Moreover, the observed.
- c) The HPOC at $\psi=0.5$ stoichiometric ratio, 650°C and 40s reaction time led to 40% OC oxygen conversion provided that maximum theoretical conversion is 50%.
- d) The HPOC yielded coke in minute amounts in all cases (< 0.07wt %).
- e) The HPOC showed little influence of thermal levels (550-650°C) on CLC performance. These findings point towards a CLC dominated by oxygen lattice diffusion.

CHAPTER 6 KINETIC MODELLING

This chapter covers both the thermodynamics of CLC and the kinetic model developed for a highly performing nickel-based oxygen carrier (HPOC). This HPOC is free of nickel aluminates and can perform very efficiently at lower temperatures (i.e. 550-650°C).

In this study, a kinetic model is proposed to predict syngas chemical looping combustion (CLC) using a HPOC. The syngas used in this study, emulates the syngas that can be derived from biomass gasification containing H_2 , CO, CH_4 and CO_2 . To establish the kinetic model, isothermal runs are developed in the CREC Riser Simulator, which is a mini-batch fluidized bed reactor. The operating conditions are varied between 2-40s reaction times and 550-650°C, with the H_2/CO ratio being 2.5 and 1.33 and the ψ fuel to HPOC stoichiometric ratio being 0.5 and 1. The solid-state kinetics considered uses of a Nucleation and Nuclei Growth Model (NNGM). The proposed kinetics leads to a model with ten independent intrinsic kinetic parameters. The various kinetic parameters are determined via numerical regression within a 95% confidence interval and small cross correlation coefficients. According to the frequency factors obtained, the reactivity of the species with a HPOC can be expressed following the $H_2 > CO > CH_4$ order. Given that the HPOC shows high performance and stability, it is anticipated that the developed kinetic model could contribute to establishing large-scale reactor CLC for syngas combustion. As a precedent to this work, the CHAPTER 5 described the preparation, characterization and performance evaluation of this highly performing oxygen carrier.

Figure 6-1 illustrates the value of experimentation with the CREC Riser Simulator for the determination of a reaction mechanism and the development of a kinetic model. Additional details describing how the CREC Riser Simulator can be used for OC evaluation can be found in technical report [119,120].

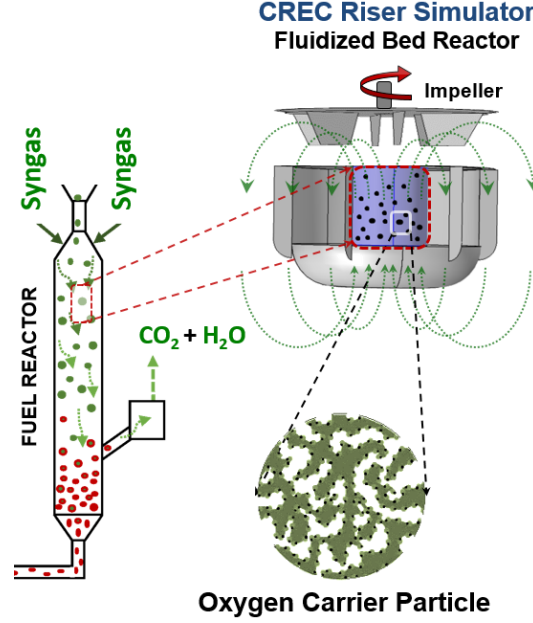


Figure 6-1: Schematic diagram illustrating the value of CREC Riser Simulator experiments for the development of a kinetic model applicable in a downer reactor unit.

6.1 Rate Limiting Steps

Gamma alumina is a good porous support reported for Ni. The CLC reduction of this heterogeneous oxygen carrier involves a multistep process. The solid reduction rate may also include: a) internal and external diffusion, b) reacting species adsorption and intrinsic reaction steps. Thus, it is important to determine if the rate-limiting step is dependent on particle size and physicochemical properties.

The potential OC particle external mass transfer influence can be neglected under the CREC Riser Simulator reactor operating conditions. This is the case, given the high gas superficial velocities [120], with $f_{r,i} \gg (-r_{exp})$, where, $f_{r,i}$ refers to the radial flux of the gaseous species “ i ” as described by eq. (6-1):

$$f_{r,i} = k_g (C_{b,i} - C_{s,i}) \quad (6-1)$$

$$(-r_{exp}) = \frac{N_0}{wS_{ex}} \frac{d\alpha}{dt} \quad (6-2)$$

with $C_{b,i}$ and $C_{s,i}$ represent the gas species concentrations at bulk and at the external surface of the particle, respectively.

The calculation of the $f_{r,i}$ also requires one to know the k_g mass transfer coefficient. This can be evaluated as $k_g = Sh D_{iA}/d_p$; where, Sh is the Sherwood number, D_{iA} stands for the species diffusion coefficient in argon and d_p denotes the mean OC particle diameter. D_{iA} can be evaluated using the Fuller Correlation [121,122]. The Sherwood number can be calculated using the Frossling's correlation, $Sh = 2 + 0.6Re^{0.5}Sc^{0.33}$, where, Re is Reynolds number and Sc is Schmidt number.

One possible approach is to set k_g at its lowest possible value, using $Sh=2$. This corresponds to the stagnant fluid around an OC particle model. Furthermore, the $(-r_{exp})$ as in eq. (6-2), can be calculated from the experimental data, with N_0 being the number of consumable oxygen moles in the OC, α standing for the OC oxygen conversion, S_{ex} denoting the external surface area per gram of sample and w representing the weight of OC. On this basis, the $f_{r,i} > (-r_{exp})$ condition can be confirmed and the influence of the external mass transfer neglected.

In order to calculate the possible internal mass transfer influence on the CLC rate, the Weisz-Prater measure can be used [123,124]. According to this, there is no internal mass transfer resistance when $C_{WP} \ll 1$. C_{WP} is a dimensionless number as shown in eq. (6-3), with ρ_{OC} being the OC apparent particle density and with D_{eff} being the effective diffusivity considered as $0.1D_{iA}$ [124]:

$$C_{WP} = \frac{(-r_{exp})S_{ex}\rho_{OC}(0.5d_p)^2}{D_{eff}C_{s,i}} \quad (6-3)$$

Table 6-1: Parameters Used to Determine the Negligible External and Internal Mass Transfer Limitations for the HPOC of the Present Study

	H ₂	CO	CH ₄
$f_{r,i}$ (mol/m ² /s)	39	5.2	1.9
$(-r_{exp})$ (mol/m ² /s)	1.56×10^{-5}	1.2×10^{-5}	3.9×10^{-6}
$C_{b,i}$ (mol/m ³)	3.2	2.4	0.8
k_g (m/s)	12.16	2.17	2.36
D_{AB} (m ² /s)	5.29×10^{-4}	9.45×10^{-5}	1.03×10^{-4}
N_0 , (mole) $\times 10^{-6}$	160	120	40
C_{WP}	0.028	0.154	0.142
Other Parameters: $T=600^\circ\text{C}$, $P=20$ psi, $D_p=87$ μm , $dX_p/dt=1.5$ s ⁻¹ , $w=175$ mg, $S_{ex}=87.8$ m ² /g			

Table 6-1 illustrates that for the HPOC runs of the present study, $f_{r,i} > (-r_{exp})$. Thus, no influence of the external mass transfer can be assigned to the CLC rates. Furthermore, $C_{s,i} = C_{b,i}$ can also be postulated. Given that $C_{WP} \ll 1$, a negligible internal diffusion in the overall CLC rate can be assumed. Thus, and as a result, the kinetic data obtained in the present study, represents the CLC intrinsic kinetics. On this basis, kinetic modeling can be developed.

6.2 Thermodynamic Equilibrium Analysis

A set of equilibrium compositions were determined for syngas and NiO reactions using equilibrium constants as discussed in CHAPTER 1. A stoichiometric amount of NiO oxygen carrier was used expecting full combustion into CO₂ and H₂O. Seven unknowns were found (i.e. mole fraction of CH₄, H₂, H₂O, CO₂, CO, Ni and NiO) at equilibrium condition. In determining seven unknowns, three independent reactions (i.e. 1, 2 and 4 in Figure 1-3) and four atomic balances (i.e. C, H, O and Ni) were accounted. Once the degree of freedom is zero the complete system of equations were solved using Matlab non-linear system solver, “fsolve”. Eventually the solution provides equilibrium compositions of all compounds.

Similar analysis was done with non-stoichiometric approach (Gibbs free energy minimization) using ASPEN Plus and compared with the results generated in Matlab. This was essential for the

verification and validation of reaction consideration in thermodynamic model. The non-stoichiometric analysis also accounted the existence of carbon formation during reaction.

Figure 6-2a illustrates that thermodynamically above 300°C unconverted CO (0.05 to 0.9 mol%) and H₂ (0.3 to 0.75 mol%) are found with augmented trend by temperature increase. In addition above 300°C there is no unconverted CH₄ (see Figure 6-2b), which is a very promising outcome of NiO oxygen carrier application in CLC.

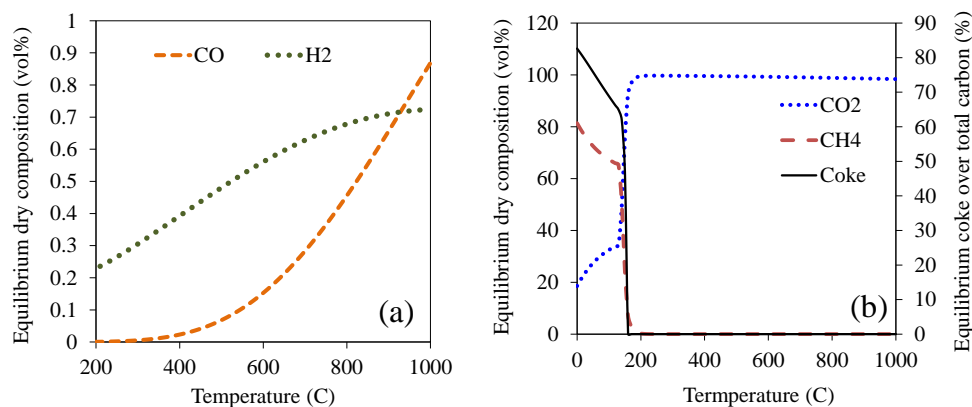


Figure 6-2: Equilibrium dry gas composition of NiO-Syngas system at 1 atm (a) CO and H₂ vol% (b) CO₂, CH₄ and Coke mole % (Syngas: 20% CO, 10% CH₄, 20% CO₂, 50% H₂ by mol)

Figure 6-2b also predicts the chemical equilibrium carbon formation of total equilibrium carbon which is 50 to 80% at less than 150°C. One can notice that there is no expected equilibrium carbon formation at above 150°C. Nevertheless, in practice lack of complete fuel oxidation, high acidity of OC support and tendency of reduced metal exposure can cause carbon deposition.

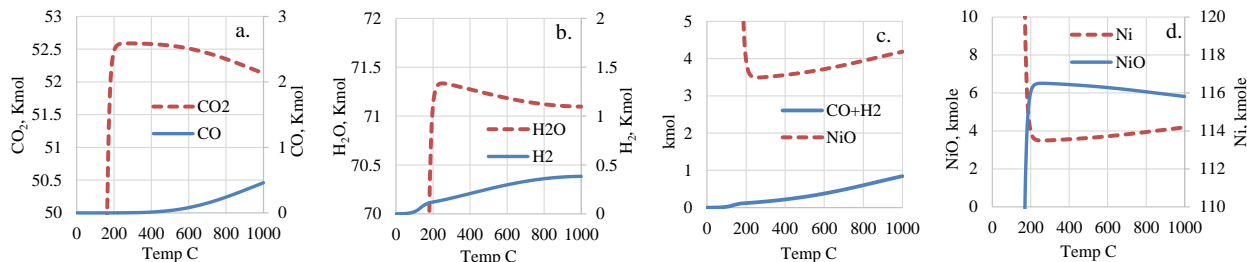
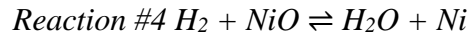
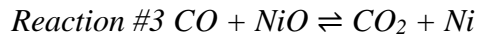


Figure 6-3 : Comparison of change in equilibrium amount of compounds by temperatures.

Figure 6-5 reports the temperature effect on equilibrium mole amount of Ni, NiO, CO, H₂, CO₂ and H₂O. This helps to understand the responsible reactions for having unconverted CO and H₂ moles at equilibrium.

Figure 6-5a and Figure 6-5b show the change in CO and H₂ mole is only related to CO₂ and H₂O respectively. Essentially Figure 6-5c depicts a decrease of Ni by increase of NiO. Also, Figure 6-5d indicates a combined change in CO and H₂ mole that is completely dependent on the NiO mole change. Considering all these perspective, one could argue that the unconverted CO and H₂ are the resultants from the equilibrium reactions of 3 and 4 as follows.



6.3 Kinetic Model Assumptions

OC reduction involves solid and gas phase species accounting for: a) the OC solid-phase change given the lattice oxygen depletion, b) The gas-phase chemical species changes as a result of various inter-conversions reactions including those with lattice oxygen. Thus, an adequate kinetic model has to be formulated to describe these phenomena.

Changes in the OC can be described using the Avrami-Erofeev NNGM Model with random nucleation ($n=1$) [65,125]. Eq. (6-4) refers to the function $f(\alpha)$, which describes the solid-phase oxygen changes, with n being the Avrami exponent:

$$f(\alpha) = n(1 - \alpha)[- \ln(1 - \alpha)]^{\frac{n-1}{n}} \quad (6-4)$$

As well the influence of the gas-phase species can be accounted in terms of species partial pressures. As a result, OC reduction involves several simultaneous reactions which are influenced by both the gas-phase reducing agent and by the OC properties [67,126].

In this respect, and in the CLC of syngas, the H₂ and CO are directly converted into H₂O and CO₂ due to their high reactivity. Furthermore, as the reaction proceeds, the reduced OC shows less available NiO exposed sites. Thus, and according to the technical literature, thermodynamic

chemical equilibrium may be reached under experimental conditions [127–129]. One can thus postulate, that chemical equilibrium may influence syngas conversion kinetics.

Figure 6-4 illustrates the overall CLC reaction mechanism on the HPOC surface providing an insight on the interactions of gas phase species such as H₂, CO and CH₄ with OC oxygen lattice.

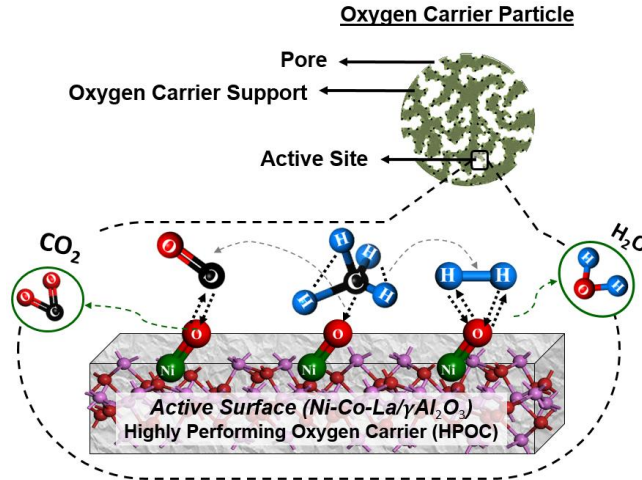
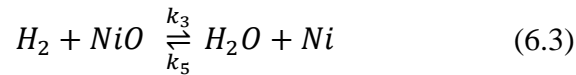
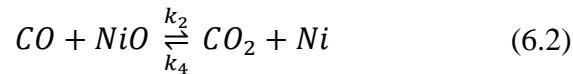
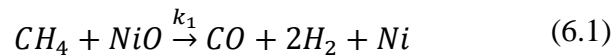


Figure 6-4: Description of the reaction mechanism on the HPOC Surface describing various interaction of H₂, CO and CH₄ with OC oxygen lattice

Furthermore, regarding CH₄ conversion with the HPOC free of nickel aluminate, one can observe: a) A dominant formation of H₂ and CO from CH₄ as described by reaction (6.1), b) a subsequent H₂ and CO formation after reactions (6.2) and (6.3).



One should notice that the nickel catalytic effect is strongly dependent on the availability of the lattice oxygen in the OC. When using the HPOC, metal dispersion is limited to 2%. This suggests that even at OC partially reduced conditions, it is unlikely that a single atom of nickel will be formed without neighboring nickel oxide sites being present.

Furthermore, carbon formation is an indicator of the Ni catalytic reaction effect. However, one can consider that if the oxygen conversion in the OC is limited to less than 80%, it is unlikely that the catalytic reactions leading to carbon formation will have activated [130]. Hence, one can suggest that if this condition is adhered to, the Ni catalytic influence will be negligible and will not need to be included in the kinetic model.

6.4 Kinetic Model Development

The CH₄, CO and H₂ reactions with nickel oxide can be considered as first order reactions, as reported by several authors [27,57,67]. As well, the reverse contribution of CO₂ and H₂O reactions, in the presence of Ni crystallites, can be postulated as being of first order [127,128].

Thus, a general reaction rate expression can be written as in eq. (6-5), accounting for both solid-phase oxygen conversion and individual gas-phase chemical species partial pressures. In this equation, r stands for the reaction rate, $k(T)$ denotes a temperature dependent apparent kinetic rate constant and P_i represents the partial pressure of “ i ” chemical species.

$$r = k(T)P_i f(\alpha) \quad (6-5)$$

In particular, the kinetic rate constant (k) can be expressed using the Arrhenius equation as, $k(T) = k_{0,i}^{app} e^{\frac{-E_i^{app} \times 10^3}{R} \left(\frac{1}{T} - \frac{1}{T_c} \right)}$ where, $k_{0,i}^{app}$ is the pre-exponential factor, E_i^{app} is apparent activation energy and T_c is the centering temperature. The use of T_c reduces the cross-correlation between kinetic parameters.

Considering NNGM random nucleation ($n=1$), and combining the resulting eq. (6-4) with eq. (6-5), the rate expression for reaction (6.1) can be written as in eq. (6-6). Using the same methodology, reaction (6.2) and (6.3) can be expressed by the eqs. (6-7) and (6-8), respectively as:

$$r_1 = k_1 P_{CH_4} (1 - \alpha) \quad (6-6)$$

$$r_2 - r_4 = k_2 P_{CO} (1 - \alpha) - k_4 P_{CO_2} \alpha \quad (6-7)$$

$$r_3 - r_5 = k_3 P_{H_2} (1 - \alpha) - k_5 P_{H_2O} \alpha \quad (6-8)$$

where, r_2 refers to the forward rate and r_4 stands for to the backward rate of reaction (3.2). As well, r_3 and r_5 refer to forward and backward rates of reaction (6.3), respectively.

In order to establish the postulated model, reduction reactions were conducted in CREC Riser Simulator. As discussed before in Section 6.1, and while assessing the overall CLC rate of reaction, one can determine that the external and internal mass transfer influence can be neglected. Hence, the change in chemical species only depends on the intrinsic reaction ($-r_n$) and can be expressed as:

$$(-r_i) = \frac{1}{V_R} \frac{dn_i}{dt} = \frac{1}{V_R} \frac{d\left(\frac{V_R P_i}{RT}\right)}{dt} \times \frac{101325}{14.7} \quad (6-9)$$

where, n_i represents the moles of “ i ” species ($\mu mole$), V_R is the reactor volume (cm^3), P_i stands for the partial pressure (psi), R denotes the universal gas constant ($J/mol/K$), T represents the reactor temperature (K) and t is reaction time (s). As the V_R and T are constant in each run performed, eq. (6-9) can be rewritten in terms of individual chemical species partial pressures as follows:

$$\frac{dP_i}{dt} = \frac{1}{f_1} \sum_i (-r_i); \text{ where, } f_1 = \frac{1}{RT} \times \frac{101325}{14.7} \quad (6-10)$$

Furthermore, combining eq. (6-6) with eq. (6-8) and eq. (6-10) leads to eqs. (6-11) to (6-15). Eq. (6-16) describes the total change in α , with N_{NiO}^0 being the initial nickel oxide amount ($mole$) in the OC.

$$\frac{dP_{CO}}{dt} = (r_1 - r_2 + r_4) \times \frac{1}{f_1} \quad (6-11)$$

$$\frac{dP_{CH_4}}{dt} = -r_1 \times \frac{1}{f_1} \quad (6-12)$$

$$\frac{dP_{CO_2}}{dt} = (r_2 - r_4) \times \frac{1}{f_1} \quad (6-13)$$

$$\frac{dP_{H_2}}{dt} = (2r_1 - r_3 + r_5) \times \frac{1}{f_1} \quad (6-14)$$

$$\frac{dP_{H_2O}}{dt} = (r_3 - r_5) \times \frac{1}{f_1} \quad (6-15)$$

$$\frac{d\alpha}{dt} = (r_1 + r_2 + r_3 - r_4 - r_5) \times \frac{V_R \times 10^{-6}}{N_{NiO}^0} \quad (6-16)$$

6.5 Numerical Method Used

Given eqs. (6-11) to (6-16), the $k_{0,i}^{app}$ and E_i^{app} kinetic parameters were determined numerically as follows: a) First, the initial parameter values were assigned and the set of ordinary differential equations were solved using the “ode45” function of MATLAB, b) Following this, the kinetic parameters were adjusted and optimized by using a non-linear parameter optimization tool “lsqnonlin”, with the “trust-region-reflective” algorithm minimizing the objective function (f_{obj}):

$$f_{obj} = \sqrt{\sum_i^{species} (P_{i,exp} - P_{i,th})^2 + (\alpha_{exp} - \alpha_{th})^2} \quad (6-17)$$

where, $P_{i,exp}$ and $P_{i,th}$ are the partial pressures of component “ i ” ($i = CH_4, CO, CO_2, H_2$ and H_2O species) observed experimentally and predicted via the kinetic model, respectively. Furthermore, $\alpha_{i,exp}$ denotes the experimental OC oxygen conversion while $\alpha_{i,th}$ is the theoretical OC oxygen conversion.

Regarding the numerical calculation development, the algorithm was used to minimize the error between the theoretical model and the experimental observations (>250 average data points). This was done to achieve 95% confidence intervals. Pre-exponential factors and activation energies for each reaction were all bound to remain positive during calculations. Cross-correlation coefficient matrices were also established. This was done to understand the mutual dependency between calculated kinetic parameters.

6.6 Results and Discussions

6.6.1 Estimated Kinetic Parameters

In this study, the kinetic parameters were assessed based on HPOC experimental data for CLC using both Syngas-250 and Syngas-133, separately. Table 6-2 reports the estimated parameters determined with low 95% confidence spans. One should note that the ten kinetic parameters were determined using 250 average observed data points, with at least 3 repeats for each experiment and a degree of freedom (DOF) of 240.

In Table 6-2 the k_1^0 , k_2^0 , k_3^0 frequency factors correspond to (6.1), (6.2) and (6.3) forward reactions. This shows that $k_1^0 < k_2^0 < k_3^0$ is consistent with the initially observed CLC reactivity difference described above, with this being $r_{H_2} > r_{CO} > r_{CH_4}$. Furthermore and regarding the backward reactions, the k_4^0 and k_5^0 display a $k_4^0 < k_5^0$ difference, showing that H_2O displays a higher reactivity than CO_2 on nickel sites. In other words, the retardation rates due to the reverse reactions are more significant for H_2 than for CO .

Table 6-2: Kinetic Parameters Determined for Syngas-250 and Syngas-133, Separately

Apparent Parameters	Syngas-250		Syngas-133	
	Value	95% CI	Value	95% CI
$k_{0,1}^a$	3.03×10^{-2}	$\pm 4.85 \times 10^{-3}$	5.62×10^{-2}	$\pm 10.1 \times 10^{-3}$
$k_{0,2}$	12.5×10^{-2}	$\pm 18.7 \times 10^{-3}$	10.5×10^{-2}	$\pm 12.2 \times 10^{-3}$
$k_{0,3}$	29.8×10^{-2}	$\pm 21.3 \times 10^{-3}$	39.7×10^{-2}	$\pm 42.4 \times 10^{-3}$
$k_{0,4}$	2.94×10^{-2}	$\pm 9.42 \times 10^{-3}$	1.54×10^{-2}	$\pm 5.59 \times 10^{-3}$
$k_{0,5}$	19.1×10^{-2}	$\pm 22.1 \times 10^{-3}$	8.9×10^{-2}	$\pm 12.6 \times 10^{-3}$
E_1^b	3.6×10^{-13}	$\pm 2.1 \times 10^{-14}$	4.02×10^{-14}	$\pm 1.1 \times 10^{-14}$
E_2	13.02	± 5.8	5.13	± 2.9
E_3	20.10	± 6.9	7.36	± 3.6
E_4	40.17	± 12.2	36.90	± 14.4
E_5	30.31	± 10.8	21.23	± 7.8
m	250			
DOF	240			

^a $mol.m^{-3}psi^{-1}s^{-1}$; ^b $kJmol^{-1}$; $T_c=873K$; Degree of Freedom (DOF)= data points

(m) – parameters (p)= 250 – 10= 240

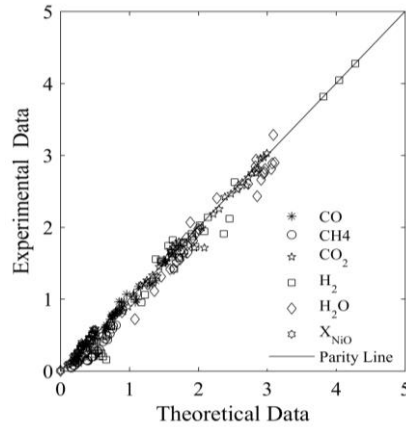


Figure 6-5: Parity plot comparing experimental chemical species partial pressures with model predictions using Syngas-250 and HPOC. Data: 250 average data points for at least 3 repeats runs. Note: standard deviation=2.9%.

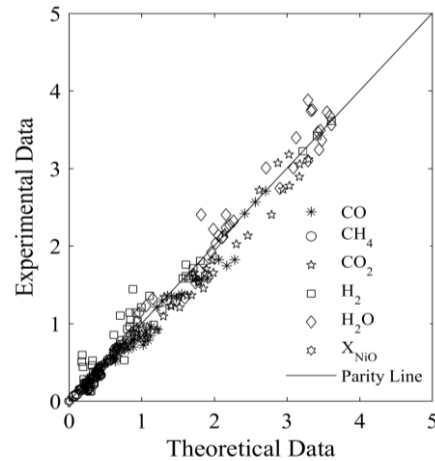


Figure 6-6: Parity plot comparing experimental chemical species partial pressures with model predictions using Syngas-133 and HPOC. Data: 250 average data points for at least 3 repeats runs. Note: standard deviation=3.9%.

Figure 6-5 and Figure 6-6 present parity plots for Syngas-250 and Syngas-133, respectively. These figures compare predicted and experimentally observed values for chemical species partial pressures at different reaction times, temperatures and ψ ratios. One can observe that the Syngas-250 shows a standard deviation error of 2.9% while Syngas-133 shows a deviation error of 3.9%. Both of these deviations are considered acceptable and within the anticipated experimental error level. Thus, the estimated parameters and the kinetic model using either of the two syngas samples are considered adequate for the CLC using the HPOC.

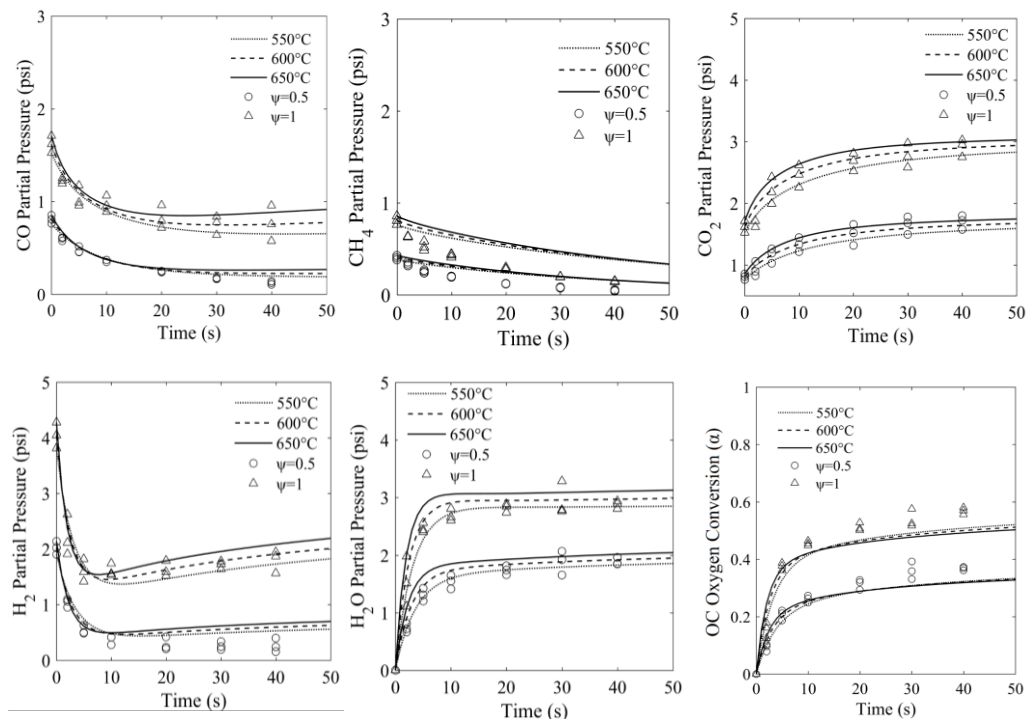


Figure 6-7: Comparison of experimental chemical species partial pressures with those of model predictions at various conditions using the Syngas-250 Feed and a HPOC.

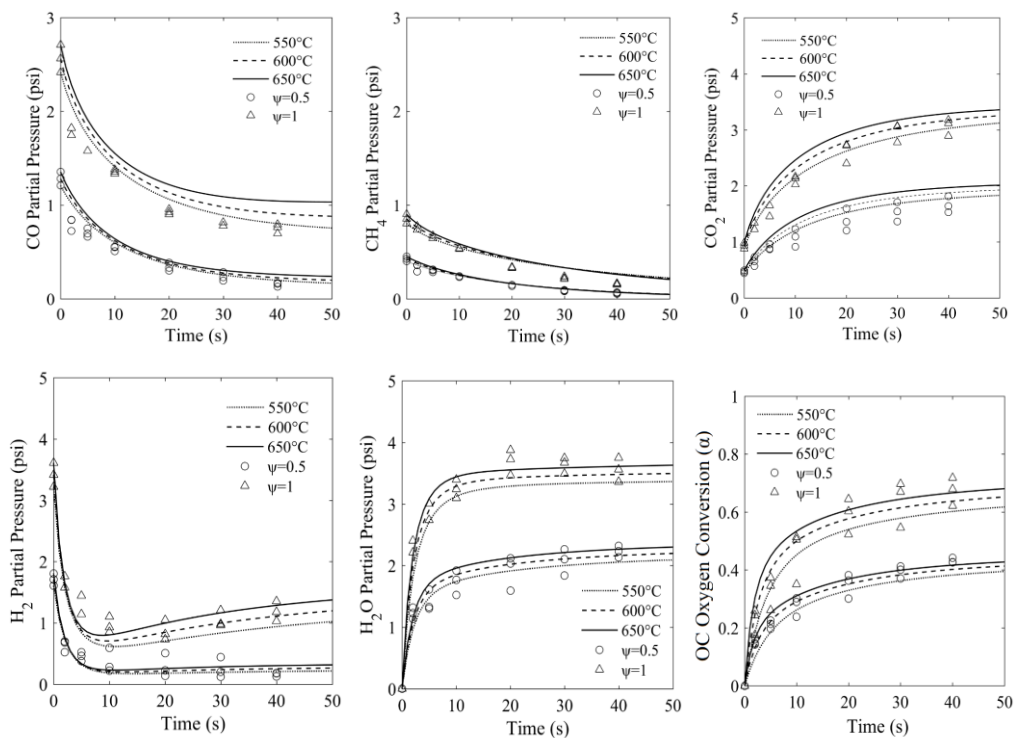


Figure 6-8: Comparison of experimental chemical species partial pressures with those of model predictions at various conditions using Syngas-133 Feed and a HPOC

Furthermore, Figure 6-7 and Figure 6-8 illustrate the predicted partial pressures using the estimated kinetic parameters for both Syngas-250 and Syngas-133 and compare with experimental results. This comparison was developed at various reaction times. Thus, it appears that the proposed kinetics and the estimated kinetic parameters are able to fit the chemical species partial pressures well. This is the case for the entire range of reaction times, with no error bias observed for some specific reaction times.

6.6.2 Model Verification and Validation

This research considered the applicability of a CLC kinetic model for a HPOC using both Syngas-250 and Syngas-133 with H₂/CO ratios of 1.33 and 2.5, respectively. In principle, if the proposed kinetic model is adequate, it must be applicable for both Syngas-250 and Syngas-133, with a single set of kinetic parameters. To validate this, a single set of kinetic parameters was estimated using all of the experimental data of Syngas-250 and Syngas-133, simultaneously.

Table 6-3: Summary of Apparent Intrinsic Kinetic Parameters for the Proposed Kinetic Model and Cross-correlation Matrix

Apparent Parameters	Value	95% CI	Correlation matrix									
			$k_{0,1}^a$	$k_{0,2}$	$k_{0,3}$	$k_{0,4}$	$k_{0,5}$	E_1^b	E_2	E_3	E_4	E_5
$k_{0,1}^a$	4.16×10^{-2}	$\pm 7.3 \times 10^{-3}$	1									
$k_{0,2}$	10.3×10^{-2}	$\pm 13.5 \times 10^{-3}$	0.14	1								
$k_{0,3}$	33.2×10^{-2}	$\pm 28.9 \times 10^{-3}$	0.06	0.16	1							
$k_{0,4}$	1.86×10^{-2}	$\pm 6.87 \times 10^{-3}$	0.00	0.76	0.13	1						
$k_{0,5}$	13.4×10^{-2}	$\pm 17.2 \times 10^{-3}$	-0.13	0.06	0.70	0.21	1					
E_1^b	4.4×10^{-7}	$\pm 3.2 \times 10^{-8}$	-0.06	-0.01	-0.01	-0.01	0.01	1				
E_2	3.89	± 2.1	-0.01	-0.01	0.01	-0.15	0.02	0.14	1			
E_3	9.85	± 4.4	-0.01	0.01	0.05	-0.02	-0.04	0.07	0.16	1		
E_4	37.13	± 11.5	-0.01	-0.16	-0.02	-0.39	-0.06	-0.01	0.75	0.12	1	
E_5	23.48	± 9.7	0.00	0.01	0.02	-0.04	0.01	-0.13	0.05	0.70	0.21	1
m	500	$^a \text{mol.m}^{-3} \text{psi}^{-1} \text{s}^{-1}$; $^b \text{kJmol}^{-1}$; $T_c = 873 \text{K}$; Degree of freedom (DOF) = data points (m) – parameters (p) = 500										
DOF	490	– 10 = 490										

Table 6-3 reports the single set of kinetic parameters including a 95% confidence interval. The ten model parameters are determined by 500 observed data points, averaged with at least 3 repeats of each experiment with a degree of freedom (DOF) of 490. One can notice that the 95% confidence spans are limited. Table 6-3 also presents the cross-correlation matrix for the kinetic parameters with most values being below 0.21 and none being more than 0.75. This shows the lack of dependence of calculated kinetic parameters. Thus and as a result, one can conclude that the kinetic

model proposed can predict the HPOC performance when using a significant range of syngas compositions.

Table 6-3 reports a very low E_1 energy of activation for CH_4 in CLC. Furthermore, it has been reported in the technical literature that E_1 may change in the 5-50 kJ/mol range [65,69,126], with the lowest observed values being for OCs free of nickel aluminate. This is consistent with the low E_1 observed for the HPOC free of nickel aluminate.

Concerning the E_2 and E_3 constants for CO and H_2 CLC, one can note that the magnitude of the determined energies of activation are in the range of reported values for the OC free of nickel aluminate [69,131] as well. Furthermore, and for the reverse reactions (6.2) and (6.3), the CO_2 conversion displayed a higher activation energy than the H_2O conversion.

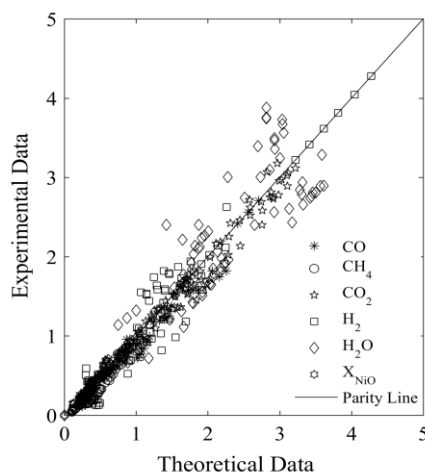


Figure 6-9: Parity plot comparing the experimental chemical species partial pressures with model predictions for both Syngas-250 and Syngas-133. Data base: 500 averaged data points for at least 3 repeat runs. Note: Standard Deviation=5.4%.

Figure 6-9 compares the predicted partial pressures with the experimental observations, using the proposed kinetic model predictions for the HOPC and both Syngas-250 and Syngas-133. One can notice that the ensemble of data including the 500 data points show a standard deviation of 5.4%. Nevertheless, one can also observe that when one eliminates the 15 data points considered outlier data from the analysis, the standard deviation is reduced to 2%.

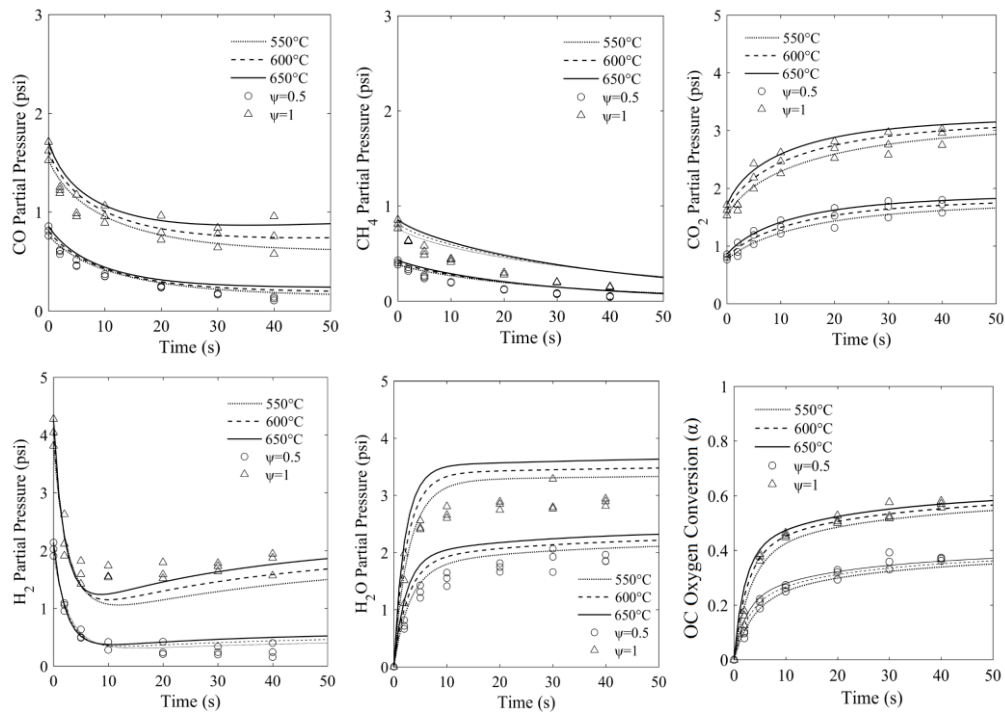


Figure 6-10: Comparison of experimental data and model predictions using the HPOC of this study and Syngas-250. Note: Parameters estimated use both Syngas-250 and Syngas-133 data.

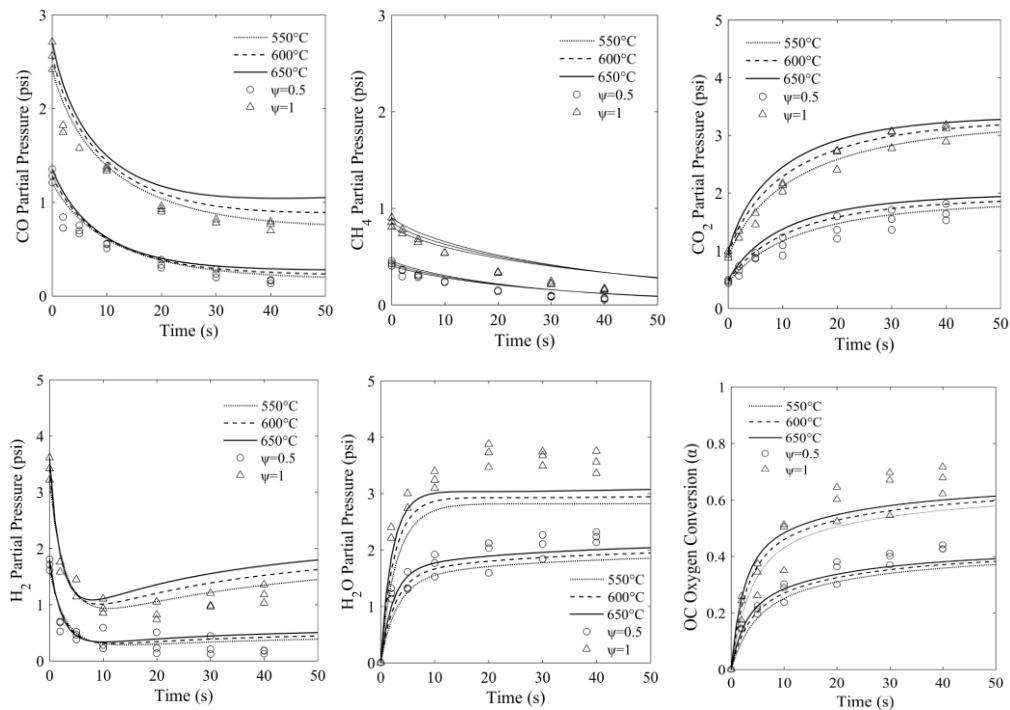


Figure 6-11: Comparison of Experimental Data and Model Predictions using the HPOC of this Study and Syngas-133. Note: Parameters estimated use both Syngas-250 and Syngas-133 data.

Figure 6-10 and Figure 6-11 describe the chemical species partial pressure changes for Syngas-250 and Syngas-133 CLC when using the HPOC of this study at various reaction times. It appears that for the CLC of the two types of syngas studied, a single set of kinetic parameters can provide excellent fitting with no observable increased errors at some specific reaction times or conditions. Thus, the proposed phenomenological kinetics appears to be a trustable model for syngas CLC rates using the HPOC of this study. This kinetic model is demonstrated to be applicable in an ample range of operating conditions. This makes the model a valuable tool for the CLC simulation of larger circulating fluidized bed units.

6.7 Conclusions

- a) A new 20wt%Ni 1wt%Co 5wt%La / γ -Al₂O₃, free of aluminate high oxygen carrier (HPOC) was successfully developed and tested with syngas in a CREC Riser Simulator reactor in the 550-650°C range. This syngas composition was the one anticipated from biomass gasification. The results are discussed in CHAPTER 5.
- b) Based on the experimental data obtained, a kinetic model was proposed for syngas CLC using the HPOC of the present study. The depletion of the lattice oxygen was described using the Avrami-Erofeev NNGM Model with random nucleation, while the CH₄, H₂ and CO consumption was accounted for via simultaneous heterogeneous gas-solid reactions.
- c) The resulting kinetic model involved ten parameters consisting of frequency factors ($k_{0,i}$) and activation energies ($E_{app,i}$). These parameters were determined using non-linear least-squares regression with 95% confidence intervals and very limited cross-correlation between parameters.
- d) It is anticipated that the proposed kinetic model could have significant value for the development of large scale downer reactor units for CLC.

CHAPTER 7 LARGE AND DEMONSTRATION SCALE SIMULATION

This chapter describes a Computational Particle Fluid Dynamics (CPFD) simulation using the BARRACUDA Virtual Reactor (VR) software. The goal is to establish a process model for a 100kW CLC power plant. The proposed CLC system includes two interconnected reactors: A riser-air reactor and a downer-fuel reactor, with a controlled oxygen carrier circulation between the two reactors. To analyze this riser-downer CLC configuration a multi-scale drag model (non-spherical Ganser's) was implemented in Barracuda and the CLC volume averaged kinetics was coupled with CPFD. The hybrid Barracuda VR-CPFD model used the Eulerian-Lagrangian approach called the MP-PIC (multi-phase particle-in-cell) and considered clustered particles as well [87].

Based on the CPFD data obtained, the following was accomplished: (a) The establishment of a riser-downer system for CLC performance assessment; (b) The calculation of the required oxygen carrier particle circulation; (c) The evaluation of the extent of CO₂ gas leaking via the loop-seal. In addition, the CPFD simulation enabled the optimization of both the air reactor and fuel reactor designs for high CLC performance.

7.1 Materials and Methods

7.1.1 CLC Riser and Downer System

A CLC process with a 100kW power generation capacity demonstration unit was considered. The CLC process involved the new HPOC of the present study together with a syngas having a 1.33 H₂/CO ratio.

Figure 7-1 reports a schematic diagram of the proposed CLC configuration for the large-scale CLC simulation of this present study. Syngas was supplied via a top downer injection port. Thus, the HPOC particles, flowing down from the top cyclone encountered the injected syngas, mixing homogeneously. This occurred before the HPOC particles moved further downwards. The downer height and diameter were carefully selected to ensure that the total gas and HPOC residence times were compatible with the high syngas conversions desired. Furthermore, the product-HPOC outlet system of this process was cautiously designed to ensure efficient particle separation with minimum particle entrainment. Furthermore, the fuel downer reactor was connected in the

proposed CLC process, with an air reactor via a loop seal. It is at this section where the HPOC was allowed to enter into the air reactor via an air pulsation system.

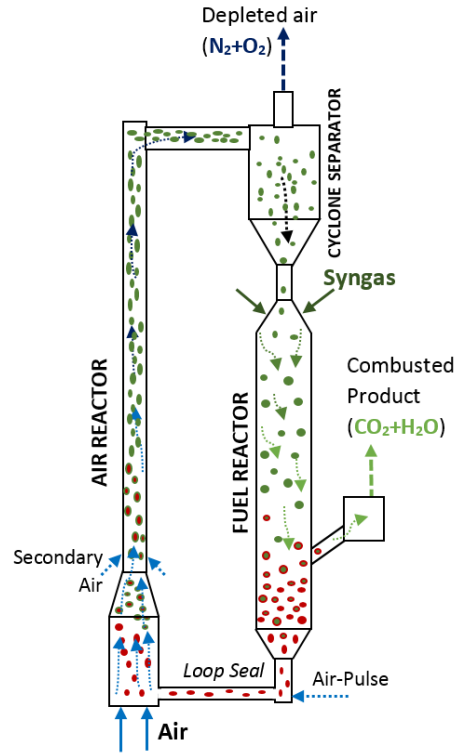


Figure 7-1: Schematic diagram of an Air Reactor (Riser) and Fuel Reactor (Downer) considered in the present study for CLC simulation

Regarding the air reactor, it was configured with the following parts: a) A fast-fluidized bed region at the unit bottom and b) A riser transport region in the middle and top section. The fast fluidized bed bottom section, secures a region with (e.g. 20%) particle volume fraction suitable for installing a heat exchanger [132]. This heat exchanger helps removing the heat generated by the exothermic syngas CLC reactions. A secondary air flow is supplied to transport particles properly to the cyclone gas-solid separator. As it travels through the air reactor, the HPOC gets fully oxidized when it comes into contact with air. The cyclone separates the gas flow from the reactivated HPOC particles to be returned to the downer unit.

7.1.2 Oxygen Carrier Particle

The particle size distribution (PSD) of HPOC was determined using Malvern Mastersizer 2000 size analyser as reported in Figure 7-2. The PSD result shows a mean particle diameter (d_{50} =87.1 μm) with a standard deviation 31.2 μm .

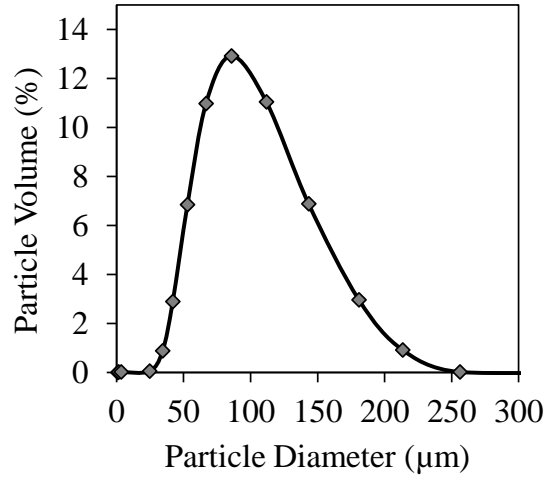


Figure 7-2: HPOC Particle Size Distribution

Table 7-1 reports the various relevant physical properties of the HPOC relevant for the CPFD simulations as follows: a) particle mean diameter, b) particle density, c) particle sphericity, d) particle close pack volume fraction, d) particle-wall tangential and normal retention coefficients, e) diffuse bound , f) maximum momentum redirection from particle to particle collision.

Table 7-1: Physical Properties of HPOC Particles

Parameters	Value
Particle mean diameter, d_{50} [μm]	87.1
Particle density, [kg/m^3]	1800
Particle sphericity	0.9
Particle close pack volume fraction	0.6
Particle-wall tangential retention coefficient	0.85
Particle-wall normal retention coefficient	0.85
Diffuse bounce	0
Maximum momentum redirection from particle to particle collision	40%

Furthermore, both in the riser or in the downer reactors, particle moves as cluster of particles rather than as single particles. Therefore, besides the single particle analysis, clustered particles are highly important to accurately represent hydrodynamics and gas-solid interactions in downers. Given the physical properties (i.e. particle diameter, density and sphericity) were essentially identical to the ones of a previous research study in CREC Laboratories [87], the HPOC cluster reported in Figure 7-3, was considered in the present study.

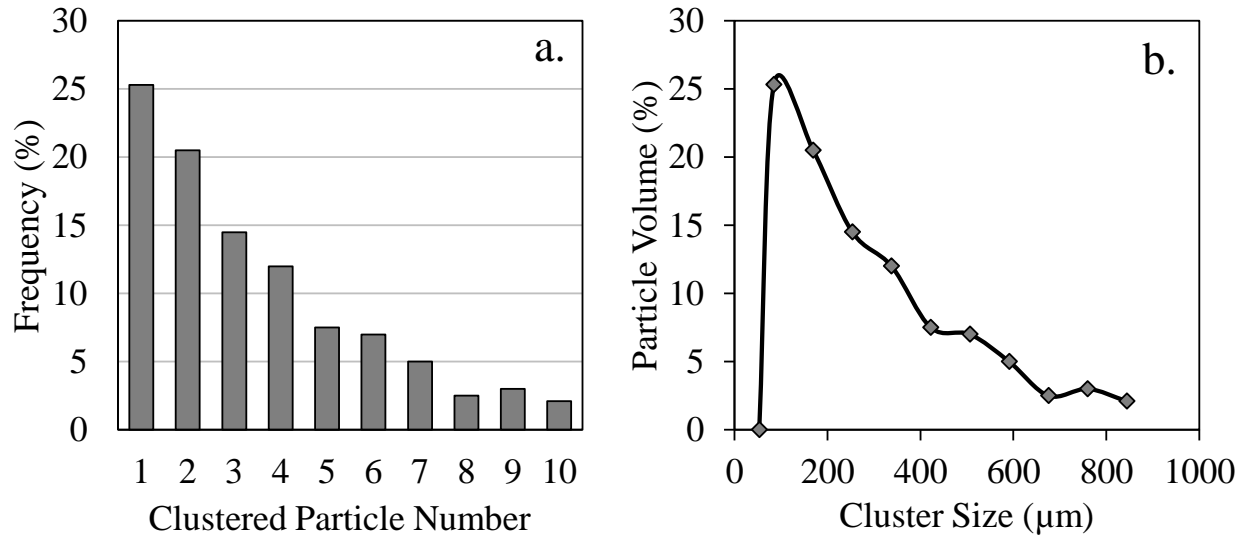


Figure 7-3: Clustered Particle Information: a) Distribution of number of particles in clusters for a gas velocity of 1.5 m/s and a particle mass flux 50 kg/m²/s [87] b) Expressed as cluster size distribution (cluster sphericity 0.64).

7.1.3 Particle and Fluid Dynamic Models

The CPFD methodology considers Reynolds Averaged Navier-Stokes equations to formulate fluid dynamics in the three dimensional space. The particle phase is described by the multi-phase-particle-in-cell (MP-PIC) method [84] to evaluate dense particle flows. Unlike the discrete particle (DPM) (Cundaland Strack, 1979), MP-PIC calculates particle stress gradient as a gradient on the grid instead of each particle.

The volume averaged mass continuity and momentum equations [133,134] are described as Eq.(7-1) and Eq.(7-2).

$$\frac{\partial(\varepsilon_g \rho_g)}{\partial t} + \nabla \cdot (\varepsilon_g \rho_g \mathbf{u}_g) = \delta \dot{m}_p \quad (7-1)$$

$$\frac{\partial(\varepsilon_g \rho_g \mathbf{u}_g)}{\partial t} + \nabla \cdot (\varepsilon_g \rho_g \mathbf{u}_g \mathbf{u}_g) = -\nabla p - \mathbf{F} + \varepsilon_g \rho_g \mathbf{g} + \nabla \cdot (\varepsilon_g \boldsymbol{\tau}_g) \quad (7-2)$$

where, ε_g is gas volume fraction, ρ_g is gas density, t is time, \mathbf{u}_g is gas velocity vector, $\delta \dot{m}_p$ is mass production rate in gas phase per unit volume due to particle-gas reaction, p is mean flow gas thermodynamic pressure, \mathbf{F} is gas to particle momentum transfer rate per unit volume, \mathbf{g} acceleration vector due to gravity, $\boldsymbol{\tau}_g$ is stress tensor in gas phase.

The properties of total gaseous phase are evaluated by the individual mass fraction ($Y_{g,i}$). Eq.(7-3) presents the transport equation of individual gas species.

$$\frac{\partial(\varepsilon_g \rho_g Y_{g,i})}{\partial t} + \nabla \cdot (\varepsilon_g \rho_g Y_{g,i} \mathbf{u}_g) = \nabla \cdot (\varepsilon_g \rho_g D \nabla Y_{g,i}) + \delta \dot{m}_{i,chem} \quad (7-3)$$

The turbulent mass diffusivity, $D = \mu / \rho_g Sc$, where μ is a shear viscosity as a sum of laminar and turbulent viscosity according to Smargorinsky model [135], Sc is turbulent Schmidt number.

The gas phase enthalpy balance equation can be written as Eq.(7-4) [136,137] where, h_g is enthalpy of gas, ϕ is viscous dissipation, \mathbf{q} is conductive heat flux of gas and \dot{Q} is energy source per volume. The conservative energy exchange from particle to gas phase is noted as S_h and the enthalpy diffusion term as \dot{q}_D .

$$\frac{\partial(\varepsilon_g \rho_g h_g)}{\partial t} + \nabla \cdot (\varepsilon_g \rho_g h_g \mathbf{u}_g) = \varepsilon_g \left(\frac{\partial p}{\partial t} + \mathbf{u}_g \cdot \nabla p \right) + \phi - \nabla \cdot (\varepsilon_g \mathbf{q}) + \dot{Q} + S_h + \dot{q}_D \quad (7-4)$$

The MP-PIC method considers a transport equation to describe particle phase dynamics via particle distribution function (PDF) [84]. Eq.(7-5) describes the function $f(\mathbf{x}_p, \mathbf{u}_p, m_p, t)$ as PDF where \mathbf{x}_p is the particle spatial location, \mathbf{u}_p is the particle velocity, m_p is the particle mass, \mathbf{A} is particle acceleration, D is drag function and τ_p is inter-particle normal stress.

$$\frac{\partial f}{\partial t} + \nabla_{\mathbf{x}_p} \cdot (f \mathbf{u}_p) + \nabla_{\mathbf{u}_p} \cdot (f \mathbf{A}) = \left(\frac{\partial f}{\partial t} \right)_{coll}^D \quad (7-5)$$

$$\mathbf{A} = \frac{d\mathbf{u}_p}{dt} = D(\mathbf{u}_g - \mathbf{u}_p) - \frac{1}{\rho_p} \nabla p - \frac{1}{\varepsilon_p \rho_p} \nabla \tau_p \quad (7-6)$$

The PDF is improved by O'Rourke et al. [138] adding a collision term on the right hand side of Eq.(7-5).

The drag model can be defined as Eq. (7-7) with C_d drag coefficient. This study considered Non Spherical Ganser's Model [139] which describes C_d depending on particle sphericity (ψ) by Eq. (7-8).

$$D = \frac{3}{8} C_d \frac{\rho_g |\mathbf{u}_g - \mathbf{u}_p|}{\rho_p r_p} \quad (7-7)$$

$$C_d = \theta_g^{n_0} K_2 \left[\frac{24}{Re K_1 K_2} (1 + c_0 (Re K_1 K_2)^{n_1}) + \frac{24 c_1}{1 + \frac{c_2}{Re K_1 K_2}} \right] \quad (7-8)$$

where, the constants are defined as $c_0=0.1118$; $c_1=0.01794$; $c_2=3305$; $n_0=-2.65$; $n_1=0.6567$; $n_2=1.8148$; $n_3=0.5743$, the isometric shape constants are defined as, $K_1 = 3(1 + 2\psi^{-0.5})^{-1}$ and $K_2 = 10^{n_2(-\log \psi)^{n_3}}$.

Further details of the governing equations for the gas and particles including the numerical procedures for solving the equations can be found elsewhere [136,137].

7.1.4 Reaction Kinetic Model Used

The choice of kinetic model has a prime importance in CLC for large-scale simulations. Hence, with that end, syngas CLC using HPOC were performed using a mini fluidized bed batch reactor, CREC Riser Simulator [41] as described in CHAPTER 5.

Table 7-2: Kinetic Parameters Applied in CLC Large Scale Simulation

Reaction	Reaction Rate ($\text{mol.m}^{-3}\text{s}^{-1}$)	$k_{0,i}^{app}$ ($\text{mol.m}^{-3}\text{psi}^{-1}\text{s}^{-1}$)	E_i^{app} (kJ/mol)
$\text{CH}_4 + \text{NiO} \xrightarrow{k_1} \text{CO} + 2\text{H}_2 + \text{Ni}$	$r_1 = k_1 P_{\text{CH}_4} (1 - \alpha)$	$k_{0,1} = 4.16 \times 10^{-2}$	$E_1 = 4.4 \times 10^{-7}$
$\text{CO} + \text{NiO} \xrightleftharpoons[k_4]{k_2} \text{CO}_2 + \text{Ni}$	$r_2 - r_4 = k_2 P_{\text{CO}} (1 - \alpha) - k_4 P_{\text{CO}_2} \alpha$	$k_{0,2} = 10.3 \times 10^{-2}$ $k_{0,4} = 1.86 \times 10^{-2}$	$E_2 = 3.89$ $E_4 = 9.85$
$\text{H}_2 + \text{NiO} \xrightleftharpoons[k_5]{k_3} \text{H}_2\text{O} + \text{Ni}$	$r_3 - r_5 = k_3 P_{\text{H}_2} (1 - \alpha) - k_5 P_{\text{H}_2\text{O}} \alpha$	$k_{0,3} = 33.2 \times 10^{-2}$ $k_{0,5} = 13.4 \times 10^{-2}$	$E_3 = 37.13$ $E_5 = 23.48$
$k_i(T) = k_{0,i}^{app} e^{\frac{-E_i^{app} \times 10^3}{R} \left(\frac{1}{T} - \frac{1}{T_c} \right)}; T_c = 823\text{K}$			

Regarding the syngas CLC runs, they were performed at different temperatures (500-650°C), times (2-40s) and two stoichiometric syngas to OC ratios ($\psi=1$ and $\psi=0.5$). The detailed performance and kinetic analysis is described in CHAPTER 6. Table 7-2 also reports the CLC kinetics and kinetic parameters for the CLC large-scale simulation. One should note that the reaction rates are expressed in Table 7-2 using volume-average kinetic parameters. Regarding CLC oxidation kinetics, a discrete model for nickel oxide formation from Ni was considered as reported by Dueso et al. [69] is used.

7.1.5 Geometry Consideration

A syngas CLC process is normally configured using an air reactor, a cyclone separator and a fuel reactor. Figure 7-4 reports the geometry for a large-scale CLC unit with its various dimensions. One should note that the air reactor bottom section was designed as a fast-fluidized bed. Using this approach, the HPOC particles were transported to the riser section with the anticipated high gas flow (0.01 kg/s inlet airflow). They entered into the cyclone via a cylindrical inlet designed for 15m/s cyclone inlet gas velocity.

Regarding the high efficiency cyclones, they were designed in the proposed CLC process configuration by following Stairmand's guidelines [140]. As well, one should note that the proposed downflow fuel reactor diameter was larger than the down-comer of the cyclone. Therefore, a reducer cone section was proposed to make this connection possible.

Furthermore, the Product Outlet was designed to avoid particle entrainment. This Product Outlet was followed by a loop-seal connected to the air reactor. During the process operation, a HPOC concentration near to the close packing was maintained in the Product Outlet section. This was done to avoid CO₂ leaking from the fuel reactor to the air reactor. Finally, a horizontal air pulsation flow was provided in the Loop Seal to feed the HPOC particles into the air reactor, having a steady HPOC circulation rate. Under the proposed conditions of the CLC system, a total HPOC particle inventory of 77 kg was used.

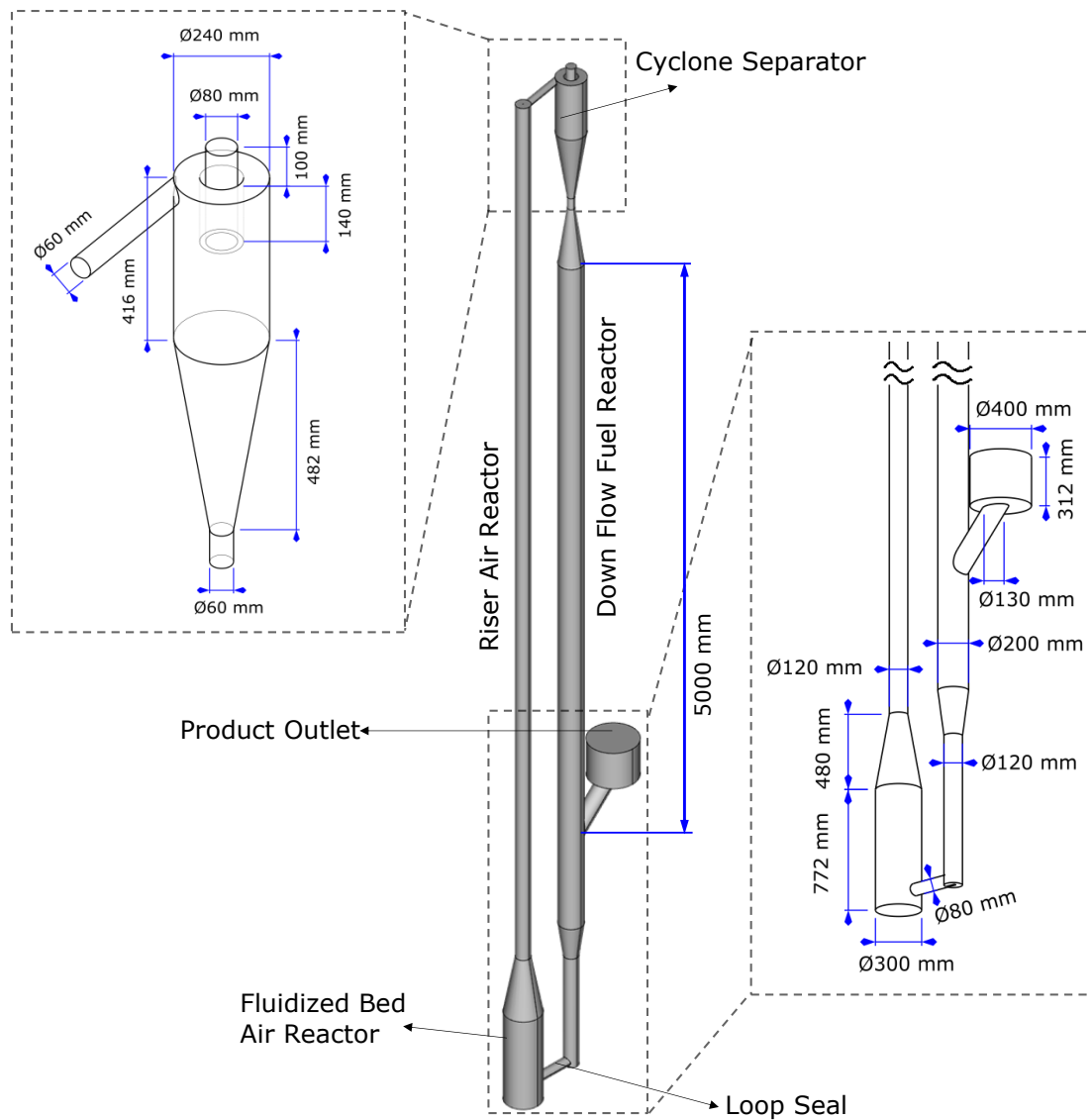


Figure 7-4: Geometrical Characteristics of the Proposed Syngas CLC System

7.1.6 Initial and Boundary Conditions

The objective of the present CPFD simulation for CLC simulation is to develop a model applicable under fully developed gas-solid flow. To achieve this, the CPFD simulations have to be started with satisfactory initial values begin the calculations. With this end, the following initial values were adopted: a) atmospheric pressure and 650°C in the entire unit. Gas density and viscosity were defined at these conditions, b) gas velocity at zero in the entire domain.

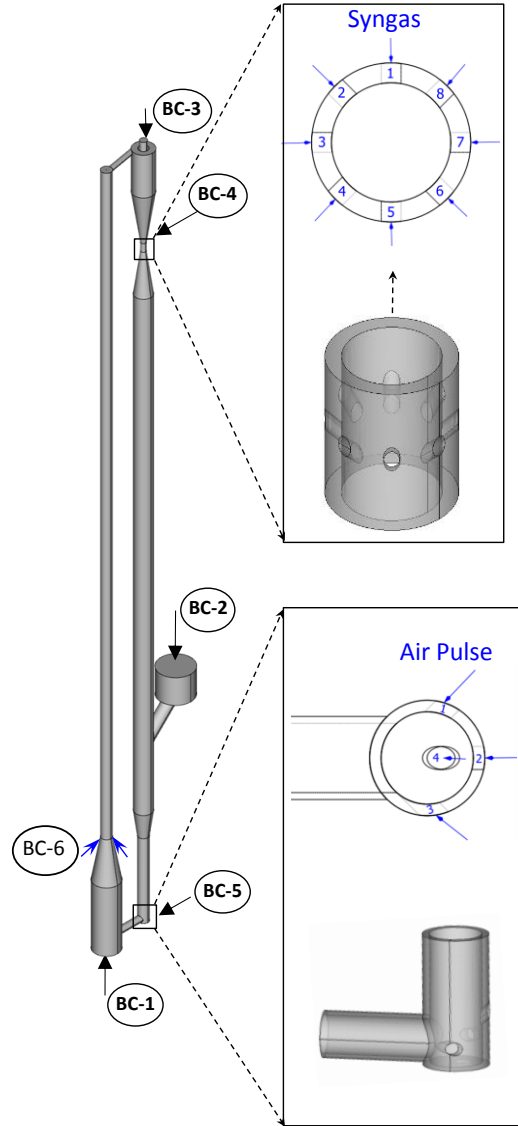


Figure 7-5: Schematic Diagram of a CLC Riser-Downer Configuration Indicating Boundary Conditions (BC)

Furthermore, Figure 7-5 reports the specific location of various boundary conditions used in the CPFD simulation as follows:

- a) An airflow rate (10 g/s) is provided to fluidize the HPOC at Boundary Condition 1 (BC-1).
- b) A secondary air flow is provided via four injection ports angled upwards at 45 degree to help with HPOC transport [141]. This is designated as Boundary Condition 6 (BC-6).
- c) Particles and gases are separated in a cyclone where pressure is kept at atmospheric conditions. This is designated as Boundary Condition 3.
- d) Eight (8) injection ports angled downwards 45 degrees downward provide syngas jets with a 10 m/s high velocity. This allows uniform HPOC distribution across the downflow fuel reactor. This is designated as Boundary Condition 4 (BC-4).
- e) The HPOC and product gas reach an outlet product separator at 1 atm. This is designated as Boundary Condition 2 (BC-2).
- f) The loop-seal near the output product separator promotes particle densification assumed at a 0.5 volume fraction. This is named as Boundary Condition 5 (BC-5).
- g) A steady HPOC circulation is achieved via an air pulsed air flow, preventing reverse gas flow towards the fuel reactor. Air pulsation frequency can be optimized, to achieve the required solid circulation and hydraulic pressure at the bottom of the air reactor.

7.1.7 Numerical Approach

In this study, a commercial software BARRACUDA VR® 17.3.0 module was used for computation particle fluid dynamics coupled with CLC reaction. A detailed description of the PC configuration employed in order to use the software is discussed in CHAPTER 4. The platform of this software is based on a finite volume method. A single simulation including chemistry takes at least 72 hours.

In this respect, time steps played a major role in the simulation output. In this simulation, time steps smaller than 0.002 seconds were used [87]. Furthermore, to obtain sufficient accuracy in the calculations, 364,580 numerical particles were considered.

Regarding the various calculations developed, they included: a) A simulation of the complete system including the riser and the downer as reported in Figure 7-4 ($7\text{m} \times 0.4\text{m} \times 1.4\text{m}$) with a

total of 100,000 cells in the computational mesh, Figure 7-6 reports a typical mesh used in this type of simulation, b) More detailed calculations in a downer unit with a 25m length and a 0.2 m diameter are given in Figure 7-12.

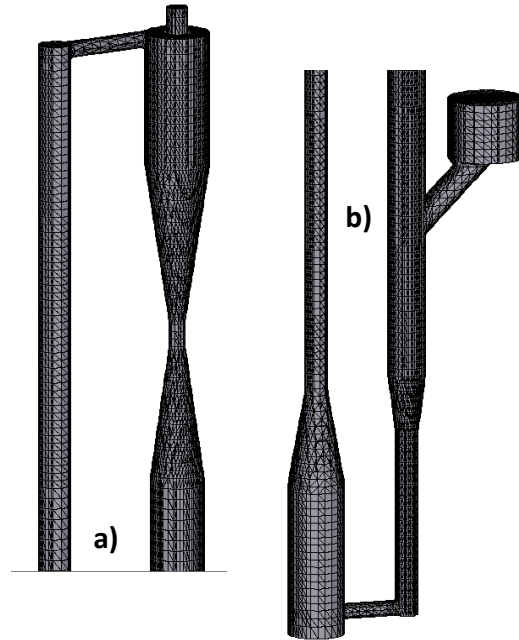


Figure 7-6: Typical Computational Mesh Pattern: a) Upper part of the CLC system b) Lower part of the CLC system

7.2 Simulation Results and Discussion

7.2.1 Solid Circulation and Loop Seal

Figure 7-7a illustrates the CPFD simulated particle volume fraction of the complete CLC system considered in this study. Figure 7-7b and Figure 7-7c report the HPOC mass flow and mass flux across the cut-planes (cross-section of reference) for both the Air Reactor-Riser and the Fuel Reactor-Downer.

Thus, and on this basis, as reported in Figure 7-7b, a stable solid circulation of 1.5 kg/s was established with a 1-3% HPOC volume fraction in the fuel reactor after 60s of simulation time. As well, a 500 kg/s/m² mass flux in the air reactor riser, and a 50 kg/s/m² mass flux in the fuel reactor were achieved. These values are in good agreement with typical experimental values and industrial requirements [142,143].

Controlling HPOC circulation is of critical importance in a CLC process. HPOC solid circulation depends on total system pressure, gas flow and solid holdup.

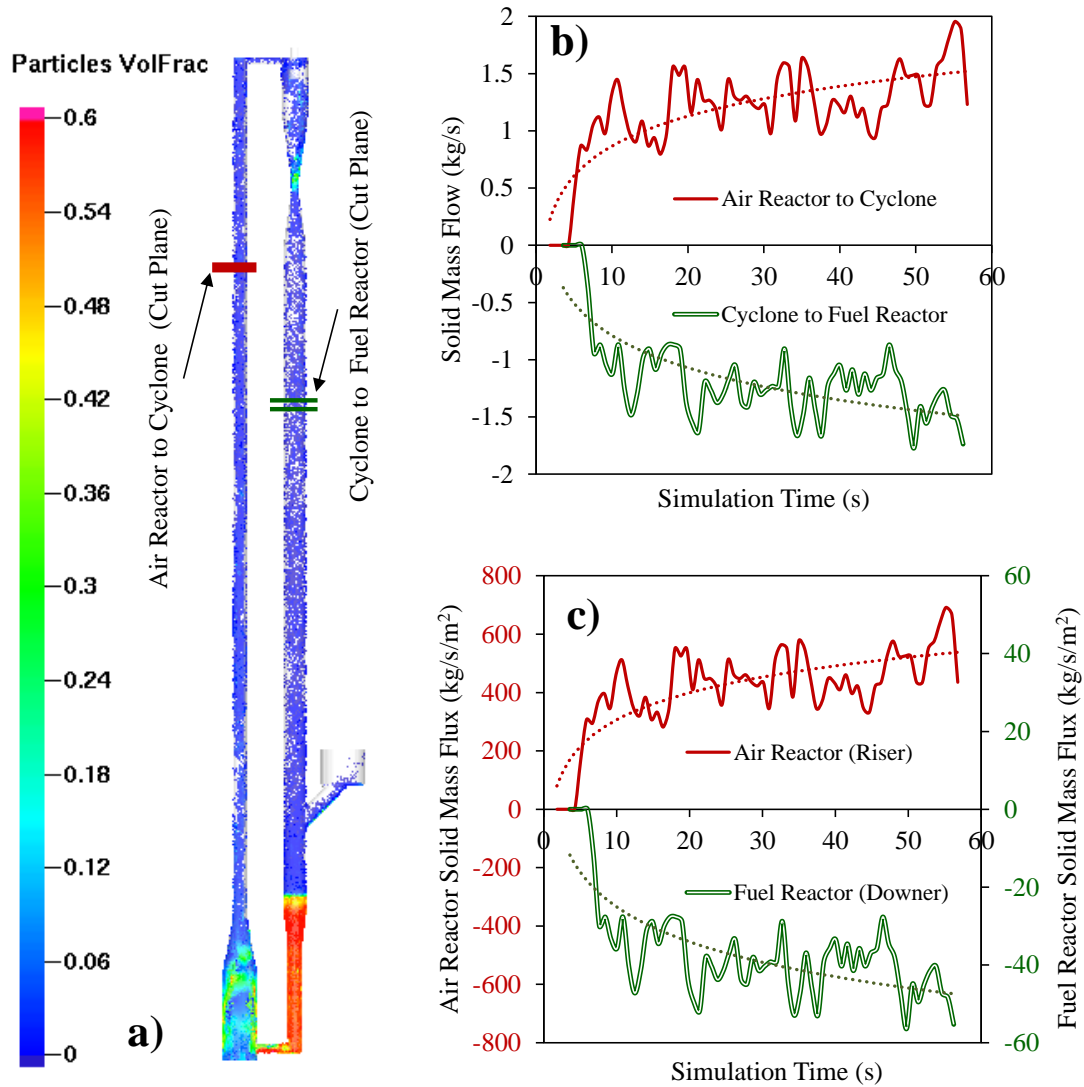


Figure 7-7: Simulated HPOC Circulation in the CLC: a) Particle volume fractions in various unit locations, b) HPOC flow rates at various simulation times, c) HPOC mass fluxes through the reactors at various simulation times. Notes: i) Data or solid circulation reported using a 1 second averaging , ii) Dotted line shows a logarithm variation of both mass flow and mass flux

The HPOC upflow transport requires a positive pressure at the air-riser reactor bottom section. This higher pressure creates a hindrance for HPOC particle circulation from the fuel-downer to the air-riser. To address this issue, a valve is required. There are several kinds of valves available as reported in the literature [144–146]. In this study, a non-mechanical valve (L-valve) was implemented as a loop-seal. With this L-Valve, a particle hold-up densification was kept in the bottom section of the air-reactor (≈ 0.5), creating both a loop-seal and preventing a backflow up from the air-reactor to the fuel reactor. [144]. With this end, a high pressure pulsation air injection was supplied at 5 g/s as follows: a) By first opening the L-Valve for 150 milliseconds, b) By keeping it closed later for 1.5 s. This valve operation was repeated during the entire run. Using this operational approach, one avoids the fluidization of the HPOC particles at the bottom of downer reactor and ensures that there is no gas leaking between the air-reactor and the fuel reactor.

7.2.2 Pressure Profiles

Figure 7-8 reports the average pressure level using a total of seven (7) simulated pressure probes. One can see that there is a steady pressure reduction in the air-riser unit (from P-5 to P-1). Furthermore, the cyclone operates with a pressure drop, and as a result a lower pressure at the cyclone exit (P-2). This is a requirement for effective gas-solid separation. Furthermore and along the downer, there is a very small additional pressure change (from P-2 to P-4). This is only the case at the downer bottom section where the loop-seal ensures that the pressure at P-5 increases. One should note that P-5 is slightly above the air reactor bottom section pressure as shown in P-6. ($P-5 > P-6$). Furthermore and in order to achieve steady HPOC solid circulation from the fuel reactor to the air reactor fluidized bed section pressurized pulsed is used. These trends are in agreement with the results obtained by Wang et al. [147]. Regarding pressure changes in the riser, one can notice an almost linear decrease with column height, with this pressure gradient being a function of the solid hold-up.

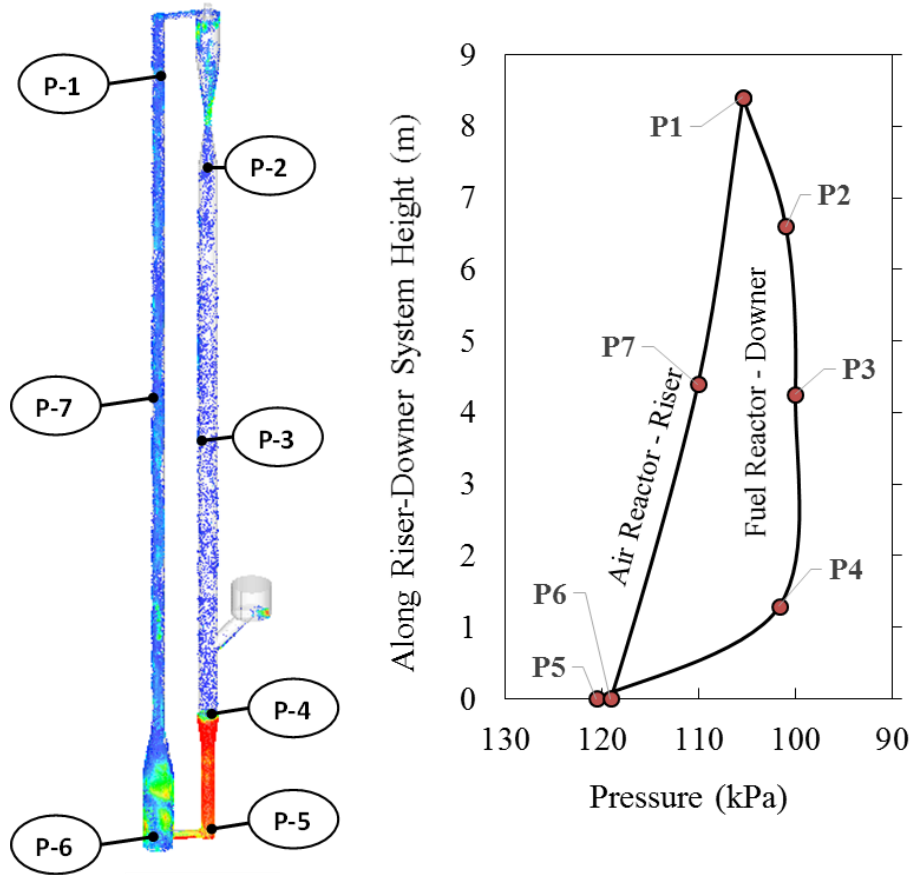


Figure 7-8: Pressure Levels at Different Locations of the CLC Process

7.2.3 Velocity Profiles and Volume Fraction

Figure 7-9 reports radial velocity profiles for both gas and particles. The data corresponds to an upper location (4m) and a lower location (2m) along the CLC downer. Reported data corresponds to radial line averages performed in the x-direction of a x-y Cartesian downer cross-section domain.

One can see that for CPFD simulation yields for a 0.85 m/s gas velocity and for a 3 m/s particle velocity, significant local variations of both gases and particle velocities are as follows a) ± 0.5 m/s for the gases, b) ± 1 m/s variation for the particles. One can also see that in spite of these significant local gas and particle velocity variations, change in phase, with this being an intrinsic fluid dynamic property in the downer. The results are in agreement with other research [148] reported in the literature.

On this basis, one can consistently predict slip velocities between gases and particles in the 2 m/s range. This is expected given at 0.85 m/s superficial gas velocity, due to particle densification, particle velocities surpass the 0.6 m/s estimated terminal settling velocity.

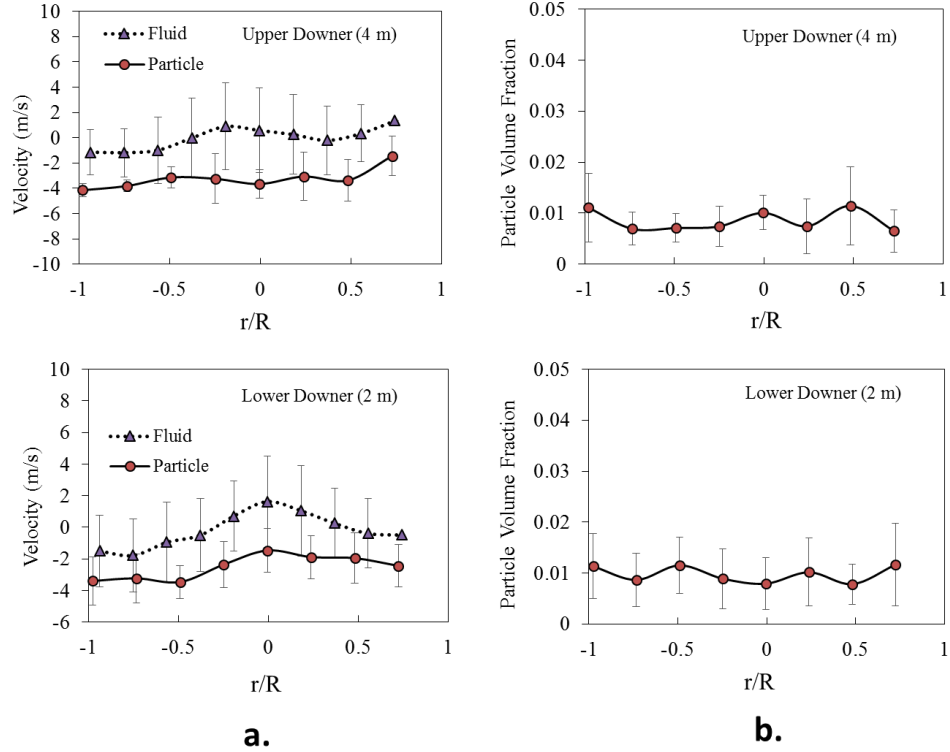


Figure 7-9: (a) Radial Gas and Particle Velocity Profiles and (b) Radial Particle Volume Fractions in the CLC Downer Unit using the “Single Particle” Model . Note: Observation times during downer operation were 1s, 2s, 3s.

Figure 7-10 reports the axial velocity of the HPOC particles (u_p) and the gas velocity (u_g) along the riser. One should note that each of the reported data points represents downer cross section averages at various downer heights. One could see that all reported cross-sectional average velocities are quite constant ($3 \text{ m/s} \pm 10\%$ for the particles and for $0.5 \text{ m/s} \pm 10\%$). This is the case in spite of the significant local velocity variations as reported in Figure 7-9.

Figure 7-10 also reports the average volume fraction along the downer. This property, as in the case of the cross-sectional average gas and particle velocity, appears to be a relatively constant one. The only exception to this trend is in the syngas feeding to the downer section, where an particle densification takes place. This is given the fluid redirection of particles coming from the

cyclone exit. However, once 1-2 m along the downer length is reached and a fully developed downer flow pattern is established, the particle volume fraction stabilizes as expected in a 1% particle volume fraction.

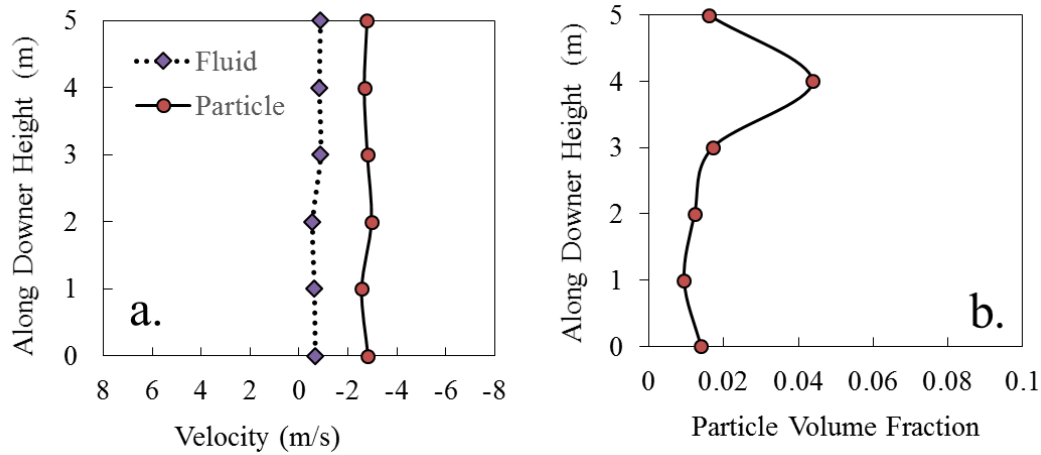


Figure 7-10: Axial Fluid and Particle Velocities along the Fuel CLC Downer Length: a) Particle and fluid velocity b) Particle volume fraction.

7.2.4 Simulated Reaction Analysis

In order to make it relevant to CLC, Barracuda VR simulations included CLC reactions coupled to the particle-fluid solver module. To accomplish this, heterogeneous reactions were considered by employing the Lagrangian Chemistry Model which calculates chemical reaction rates for each computational particle. To achieve this, CLC calculations were developed first by considering a 5m downer fuel reactor unit.

Figure 7-11 reports gas species mass flow rates at the CLC downer outlet. One can see that computations involved two steps: a) An initial 28 seconds simulation time with the reaction module turned “off” to obtain a steady downer operation, b) An additional 15 seconds of simulation time with the reaction module turned “on”. Once these two steps were completed, one could conclude that the calculated species flow rates represented the ones in a steady CLC downer unit. Regarding the observed mass flow rate oscillations, it is shown in the present study that they could be limited (Standard Deviations: 3%) by using simulation time steps smaller than 0.002s. An important fact to note is that the reported results show a theoretical 40% CO₂ yield which is in line

with the experimental value of a 43% CO₂ yield in the CREC Riser Simulator after 5 seconds of reaction time. For additional details, refer to CHAPTER 5.

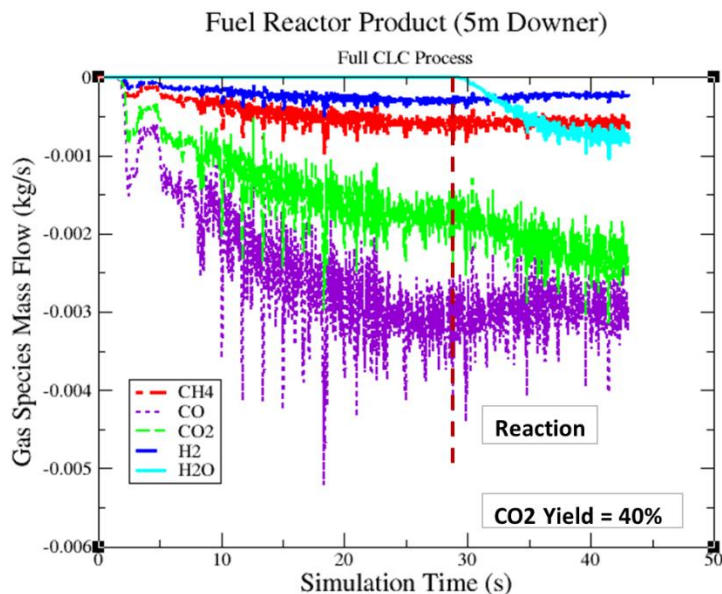


Figure 7-11: Simulated Total Gas Species Mass Flow in a Complete CLC Process using a 5 m downer. Note: a) The negative sign indicates a mass flow rate defined in downward direction, b) The CLC reaction module was activated after 28 second, c) Simulation time steps are: 0.002s

Furthermore, to develop more relevant CLC simulations, and to reach a 90% CO₂ yield, a 25m downer was considered suitable. In this case, both single and clustered particle models were included in the simulations. The solid downer entry flow rate was kept at 1.5 kg/s and the syngas fed was kept at 6 g/s. One significant change in the CFPD simulations at this point, was to turn “on” the CLC reaction module from the very beginning. This was required given that it was found that the initial period with the CLC reaction turned “off”, while was good for studying the downer flow without reaction and the added effect of CLC, was not strictly required for CLC with the same numerical solution being obtained.

Figure 7-12 reports the syngas conversion performance in the downer using the “single particle” model. Reported results compare the 5m downer and the 20m downer with 45% CO₂ yields, and 80% CO₂ yields, respectively. One should note that these results were obtained after 30s of simulation time.

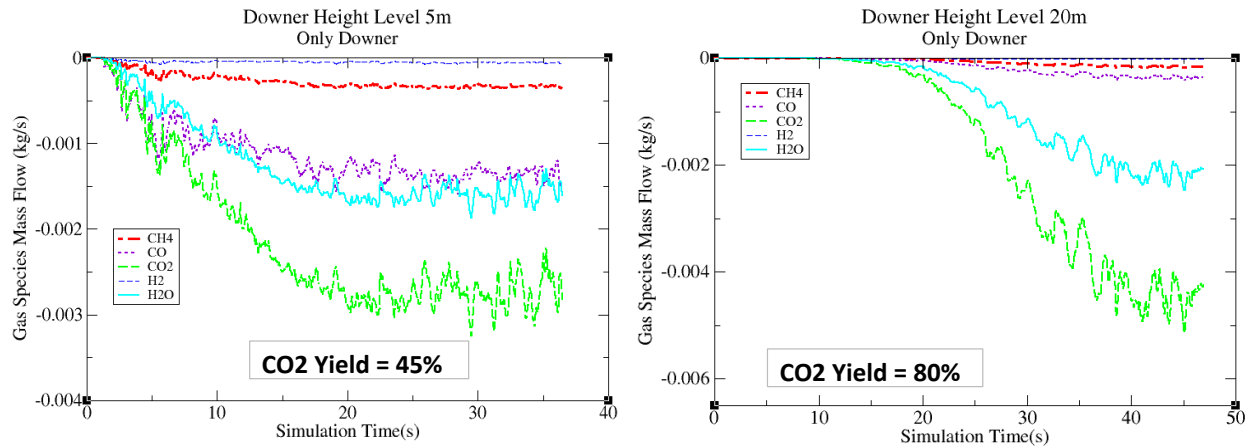


Figure 7-12: Simulated total gas species mass flow rates at different downer height levels of 5m and 20m. Notes: a) downer height is defined in the downward direction and from the top of the unit, b) the negative sign is assigned to mass flow shows in the downward direction

Furthermore and to provide realistic CPFD simulations of the CLC downer-fuel reactor, a unit performance analysis was also developed using the “particle cluster” model. This model considers a particle cluster size distribution as described in Section 7.1.2. This HPOC particle cluster distribution is expected to be result of a dynamic balance between cluster formation and cluster breakup [149].

Figure 7-13 reports the syngas combustion in the downer unit using the “particle cluster” model. In this case, the CLC reaction module in the CPFD Barracuda downer simulation was turned “on” from the very beginning of the calculation. One can see in Figure 7-13, that after 30s of simulation time, a 38% CO₂ yield was obtained at 5m from downer top and a 70% CO₂ yield was obtained at the end of the 20m downer reactor. Thus, it was observed that the additional flow details provided in the downer fluid dynamics using particle clusters, reduces about 15% the CO₂ yield. As a consequence, the particle is an important factor to be considered in CPFD simulations of both demonstration and large scale CLC downer units.

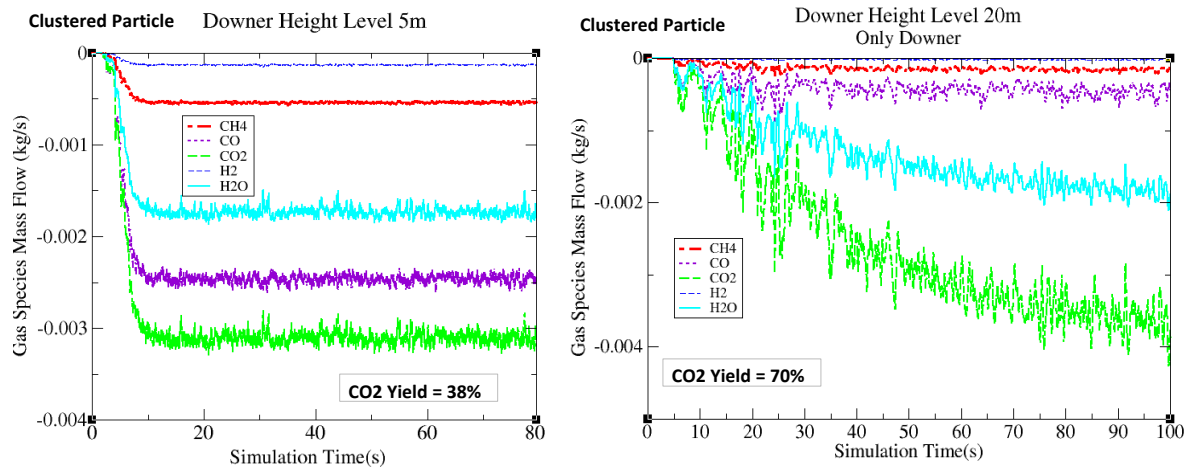


Figure 7-13: Total simulated gas species mass flow rates at different downer height levels using particle clusters with only downer system. Note: The negative sign indicates mass flows in a downward direction.

Figure 7-14 predicts that, the CLC performance with 90% CO₂ yield is achievable using HPOC by applying 25m downer reactor for the case of “single particle”. The provided solid flux was 50 kg/s/m² which also applied for clustered particle. For the case of particle cluster, it requires 30m downer reactor to achieve same 90% CO₂ yield. Also this represents the worst case scenario for syngas conversion as the cluster size does not reduce all through the downer essentially no increase of surface area for reaction.

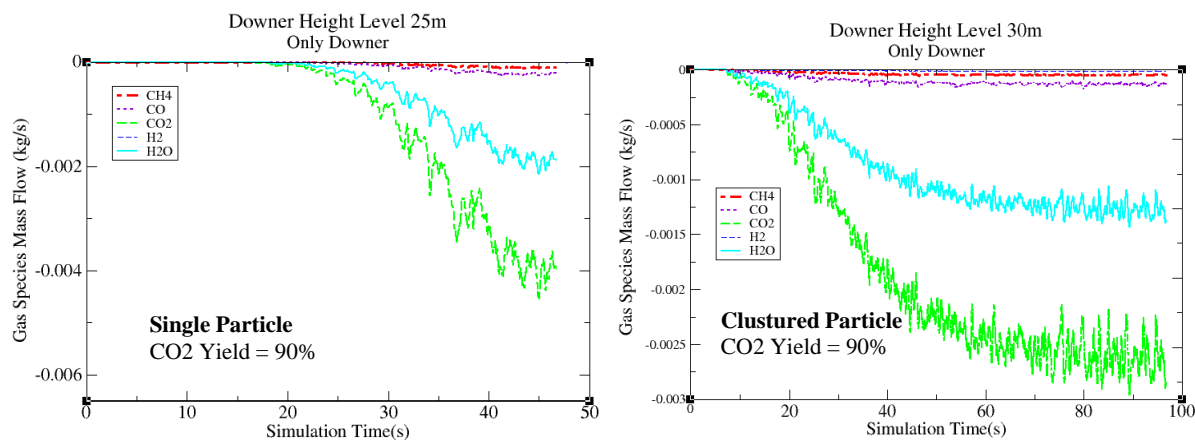


Figure 7-14: Total simulated gas species mass flow rates and predicted only downer height levels for single and clustered particles to achieve 90% CO₂ yield. Note: The negative sign indicates mass flows in a downward direction.

7.3 Conclusions

- a) A demonstration scale chemical looping combustion process was successfully simulated using both CPFD and CLC kinetics. This allowed designing and optimizing the CLC process for HPOC applications.
- b) The CLC system was established using a riser-air reactor and a downer-fuel reactor in a twin fluidized bed configuration. The use of a hybrid CPFD computational model was important to account for particle cluster formation.
- c) A desired solid circulation was achieved using an air pulsation system in the loop-seal section. The selected air pulsation frequency involved opening the L-Valve for 150 milliseconds and keeping it closed later for 1.5s.
- d) An applicable HPOC kinetic model was incorporated into the CPFD simulation, by considering a CLC unit using both “single particle” and “clustered particle” models. It was predicted that a 90% CO₂ yield can be obtained in a 25m downer reactor using “single particle” model and 30m downer reactor using “clustered particle” model with a solid flux of 50 kg/s/m².

CHAPTER 8 CONCLUSIONS AND RECOMMENDATIONS

8.1 Conclusions

- a) The high performance of a nickel γ -alumina oxygen carrier (HPOC) was successfully demonstrated in the present study. With this end, CLC systematic runs were developed in a CREC Riser Simulator.
- b) The CREC Riser Simulator was evaluated prior to the CLC runs by employing CFD simulations. This allowed confirming that there was high gas mixing and good particle fluidization in this unit.
- c) A thermodynamic analysis was implemented in the present study, showing a consistent 99% syngas equilibrium conversion below 800°C. The thermodynamic model also predicted full methane conversion and OCs free of carbon, above 300°C and 150°C, respectively.
- d) The HPOC showed an excellent CLC when using syngas (i.e. $H_2/CO=2.5$ and $H_2/CO=1.33$) at 650°C with a $\psi=0.5$ fuel/OC stoichiometric ratio. Furthermore, in this case, a 92% CO_2 yield and 90% CO, 95% H_2 and 91% CH_4 conversions were obtained.
- e) The HPOC displayed an encouraging 40% OC oxygen conversion at 650°C and 40s. This very valuable accomplishment given the 50% expected maximum OC conversion, displayed Coke was formed under these conditions in minute amounts ($< 0.07\text{wt } \%$).
- f) The selected thermal level in the 550-650°C range had little influence on the HPOC performance. These findings point towards a CLC reaction dominated by oxygen lattice diffusion.
- g) A phenomenological kinetics based on solid-state reactions (Avrami-Erofeev NNGM) was proven suitable to describe syngas CLC using the HPOC.
- h) The resulting kinetics involved ten kinetic parameters (5 frequency factors and 5 activation energies). These parameters were successfully determined using non-linear least-squares data regression with 95% confidence intervals and limited cross-correlation between parameters.
- i) It was observed that according to the frequency factors obtained, the reactivity of the species using the HPOC could be expressed the following reactivity order: $H_2 > CO > CH_4$.

- j) It was demonstrated that the developed kinetic model could be applied to establish a computational particle fluid dynamics (CPFD) simulation in a 100kW CLC facility. This simulation uses a hybrid CPFD model featuring “single particles” and “clustered particles”.
- k) The CFD model shows that for particle clusters, 500 kg/s/m² solid fluxes in the riser air reactor and 50 kg/s/m² solid fluxes in the downer fuel reactor, can be obtained. Together with this, a 1% particle volume fraction with a 3m/s gas cluster particle slip velocity were obtained.
- l) The CFD results demonstrated that 90% CO₂ yields can be achieved in a 25m length downer unit using a “single particle” model versus the 30m downer unit required for the “clustered particle” model. As well, it was proven that a L-type loop seal between the downer and riser yields negligible CO₂ leakage.

8.2 Recommendations

- a) It would be of interest to establish the effect of the feeder design on the performance of the downer unit and this to prevent fluid and OC non-uniform cross-section distributions.
- b) It would be valuable to consider vertical or horizontal tube heat exchangers inside the air-fluidized bed. This would allow assessment of heat removal in the air reactor and evaluation of the effect of heat exchangers on the circulation of OC in the entire CLC process.

NOMENCLATURE

c	sound velocity at medium (m/s)
$C_{b,i}$	concentration in bulk phase(mol/m ³)
C_{μ}, C_{e1}, C_{e2}	turbulence model coefficients
C_i	mass concentration of “i” species
$C_{s,i}$	concentration at external surface of particles (mol/m ³)
C_{WP}	dimensionless number
d_p	mean oxygen carrier particle diameter (m)
d_v	average crystal diameter (m)
$\%D$	metal Dispersion
D_{iA}	diffusion coefficient in medium
E_i^{app}	apparent activation energy (kJ/mole)
f_I	conversion factor=101325/RT/14.7 where, R(J.mol ⁻¹ K ⁻¹), T(K)
$f(\alpha)$	function to describe lattice oxygen depletion at solid state
f_{obj}	objective function
F	volume force (N)
ΔH^o	heat of reaction (kJ/mole)
ΔH_c^o	heat of combustion (kJ/mole)
k	kinetic energy of turbulence (J/Kg)
k_v	von Karman’s constant
$k_{0,i}^{app}$	pre-exponential or frequency factor (mol.m ⁻³ psi ⁻¹ s ⁻¹)
$k(T)$	reaction rate constant as a function of temperature
k_g	mass transfer coefficient
k,m,n	stoichiometric coefficient
K_1, K_2	isometric shape constant
K_c, K_p	Equilibrium constant
M	Mach number
m_p	Particle mass (kg)
n	Avrami’s equation exponent
n_i	moles of i in the gaseous product/feed
p	kinetic parameters
P_i	partial pressure of species “i” (psi)
P_k	production of turbulent kinetic energy due to the mean flow gradients (J/m ³ /s)

$P_{i,exp}$	experimentally observed partial pressure of species “i” (psi)
$P_{i,th}$	model predicted partial pressure of species “i” (psi)
$(-r_n)$	rate of n th reaction (mol.m ⁻³ s ⁻¹)
$(-r_i)$	reaction rate of species “i” (mol.m ⁻³ s ⁻¹)
$(-r_{exp})$	experimental rate of reaction
R	universal gas constant
Re	Reynolds Number
Sc	Schmidt number
Sh	Sherwood number
S_{ex}	external surface area (m ² /g)
S_m	average surface area (nm ²) exposed per surface metal atom
Syngas-250	syngas with a H ₂ /CO molar ratio of 2.5
Syngas-133	syngas with a H ₂ /CO molar ratio of 1.33
T	operating temperature (K)
T_c	centering temperature to reduce cross-correlation factor (K)
t	reaction time (s)
t^*	frozen time(s)
u	fluid or particle velocity (m/s)
$u_{b,face}$	fluid velocity at either the “right face” or “left face” of the baffle (m/s)
$u_{i,face}$	Fluid velocity at either the “right face” or “left face” of the impeller blade (m/s),
u_{imp}	velocity of impeller blade wall (m/s)
u_{rel}	relative fluid velocity with the wall (m/s)
$u_{rel,tang}$	relative tangential fluid velocity with the wall (m/s)
u_τ	shear velocity or friction velocity(m/s)
V_g	molar volume gas at STP (i.e. 22414 cm ³ /mole)
V_m	volume of metal atoms (nm ³)
V_T	total reactor volume (cm ³)
W	Weight of the catalyst (g)
x	Displacement vector of impeller surface (m)

Symbols

α	oxygen carrier oxygen conversion
$\alpha_{i,exp}$	experimentally observed solid-phase oxygen conversion
$\alpha_{i,th}$	model predicted observed solid-phase oxygen conversion

δ_w^+	Wall lift-off also known as dimensionless wall unit (y^+).
ϕ	particle shape constant
ψ	fuel stoichiometric oxygen to supplied oxygen ratio
ϵ	Dissipation rate of turbulent kinetic energy(J/(Kg/s)
μ	Viscosity(Pa.s)
μ_T	Turbulent viscosity(Pa.s)
ν	Kinematic viscosity(m ² /s) or chemisorption stoichiometric factor
ρ	Fluid of particle density (kg/m ³)
ρ_{OC}	apparent density of oxygen carrier particle
σ_k, σ_e	Turbulence model coefficients
τ_g	stress tensor in gas phase (Pa)
τ_w	Shear stress(Pa)

Abbreviation

4PV/6PV	Four Port Valve/ Six Port Valve
BET	Brunauer–Emmett–Teller
BJH	Barrett-Joyner-Halenda
CCS	Carbon Capture and Storage
CFD	Computational Fluid Dynamics
CLC	Chemical Looping Combustion
CPFD	Computational Particle Fluid Dynamics
CREC	Chemical Reaction Engineering Centre
DOF	Degree of Freedom
FCC	Fluid Catalytic Cracking
FEM	Finite Element Method
FID	Flame Ionization Detector
GC	Gas Chromatograph
GMRES	Generalized Minimal Residual
HPOC	Highly Performing Oxygen Carrier
HRN	High Reynolds Number
IUPAC	International Union of Pure and Applied Chemistry
JCPDS	Joint Committee on Powder Diffraction Standards
LRN	Low Reynolds Number
MFC	Mass Flow Controller

MTN	Methanizer
NNGM	Nucleation and Nuclei Growth Model
OC	Oxygen Carrier
OC-Ref	Reference OC prepared by similar method of previous researcher
PSD	Pore Size Distribution
RAM	Random Access Memory
RANS	Reynolds Average Navier-Stokes equation
RPM	Rotation Per Minute
STP	Standard Temperature and Pressure (273.13K and 760 mmHg)
SCM	Shrinking Core Model
TCD	Thermal Conductivity Detector
TPD	Temperature Programmed Desorption
TPO	Temperature Programmed Oxidation
TPR	Temperature Programmed Reduction
VR	Virtual Reactor (Barracuda)
XRD	X-ray Diffraction

REFERENCES

- [1] S.O. Omoruyi, D.J. Idiata, The Environmental and Cost Implication of Fossil Fuel Generators : New Benin Market , Benin City , Nigeria, IJETAE. 5 (2015) 25–29.
- [2] R. Carapellucci, A. Milazzo, Membrane systems for CO₂ capture and their integration with gas turbine plants, Proc. Inst. Mech. Eng. Part A J. Power Energy. 217 (2003) 505–517.
- [3] H. Yang, Z. Xu, M. Fan, R. Gupta, R.B. Slimane, A.E. Bland, I. Wright, Progress in carbon dioxide separation and capture: A review, J. Environ. Sci. 20 (2008) 14–27.
- [4] L.M. Romeo, I. Bolea, J.M. Escosa, Integration of power plant and amine scrubbing to reduce CO₂ capture costs, Appl. Therm. Eng. 28 (2008) 1039–1046.
- [5] M.M. Hossain, H.I. de Lasa, Chemical-looping combustion (CLC) for inherent CO₂ Separation- a review, Chem. Eng. Sci. 63 (2008) 4433–4451.
- [6] J. Adanez, A. Abad, F. Garcia-labiano, P. Gayan, L.F. de Diego, Progress in Chemical-Looping Combustion and Reforming technologies, Prog. Energy Combust. Sci. 38 (2012) 215–282.
- [7] M.R. Quddus, a Novel Mixed Metallic Oxygen Carrier for Chemical Looping Combustion : Preparation , Characterization & Kinetic Modeling, (2013).
- [8] W.K. Lewis, E.R. Gilliland, W.A. Reed, Reaction of Methane with Copper Oxide in a Fluidized Bed, Ind. Eng. Chem. 41 (1949) 1227–1237.
- [9] H.J. Richter, K.F. Knoche, Reversibility of Combustion Processes, in: ACS Symp. Ser. Am. Chem. Soc. Washington, DC, 1983, 1983: pp. 71–85.
- [10] M. Ishida, D. Zheng, T. Akehata, Evaluation of a chemical-looping-combustion power-generation system by graphic exergy analysis, Energy. 12 (1987) 147–154.
- [11] N.R. McGlashan, Chemical-looping combustion – a thermodynamic study, Proc. Inst. Mech. Eng. Part C J. Mech. Eng. Sci. 222 (2008) 1005–1019.
- [12] M. Ishida, H. Jin, A Novel Chemical-Looping Combustor without NO_x Formation, Ind. Eng. Chem. Res. 35 (1996) 2469–2472.
- [13] M. Ishida, Hongguang Jin, A novel combustor based on chemical-looping reactions and its reaction kinetics, J. Chem. Eng. Japan. 27 (1994) 296–301.
- [14] M.R. Quddus, M.M. Hossain, H.I. de Lasa, Ni based oxygen carrier over γ -Al₂O₃ for chemical looping combustion: Effect of preparation method on metal support interaction,

- Catal. Today. 210 (2013) 124–134.
- [15] K.E. Sedor, M.M. Hossain, H.I. de Lasa, Reactivity and stability of Ni/Al₂O₃ oxygen carrier for chemical-looping combustion (CLC), Chem. Eng. Sci. 63 (2008) 2994–3007.
 - [16] C. Dueso, A. Abad, F. García-Labiano, L.F. de Diego, P. Gayán, J. Adánez, A. Lyngfelt, Reactivity of a NiO/Al₂O₃ oxygen carrier prepared by impregnation for chemical-looping combustion, Fuel. (2010).
 - [17] T. Mattisson, A. Lyngfelt, Capture of CO₂ using chemical-looping combustion, in: Proc. First Bienn. Meet. Scand. Sect. Combust. Inst., 2001: pp. 163–168.
 - [18] P.H. Bolt, F.H.P.M. Habraken, J.W. Geus, Formation of Nickel, Cobalt, Copper, and Iron Aluminates from α - and γ -Alumina-Supported Oxides: A Comparative Study, J. Solid State Chem. 135 (1998) 59–69.
 - [19] Q. Zafar, T. Mattisson, B. Gevert, Redox investigation of some oxides of transition-state metals Ni, Cu, Fe, and supported on SiO₂ and MgAl₂O₄, Energy and Fuels. 20 (2006) 34–44.
 - [20] H. Jin, M. Ishida, A new type of coal gas fueled chemical-looping combustion, Fuel. 83 (2004) 2411–2417.
 - [21] H. Jin, T. Okamoto, M. Ishida, Development of a Novel Chemical-Looping Combustion: Synthesis of a Looping Material with a Double Metal Oxide of CoO–NiO, Energy & Fuels. 12 (1998) 1272–1277.
 - [22] T. Mattisson, A. Järnäs, A. Lyngfelt, Reactivity of some metal oxides supported on alumina with alternating methane and oxygen - Application for chemical-looping combustion, Energy and Fuels. 17 (2003) 643–651.
 - [23] P. Cho, T. Mattisson, A. Lyngfelt, Comparison of iron-, nickel-, copper- and manganese-based oxygen carriers for chemical-looping combustion, Fuel. 83 (2004) 1215–1225.
 - [24] M. Ishida, M. Yamamoto, T. Ohba, Experimental results of chemical-looping combustion with NiO/NiAl₂O₄ particle circulation at 1200 °C, in: Energy Convers. Manag., 2002: pp. 1469–1478.
 - [25] C. Dueso, F. García-Labiano, J. Adánez, L.F. de Diego, P. Gayán, A. Abad, Syngas combustion in a chemical-looping combustion system using an impregnated Ni-based oxygen carrier, Fuel. 88 (2009) 2357–2364.
 - [26] P. Erri, A. Varma, Spinel-Supported Oxygen Carriers for Inherent CO₂ Separation during

- Power Generation., Ind. Eng. Chem. Res. 46 (2007) 8597–8601.
- [27] M.M. Hossain, H.I. de Lasa, Reactivity and stability of Co-Ni/Al₂O₃ oxygen carrier in multicycle CLC, AIChE J. 53 (2007) 1817–1829.
 - [28] L. Shen, Z. Gao, J. Wu, J. Xiao, Sulfur behavior in chemical looping combustion with NiO/Al₂O₃ oxygen carrier, Combust. Flame. 157 (2010) 853–863.
 - [29] L. Shen, J. Wu, Z. Gao, J. Xiao, Characterization of chemical looping combustion of coal in a 1 kWth reactor with a nickel-based oxygen carrier, Combust. Flame. (2010).
 - [30] L. Shen, J. Wu, Z. Gao, J. Xiao, Reactivity deterioration of NiO/Al₂O₃ oxygen carrier for chemical looping combustion of coal in a 10 kWth reactor, Combust. Flame. (2009).
 - [31] K.E. Sedor, M.M. Hossain, H.I. de Lasa, Reduction kinetics of a fluidizable nickel-alumina oxygen carrier for chemical-looping combustion, Can. J. Chem. Eng. 86 (2008) 323–334.
 - [32] M.M.M. Hossain, K.E.E. Sedor, H.I.I. de Lasa, Co-Ni/Al₂O₃ oxygen carrier for fluidized bed chemical-looping combustion: Desorption kinetics and metal-support interaction, Chem. Eng. Sci. 62 (2007) 5464–5472.
 - [33] F. García-Labiano, L.F. De Diego, P. Gayán, J. Adánez, A. Abad, C. Dueso, Effect of fuel gas composition in chemical-looping combustion with ni-based oxygen carriers. 1. fate of sulfur, Ind. Eng. Chem. Res. (2009).
 - [34] J. Adánez, F. García-Labiano, P. Gayán, L.F. de Diego, A. Abad, C. Dueso, C.R. Forero, Effect of gas impurities on the behavior of Ni-based oxygen carriers on chemical-looping combustion, in: Energy Procedia, 2009.
 - [35] P. Gayán, C. Dueso, A. Abad, J. Adanez, L.F. de Diego, F. García-Labiano, NiO/Al₂O₃ oxygen carriers for chemical-looping combustion prepared by impregnation and deposition-precipitation methods, Fuel. (2009).
 - [36] M.M. Hossain, K.E. Sedor, H.I. de Lasa, Co-Ni/Al₂O₃ oxygen carrier for fluidized bed chemical-looping combustion: Desorption kinetics and metal-support interaction, Chem. Eng. Sci. 62 (2007) 5464–5472.
 - [37] M.M. Hossain, D. Lopez, J. Herrera, H.I. de Lasa, Nickel on lanthanum-modified γ -Al₂O₃ oxygen carrier for CLC: Reactivity and stability, Catal. Today. (2009).
 - [38] P. Erri, A. Varma, Diffusional Effects in Nickel Oxide Reduction Kinetics, Ind. Eng. Chem. Res. 48 (2009) 4–6.

- [39] H. Jin, T. Okamoto, M. Ishida, Development of a novel chemical-looping combustion: Synthesis of a looping material with a double metal oxide of CoO-NiO, *Energy and Fuels*. (1998).
- [40] M. Ishida, H. Jin, Fundamental Study on a Novel Gas Turbine Cycle, *J. Energy Resour. Technol.* (2001).
- [41] H.I. de Lasa, Riser Simulator, U.S. Patent, 5,102,628, 1992.
- [42] D. Kraemer, H. de Lasa, Catalytic cracking of hydrocarbons in a riser simulator, *Ind. Eng. Chem. Res.* 27 (1988) 2002–2008.
- [43] S. Rostom, H.I. de Lasa, Propane Oxidative Dehydrogenation Using Consecutive Feed Injections and Fluidizable VO_x/γAl₂O₃ and VO_x/ZrO₂-γAl₂O₃ Catalysts, *Ind. Eng. Chem. Res.* (2017) acs.iecr.7b01369.
- [44] Y. Aponte, H. de Lasa, A Zn-Offretite for the adsorption of thiophenic species under fluidized catalytic cracking conditions. Synthesis, characterization and reactivity, *Appl. Catal. B Environ.* 189 (2016) 160–171.
- [45] A.A. Ayandiran, I.A. Bakare, H. Binous, S. Al-Ghamdi, S.A. Razzak, M.M. Hossain, Oxidative dehydrogenation of propane to propylene over VO_x/CaO-γ-Al₂O₃ using lattice oxygen, *Catal. Sci. Technol.* (2016).
- [46] J. Mazumder, H.I. de Lasa, Catalytic steam gasification of biomass surrogates: Thermodynamics and effect of operating conditions, *Chem. Eng. J.* 293 (2016) 232–242.
- [47] R. Pujro, M. Falco, U. Sedran, Production of aromatic compounds in the heavy naphtha and light cycle oil ranges: catalytic cracking of aromatics and C₁₀ naphthenic-aromatics, *J. Chem. Technol. Biotechnol.* 91 (2016) 336–345.
- [48] I.A. Bakare, S.A. Mohamed, S. Al-Ghamdi, S.A. Razzak, M.M. Hossain, H.I. de Lasa, Fluidized bed ODH of ethane to ethylene over VO_x-MoO_x/γ-Al₂O₃ catalyst: Desorption kinetics and catalytic activity, *Chem. Eng. J.* 278 (2015) 207–216.
- [49] S.A. Mohamed, M.R. Quddus, S.A. Razzak, M.M. Hossain, H.I. de Lasa, Fluidizable NiO/Ce-γAl₂O₃ Oxygen Carrier for Chemical Looping Combustion, *Energy & Fuels*. 29 (2015) 6095–6103.
- [50] D. Del Rio, R. Bastos, U. Sedran, Commercial additives for sulfur control in FCC gasoline: Overall analysis of their impact on LCO and gasoline, *Catal. Today*. 213 (2013) 206–210.

- [51] M. Al-Sabawi, H. de Lasa, Modeling thermal and catalytic conversion of decalin under industrial FCC operating conditions, *Chem. Eng. Sci.* 65 (2010) 626–644.
- [52] M.M. Hossain, M.R. Quddus, H.I. de Lasa, Reduction Kinetics of La Modified NiO/La- γ -Al₂O₃ Oxygen Carrier for Chemical-Looping Combustion, *Ind. Eng. Chem. Res.* 49 (2010) 11009–11017.
- [53] E. Salaices, B. Serrano, H. de Lasa, Biomass Catalytic Steam Gasification Thermodynamics Analysis and Reaction Experiments in a CREC Riser Simulator, *Ind. Eng. Chem. Res.* 49 (2010) 6834–6844.
- [54] G. de la Puente, A. Ávila, G. Chiovetta, W.P. Martignoni, H.S. Cerqueira, U. Sedran, Adsorption of Hydrocarbons on FCC Catalysts under Reaction Conditions, *Ind. Eng. Chem. Res.* 44 (2005) 3879–3886.
- [55] A. Pekediz, D.W. Kraemer, J. Chabot, H.I. de Lasa, Mixing Patterns in a Novel Riser Simulator, in: *Chem. React. Technol. Environ. Safe React. Prod.*, NATO ASI S, Springer, Dordrecht, 1992: pp. 133–146.
- [56] F. García-Labiano, J. Adánez, L.F. de Diego, P. Gayán, A. Abad, Effect of Pressure on the Behavior of Copper-, Iron-, and Nickel-Based Oxygen Carriers for Chemical-Looping Combustion, *Energy & Fuels*. 20 (2006) 26–33.
- [57] F. Garcia-Labiano, L. De Diego, Reduction and oxidation kinetics of a copper-based oxygen carrier prepared by impregnation for chemical-looping combustion, *Ind. Eng. Chem. Res.* (2004) 8168–8177.
- [58] J. Mazumder, Steam Gasification of Biomass Surrogates: Catalyst Development and Kinetic Modelling, (2014) 1–160.
- [59] J.M. Smith, H.C. Van Ness, M.M. Abbott, *Introduction to Chemical Engineering Thermodynamics*, 2005.
- [60] M.M. Hossain, Chemical-Looping Combustion With Gaseous Fuels: Thermodynamic Parametric Modeling, *Arab. J. Sci. Eng.* 39 (2014) 3415–3421.
- [61] K. Svoboda, G. Slowinski, J. Rogut, D. Baxter, Thermodynamic possibilities and constraints for pure hydrogen production by iron based chemical looping process at lower temperatures, *Energy Convers. Manag.* 48 (2007) 3063–3073.
- [62] I.I. Barin, *Thermochemical Data of Pure Substances*, Wiley-VCH Verlag GmbH, Weinheim, Germany, 1995.

- [63] A. Abad, J. Adánez, F. García-Labiano, L.F. de Diego, P. Gayán, J. Celaya, Mapping of the range of operational conditions for Cu-, Fe-, and Ni-based oxygen carriers in chemical-looping combustion, *Chem. Eng. Sci.* 62 (2007) 533–549.
- [64] A. Abad, F. García-Labiano, L.F. de Diego, P. Gayán, J. Adánez, Reduction Kinetics of Cu-, Ni-, and Fe-Based Oxygen Carriers Using Syngas ($\text{CO} + \text{H}_2$) for Chemical-Looping Combustion, *Energy & Fuels*. 21 (2007) 1843–1853.
- [65] M.M. Hossain, H.I. de Lasa, Reduction and oxidation kinetics of Co-Ni/ Al_2O_3 oxygen carrier involved in a chemical-looping combustion cycles, *Chem. Eng. Sci.* 65 (2010) 98–106.
- [66] B. Moghtaderi, H. Song, Reduction properties of physically mixed metallic oxide oxygen carriers in chemical looping combustion, *Energy and Fuels*. 24 (2010) 5359–5368.
- [67] I. Iliuta, R. Tahoces, G.S. Patience, S. Riffart, F. Luck, Chemical-looping combustion process: Kinetics and mathematical modeling, *AIChE J.* 56 (2010) 1063–1079.
- [68] A. Abad, A., G.-L. Juan, de D. F., G. L. F., K. P., A. P., T. Pröll, CLC Modeling the fuel reactor at fast fluidization - Conversion of CH_4 using a NiO-based oxygen carrier in a 12 kWth unit, in: 1st Int. Conf. Chem. Looping, Lyon, Fr., 2010.
- [69] C. Dueso, M. Ortiz, A. Abad, F. García-Labiano, L.F. de Diego, P. Gayán, J. Adánez, Reduction and oxidation kinetics of nickel-based oxygen-carriers for chemical-looping combustion and chemical-looping reforming, *Chem. Eng. J.* (2012).
- [70] M. Trueba, S.P. Trasatti, γ -alumina as a support for catalysts: A review of fundamental aspects, *Eur. J. Inorg. Chem.* (2005) 3393–3403.
- [71] R. Villa, C. Cristiani, G. Groppi, L. Lietti, P. Forzatti, U. Cornaro, S. Rossini, Ni based mixed oxide materials for CH_4 oxidation under redox cycle conditions, *J. Mol. Catal. A Chem.* (2003).
- [72] A. Khawam, D.R. Flanagan, Solid-state kinetic models: Basics and mathematical fundamentals, *J. Phys. Chem. B.* 110 (2006) 17315–17328.
- [73] Z. Zhou, L. Han, G.M. Bollas, Kinetics of NiO reduction by H_2 and Ni oxidation at conditions relevant to chemical-looping combustion and reforming, *Int. J. Hydrogen Energy*. 39 (2014) 8535–8556.
- [74] K. V. Manukyan, A.G. Avetisyan, C.E. Shuck, H.A. Chatilyan, S. Rouvimov, S.L. Kharatyan, A.S. Mukasyan, Nickel Oxide Reduction by Hydrogen: Kinetics and Structural

- Transformations, *J. Phys. Chem. C*. 119 (2015) 16131–16138.
- [75] X. Dai, J. Cheng, Z. Li, M. Liu, Y. Ma, X. Zhang, Reduction kinetics of lanthanum ferrite perovskite for the production of synthesis gas by chemical-looping methane reforming, *Chem. Eng. Sci.* 153 (2016) 236–245.
- [76] V. V. Boldyrev, Topochemistry of thermal decompositions of solids, *Thermochim. Acta.* (1986).
- [77] A.K. Burnham, R.K. Weese, B.L. Weeks, A distributed activation energy model of thermodynamically inhibited nucleation and growth reactions and its application to the β – δ phase transition of HMX, *J. Phys. Chem. B.* (2004).
- [78] M.A. Brown, Market failures and barriers as a basis for clean energy policies, *Energy Policy.* (2001).
- [79] M.A. Hamilton, K.J. Whitty, J.S. Lighty, Numerical Simulation Comparison of Two Reactor Configurations for Chemical Looping Combustion and Chemical Looping With Oxygen Uncoupling, *J. Energy Resour. Technol.* 138 (2016) 042213.
- [80] J. Jung, I.K. Gamwo, Multiphase CFD-based models for chemical looping combustion process: Fuel reactor modeling, *Powder Technol.* 183 (2008) 401–409.
- [81] A.S. Cloete S., Johanse ST., Multiphase CFD-based models for a chemical looping combustion process., in: *Proc. 1st Int Conf Chem. Looping*, Lyon, France, 2010.
- [82] K. Mahalatkar, J. Kuhlman, E.D. Huckaby, T. O’Brien, Computational fluid dynamic simulations of chemical looping fuel reactors utilizing gaseous fuels, *Chem. Eng. Sci.* (2011).
- [83] J.M. Parker, CFD model for the simulation of chemical looping combustion, *Powder Technol.* 265 (2014) 47–53.
- [84] M.J. Andrews, P.J. O’Rourke, The multiphase particle-in-cell (MP-PIC) method for dense particulate flows, *Int. J. Multiph. Flow.* (1996).
- [85] D.M. Snider, P.J. O’Rourke, M.J. Andrews, Sediment flow in inclined vessels calculated using a multiphase particle-in-cell model for dense particle flows, *Int. J. Multiph. Flow.* (1998).
- [86] P.J. O’Rourke, P. (Pinghua) Zhao, D. Snider, A model for collisional exchange in gas/liquid/solid fluidized beds, *Chem. Eng. Sci.* (2009).
- [87] A. Lanza, H. de Lasa, Scaling-up down flow reactors. CPFD simulations and model

- validation, *Comput. Chem. Eng.* 101 (2017) 226–242.
- [88] D.G. Mustard, C.H. Bartholomew, Determination of Metal Crystallite Supported Size and Morphology Supported Nickel Catalysts, *J. Catal.* 67 (1981) 186–206.
 - [89] H. Zhang, R. Xiao, D. Wang, Z. Zhong, M. Song, Q. Pan, G. He, Catalytic Fast Pyrolysis of Biomass in a Fluidized Bed with Fresh and Spent Fluidized Catalytic Cracking (FCC) Catalysts, *Energy & Fuels*. 23 (2009) 6199–6206.
 - [90] D. Geldart, Types of gas fluidization, *Powder Technol.* 7 (1973) 285–292.
 - [91] J.A. Alfaro-Ayala, V. Ayala-Ramírez, A. Gallegos-Muñoz, A.R. Uribe-Ramírez, Optimal location of axial impellers in a stirred tank applying evolutionary programming and CFD, *Chem. Eng. Res. Des.* 100 (2015) 203–211.
 - [92] D.A. Deglon, C.J. Meyer, CFD modelling of stirred tanks: Numerical considerations, *Miner. Eng.* 19 (2006) 1059–1068.
 - [93] Y.N. Chiu, J. Naser, K.F. Ngian, K.C. Pratt, Computation of the flow and reactive mixing in dual-Rushton ethoxylation reactor, *Chem. Eng. Process. Process Intensif.* 48 (2009) 977–987.
 - [94] W.P. Jones, B.E. Launder, The prediction of laminarization with a two-equation model of turbulence, *Int. J. Heat Mass Transf.* 15 (1972) 301–314.
 - [95] Y. Guan, J. Chang, K. Zhang, B. Wang, Q. Sun, Three-dimensional CFD simulation of hydrodynamics in an interconnected fluidized bed for chemical looping combustion, *Powder Technol.* 268 (2014) 316–328.
 - [96] B.E. Launder, D.B. Spalding, The numerical computation of turbulent flows, *Comput. Methods Appl. Mech. Eng.* 3 (1974) 269–289.
 - [97] J. Bredberg, On the Wall Boundary Condition for Turbulence Models, Intern. Rep. 00/4 Dep. Thermo Fluid Dyn. CHALMERS Univ. Technol. Goteborg, Sweden. (2000) 25.
 - [98] D.M. Hargreaves, N.G. Wright, On the use of the k - ϵ model in commercial CFD software to model the neutral atmospheric boundary layer, *J. Wind Eng. Ind. Aerodyn.* 95 (2007) 355–369.
 - [99] X. Feng, J. Cheng, X. Li, C. Yang, Z.S. Mao, Numerical simulation of turbulent flow in a baffled stirred tank with an explicit algebraic stress model, *Chem. Eng. Sci.* 69 (2012) 30–44.
 - [100] J. Gimbut, C.D. Rielly, Z.K. Nagy, J.J. Derksen, Detached eddy simulation on the

- turbulent flow in a stirred tank, *AIChE J.* 58 (2012) 3224–3241.
- [101] C.P. Fonte, B.S. Pinho, V. Santos-Moreau, J.C.B. Lopes, Prediction of the Induced Gas Flow Rate from a Self-Inducing Impeller with CFD, *Chem. Eng. Technol.* 37 (2014) 571–579.
- [102] B. Blocken, T. Stathopoulos, J. Carmeliet, CFD simulation of the atmospheric boundary layer: wall function problems, 41 (2007) 238–252.
- [103] G. Li, X. Yang, H. Ye, CFD simulation of shear flow and mixing in a Taylor-Couette reactor with variable cross-section inner cylinders, *Powder Technol.* 280 (2015) 53–66.
- [104] A. Corsini, G. Delibra, A.G. Sheard, *A Critical Review of Computational Methods and Their Application in Industrial Fan Design*, 2013 (2013).
- [105] R. Courant, Variational methods for the solution of problems of equilibrium and vibrations, *Bull. Am. Math. Soc.* 49 (1943) 1–24.
- [106] A. Hrennikoff, Solution of Problems of Elasticity by the Frame-Work Method, *Appl. Sci. Res.* A8 (1941) 169–175.
- [107] Y. Saad, M.H. Schultz, GMRES: A Generalized Minimal Residual Algorithm for Solving Nonsymmetric Linear Systems, *SIAM J. Sci. Stat. Comput.* 7 (1986) 856–869.
- [108] S. Al-Ghamdi, M. Volpe, M.M. Hossain, H. de Lasa, VO_x/c-Al₂O₃ catalyst for oxidative dehydrogenation of ethane to ethylene: Desorption kinetics and catalytic activity, *Appl. Catal. A Gen.* 450 (2013) 120–130.
- [109] C. Li, Y.W. Chen, Temperature-programmed-reduction studies of nickel oxide/alumina catalysts: effects of the preparation method, *Thermochim. Acta.* 256 (1995) 457–465.
- [110] A. Antzara, E. Heracleous, L. Silvester, D.B. Bukur, A.A. Lemonidou, Activity study of NiO-based oxygen carriers in chemical looping steam methane reforming, *Catal. Today.* 272 (2016) 32–41.
- [111] K.S.W. Sing, Reporting physisorption data for gas/solid systems with special reference to the determination of surface area and porosity (Recommendations 1984), *Pure Appl. Chem.* 57 (1985) 603–619.
- [112] M. Thommes, K. Kaneko, A. V. Neimark, J.P. Olivier, F. Rodriguez-Reinoso, J. Rouquerol, K.S.W. Sing, Physisorption of gases, with special reference to the evaluation of surface area and pore size distribution (IUPAC Technical Report), *Pure Appl. Chem.* 87 (2015) 1051–1069.

- [113] J. Mazumder, H. de Lasa, Fluidizable Ni/La₂O₃- γ -Al₂O₃ catalyst for steam gasification of a cellulosic biomass surrogate, *Appl. Catal. B Environ.* 160–161 (2014) 67–79.
- [114] A.K. Bastos, C. Torres, A. Mazumder, H. de Lasa, CO₂ biomass fluidized gasification: Thermodynamics and reactivity studies, *Can. J. Chem. Eng.* 96 (2018) 2176–2184.
- [115] J. Adánez, C. Dueso, L.F.D. Diego, F. García-Labiano, P. Gayán, A. Abad, Methane combustion in a 500 Wth chemical-looping combustion system using an impregnated Ni-based oxygen carrier, *Energy and Fuels*. 23 (2009) 130–142.
- [116] P. Gayán, L.F. de Diego, F. García-Labiano, J. Adánez, A. Abad, C. Dueso, Effect of support on reactivity and selectivity of Ni-based oxygen carriers for chemical-looping combustion, *Fuel*. 87 (2008) 2641–2650.
- [117] K. Dossumov, G.Y. Yergazieva, L.K. Myltykbaieva, N.A. Asanov, Effect of Co, Ce, and La Oxides as Modifying Additives on the Activity of an NiO/ γ -Al₂O₃ Catalyst in the Oxidation of Methane to Give Synthesis Gas, *Theor. Exp. Chem.* 52 (2016) 119–122.
- [118] B. Wang, R. Yan, D.H. Lee, D.T. Liang, Y. Zheng, H. Zhao, C. Zheng, Thermodynamic Investigation of Carbon Deposition and Sulfur Evolution in Chemical Looping Combustion with Syngas, *Energy & Fuels*. 22 (2008) 1012–1020.
- [119] I. Ahmed, H. de Lasa, Syngas chemical looping combustion using a highly performing fluidizable oxygen carrier, *Catal. Today*. (2019).
- [120] I. Ahmed, S. Rostom, A. Lanza, H. de Lasa, Computational Fluid Dynamics study of the CREC Riser Simulator: Mixing patterns, *Powder Technol.* 316 (2016) 641–649.
- [121] E.N. Fuller, P.D. Schettler, J.C. Giddings, A new method for prediction of binary gas-phase diffusion coefficients, *Ind. Eng. Chem.* (1966).
- [122] E.N. Fuller, K. Ensley, J.C. Giddings, Diffusion of halogenated hydrocarbons in helium. The effect of structure on collision cross sections, *J. Phys. Chem.* (1969).
- [123] P.B. Weisz, C.D. Prater, Interpretation of Measurements in Experimental Catalysis, *Adv. Catal.* (1954).
- [124] H. Fogler, *Elements of chemical reaction engineering*, 1999.
- [125] J. Kanervo, Characterisation of Supported Chromium Oxide Catalysts by Kinetic Analysis of H₂-TPR Data, *J. Catal.* 207 (2002) 57–65.
- [126] A. Tilland, L. Franck-Lacaze, E. Schaer, Kinetic determination of chemical looping combustion reactions in a continuous stirred tank reactor: Reduction of the oxygen carrier,

- Chem. Eng. Sci. 162 (2017) 341–354.
- [127] R.N. Pease, R.S. Cook, Equilibrium in the reaction, $\text{NiO} + \text{H}_2 \rightleftharpoons \text{Ni} + \text{H}_2\text{O}$. The free energy of nickelous oxide, J. Am. Chem. Soc. 48 (1926) 1199–1206.
- [128] J.E. Antill, J.B. Warburton, Oxidation of Nickel by Carbon Dioxide, J. Electrochem. Soc. 114 (1967) 1215–1221.
- [129] T. Mattisson, M. Johansson, A. Lyngfelt, The use of NiO as an oxygen carrier in chemical-looping combustion, Fuel. 85 (2006) 736–747.
- [130] P. Cho, T. Mattisson, A. Lyngfelt, Carbon formation on Nickel and Iron Oxide-Containing Oxygen Carriers for Chemical-Looping Combustion, Ind. Eng. Chem. Res. (2005).
- [131] S.R. Son, S.D. Kim, Chemical-looping combustion with NiO and Fe_2O_3 in a thermobalance and circulating fluidized bed reactor with double loops, in: Ind. Eng. Chem. Res., 2006.
- [132] S.W. Kim, J.Y. Ahn, S.D. Kim, D. Hyun Lee, Heat transfer and bubble characteristics in a fluidized bed with immersed horizontal tube bundle, Int. J. Heat Mass Transf. (2003).
- [133] T.B. Anderson, R. Jackson, Fluid mechanical description of fluidized beds: Equations of Motion, Ind. Eng. Chem. Fundam. 6 (1967) 527–539.
- [134] R. Jackson, The Dynamics of Fluidized Particles, Meas. Sci. Technol. (2001).
- [135] J. Smagorinsky, General Circulation Experiments With the Primitive Equations, Mon. Weather Rev. (1963).
- [136] D.M. Snider, S.M. Clark, P.J. O'Rourke, Eulerian-Lagrangian method for three-dimensional thermal reacting flow with application to coal gasifiers, Chem. Eng. Sci. (2011).
- [137] D. Snider, S. Banerjee, Heterogeneous gas chemistry in the CPFD Eulerian-Lagrangian numerical scheme (ozone decomposition), Powder Technol. (2010).
- [138] P.J. O'Rourke, D.M. Snider, An improved collision damping time for MP-PIC calculations of dense particle flows with applications to polydisperse sedimenting beds and colliding particle jets, Chem. Eng. Sci. (2010).
- [139] R.P. Chhabra, L. Agarwal, N.K. Sinha, Drag on non-spherical particles: An evaluation of available methods, Powder Technol. (1999).
- [140] C.J. Stairmand, The Design and Performance of Cyclone Separators, Trans. Inst. Chem. Eng. (1951).

- [141] M. Koksai, F. Hamdullahpur, Gas mixing in circulating fluidized beds with secondary air injection, *Chem. Eng. Res. Des.* (2004).
- [142] A. Lanza, M.A. Islam, H. de Lasa, Particle clusters and drag coefficients in gas-solid downer units, *Chem. Eng. J.* 200–202 (2012) 439–451.
- [143] G. Guan, C. Fushimi, M. Ishizuka, Y. Nakamura, A. Tsutsumi, S. Matsuda, Y. Suzuki, H. Hatano, Y. Cheng, E.W. Chuan Lim, C.H. Wang, Flow behaviors in the downer of a large-scale triple-bed combined circulating fluidized bed system with high solids mass fluxes, *Chem. Eng. Sci.* (2011).
- [144] L. Cheng, P. Basu, Effect of pressure on loop seal operation for a pressurized circulating fluidized bed, *Powder Technol.* (1999).
- [145] M.M. Yazdanpanah, A. Forret, T. Gauthier, A. Delebarre, An experimental investigation of loop-seal operation in an interconnected circulating fluidized bed system, *Powder Technol.* (2013).
- [146] P. Basu, J. Butler, Studies on the operation of loop-seal in circulating fluidized bed boilers, *Appl. Energy.* (2009).
- [147] Z. Wang, D. Bai, Y. Jin, Hydrodynamics of cocurrent downflow circulating fluidized bed (CDCFB), *Powder Technol.* (1992).
- [148] S. Vaishali, S. Roy, P.L. Mills, Hydrodynamic simulation of gas-solids downflow reactors, *Chem. Eng. Sci.* (2008).
- [149] S. Krol, A. Pekediz, H. De Lasa, Particle clustering in down flow reactors, *Powder Technol.* (2000).

APPENDICES

Appendix A Gas Chromatograph (GC) and Mass Balance

GC Configuration

Table A 1: Gas Chromatograph parameters used to analyze reaction product

Parameters	Properties		
Column (HaySep D 100/120)	Length 9.1m, Film Thickness 2.0 μ m, Inner Diameter 2.0 mm		
Injection Temperature ($^{\circ}$ C)	200		
Flow Control Mode	Flow		
Carrier Gas	Argon		
Total Flow (ml/min)	20		
Purge Flow (ml/min)	3		
Oven Temperature Program	Rate	Temperature	Hold Time
	($^{\circ}$ C/min)	($^{\circ}$ C)	(min)
	-	50	4
	20	200	18.5
	[TCD]	[FID]	
Temperature ($^{\circ}$ C)	200	230	
Makeup Gas	Argon	H ₂	
Makeup Flow (ml/min)	15	15	
Flame	n/a	H ₂ 40ml/min	
		Air 400 ml/min	
Current (mA)	30 (-ve polarity)		n/a
Sample Actuator Program (Relay91)	Time (min)		Value
	0.00		0
	0.01		1
	0.5		0

Figure A 1 is an gas chromatograph example established by injecting 2ml syngas. The syngas contains 50v% H₂, 20v%CO, 10v%CH₄, 20%CO₂.

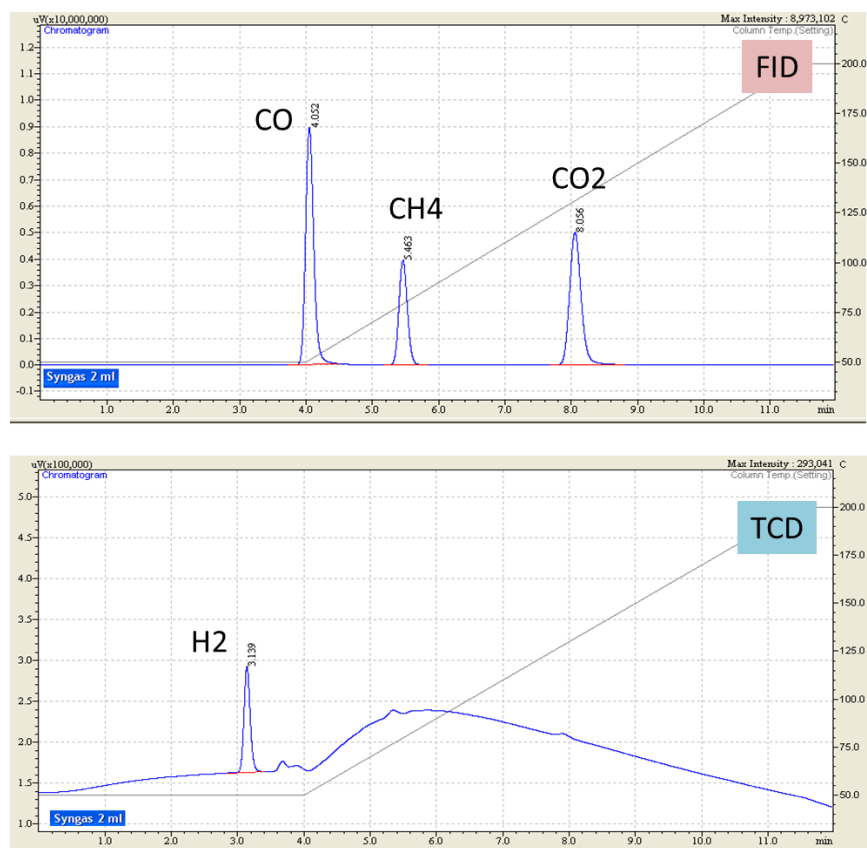


Figure A 1: Typical Gas Chromatograph of a syngas sample

GC Calibration

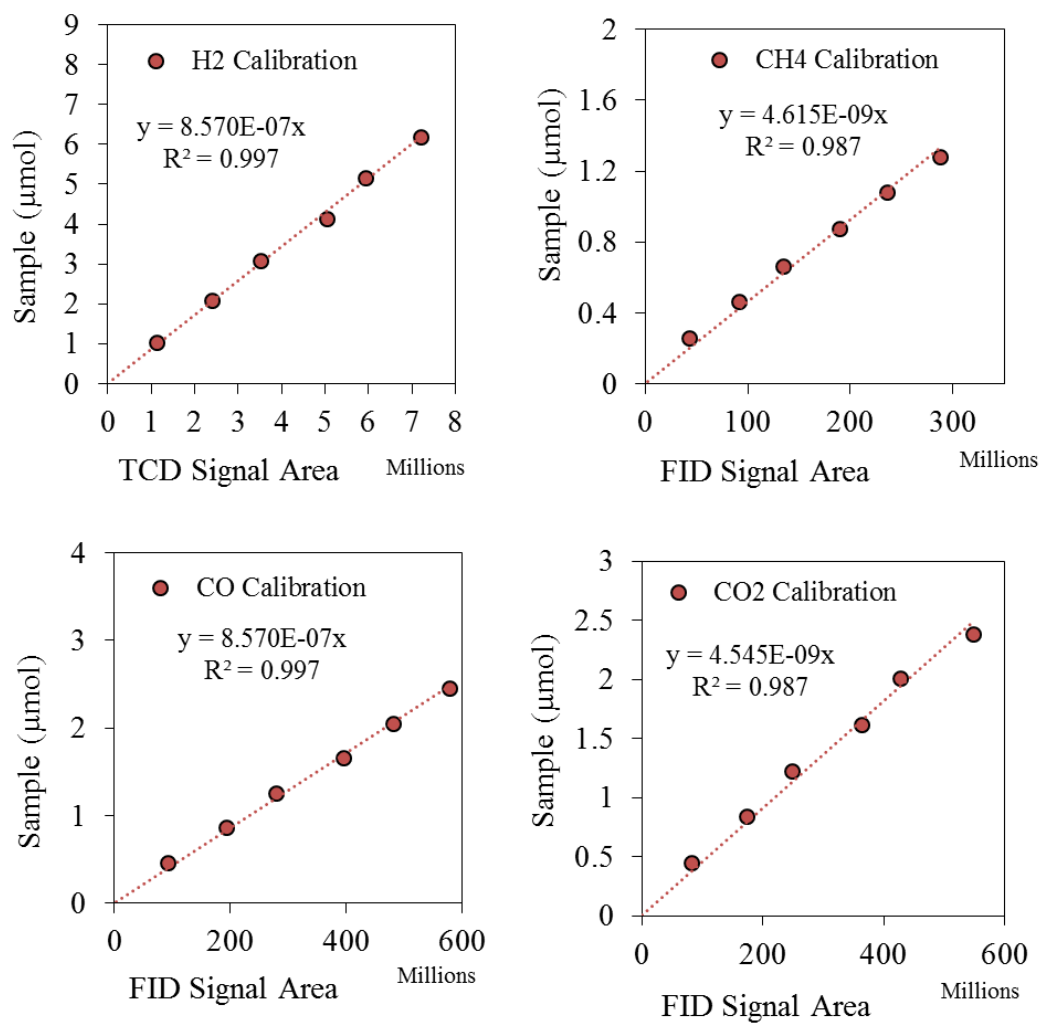


Figure A 2: Gas chromatograph calibration, H₂ is calibrated using TCD and CO, CH₄, CO₂ are calibrated using FID

Mass Balance

$$\text{Amount of feed, } n_{feed}(\mu\text{mol}) = \frac{V_{feed}(cc) \times P_{inj}(\text{psi}) \times 6870.75}{R\left(\frac{J}{\text{mol.K}}\right) \times T_{inj}(K)}$$

where, V_{feed} is gaseous feed volume, R is gas constant, P_{inj} and T_{inj} are pressure and temperature respectively of gas injector which is typically at room temperature and pressure.

$$\text{Initial Argon in reactor, } n_{R-Ar}(\mu\text{mol}) = \frac{V_R(cc) \times P_{iR}(\text{psi}) \times 6870.75}{R\left(\frac{J}{\text{mol.K}}\right) \times T_R(K)}$$

where, V_R is reactor volume, P_{iR} is initial reactor pressure and T_R is reactor temperature

$$\text{Initial Argon in vacuum box, } n_{V-Ar}(\mu\text{mol}) = \frac{V_V(cc) \times P_{iV}(\text{psi}) \times 6870.75}{R\left(\frac{J}{\text{mol.K}}\right) \times T_V(K)}$$

where, V_V is vacuum box volume, P_{iV} is initial vacuum box pressure and T_V is vacuum box temperature.

$$\text{Final gas amount in the reactor, } (n_{R-Ar} + n_{PR})(\mu\text{mol}) = \frac{V_R(cc) \times P_{fR}(\text{psi}) \times 6870.75}{R\left(\frac{J}{\text{mol.K}}\right) \times T_R(K)}$$

where, P_{fR} is final reactor pressure.

$$\text{Product in the reactor, } n_{PR}(\mu\text{mol}) = \frac{V_R(cc) \times (P_{iR} - P_{fR})(\text{psi}) \times 6870.75}{R\left(\frac{J}{\text{mol.K}}\right) \times T_R(K)}$$

$$\text{Total gas amount in the system, } n_T = n_{R-Ar} + n_{PR} + n_{V-Ar}$$

$$\text{Fraction of products in the vacuum box after opening the reactor, } f_P = 1 - \frac{n_{R-Ar} + n_{V-Ar}}{n_T} \text{ Total gas}$$

$$\text{amount in 1 ml sample loop, } n_{ST}(\mu\text{mol}) = \frac{V_s(cc) \times P_{fV}(\text{psi}) \times 6870.75}{R\left(\frac{J}{\text{mol.K}}\right) \times T_s(K)}$$

Where, P_{fV} is final vacuum box pressure, T_s is sample loop temperature which is recommended to keep as same as vacuum box temperature T_V .

$$\text{Product in 1ml sample loop, } n_{Sp}(\mu\text{mol}) = n_{ST} \times f_P$$

$$\text{Amount of "i" compound in reactor product, } n_{PR-Ci}(\mu\text{mol}) = n_{PR} \times \frac{n_{sp-ci}}{n_{sp}}$$

where, n_{sp-ci} is the μmol amount in 1ml sample loop. This data is collected from calibrated GC system.

These calculations are essential to establish material balance and to analyze reaction performance for a certain condition.

Appendix B Oxygen Carrier (OC) Preparation Equipment

Preparation of the OC-Ref and HPOC

Precursor impregnation over the support

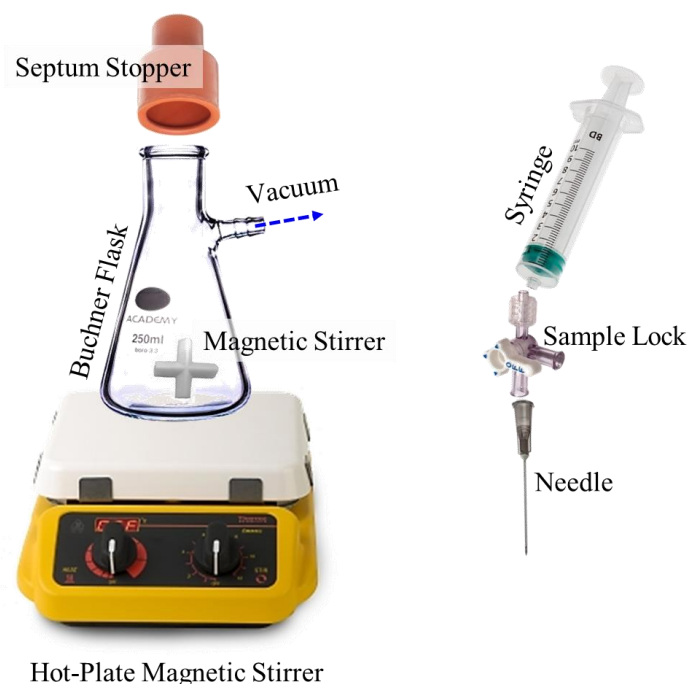


Figure B 1: Necessary equipment for precursor impregnation

A single batch preparation considers 20g γ -alumina in a Buchner flask as presented in Figure B 1. Prior to the metal impregnation, γ -alumina is dried under vacuum condition for at least for 2hr at 200°C to ensure the removal of all water moisture from the γ -alumina pore. Reaching 200°C should follow 5°C/min or less ramp to avoid particle fracture due to sudden evaporation of moisture. The temperature can be controlled using hot-plate magnetic stirrer system.

Once moisture removal is done and the system is at ambient temperature under vacuum condition, it is ready for injection of precursor solution. A sample lock is used in injection syringe system to control the precursor flow as drop wise. Stirring must be continued during the precursor impregnation as if the particle does not get wet. Once the complete precursor is injected it is kept under vacuum for at least 30 min. Sample is collected by equalizing pressure to the atmosphere. The sample is then collected in a ceramic evaporating dish as shown in Figure B 2b and kept in a furnace (Figure B 2a) with drying temperature program as described in CHAPTER 5.

Following drying step, the sample is collected into a small fluidized bed system (Figure B 2c) and installed into the same furnace. Both inlet and outlet of the fluidized bed is kept outside the furnace via the exhaust port. A 10% H₂-Ar and air is flowed via inlet to reduce and calcine respectively at fluidized bed condition. In preparation of OC-Ref, 750°C temperature was used for both reduction and calcination following a certain temperature program.

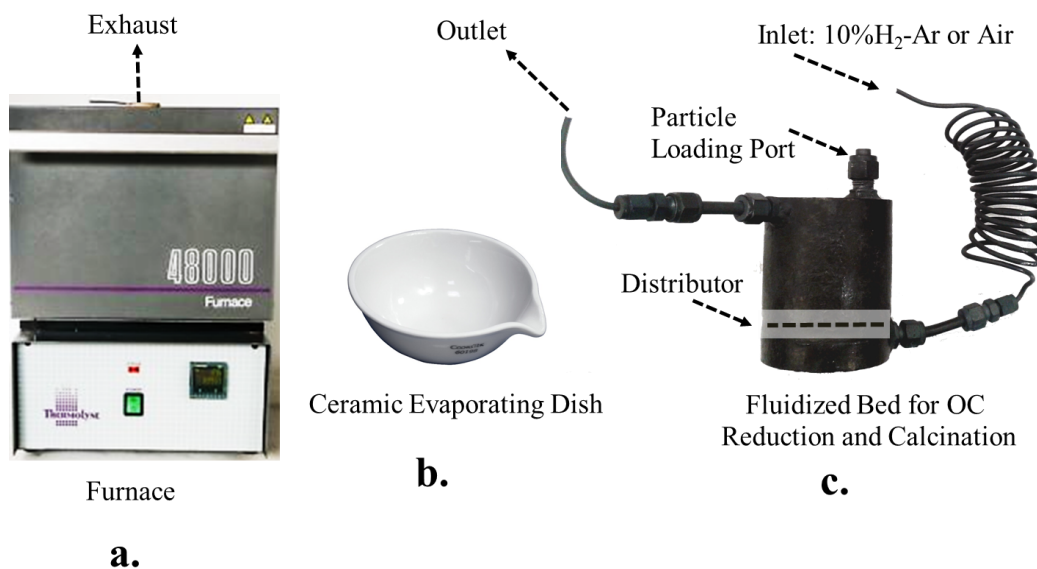


Figure B 2: Equipment used for drying, reduction and calcination steps

Preparation of the HPOC

The OC-Ref is further treated to circumvent the undesirable formation of NiAl₂O₄ in the OC-Ref, additional treatment steps were implemented in the present study as follows: a) the OC was further treated in a tube furnace (Thermolyne 21100) with 10% H₂ balanced with Ar, b) the temperature

of the furnace was increased using a 15°C/min ramp b) once 900°C reached, this temperature was kept for 1h, c) the resulting OC was calcined at 650°C.

Figure B 3 depicts an appearance of OC-Ref and HPOC. After the treatment to reduce nickel aluminate, the HPOC pigment appears as green olive where OC-Ref pigment was blue.

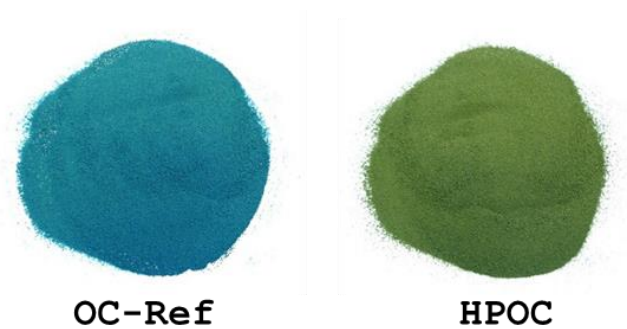


Figure B 3: Appearance of OC-Ref and HPOC after preparation

CURRICULUM VITAE

IMTIAZ AHMED

EDUCATION

Ph.D. in Chemical Engineering

Jan 2015 - Jan 2019

University of Western Ontario, London, ON, Canada

- *Dissertation:* Develop a highly reactive and recyclable heterogeneous oxygen carrier for complete combustion of syngas via Chemical Looping technology and assess performance thereof in industrial scale.
- *Award:* Western Graduate Research Scholarship (WGRS)

B. Sc. in Chemical Engineering

Jun 2007 - Mar 2012

Bangladesh University of Engineering and Technology (BUET), Dhaka, Bangladesh

- *Dissertation:* Design a data acquisition software and PID controller to regulate multiple interacting heating processes using Decoupler technique and construct a hardware interface to communicate with the software.
- *Project:* Construct a heat and mass balance model for crude oil refining process using Aspen-HYSYS software to maximize diesel and kerosene production and design the major infrastructure equipment including PFD and P&ID.
- *Award:* Bangladesh Government Technical Scholarship

RESEARCH EXPERIENCE

Research Assistant | University of Western Ontario, London, ON, Canada Jan 2015 - Jan 2019

- Constructed a thermodynamic model using Matlab and Aspen-Plus to study the theoretical limits of syngas combustion.
- Developed a computational fluid dynamics of CREC Riser Simulator reactor using COMSOL-CFD to predict efficiency of gas-solid mixing patterns during reaction that eliminated experimental uncertainty of a reaction. Findings were published in a scientific journal.
- Synthesized and investigated oxygen carrier materials by following hypotheses and characterizations (i.e. BET surface area, TPR/TPO, Pulse-Chemisorption and XRD). Discovered a

novel synthesis technique and developed a Highly Performing Oxygen Carrier (HPOC) featured with high reactivity at lower temperature and strong recyclability.

- Performed numerous syngas combustion reactions using the HPOC and analyzed efficiency using parametric optimization. Eventually achieved over 92% CO₂ yield, which enables subsequent sequestration industrially viable and cost-effective.
- Investigated reaction mechanism and constructed kinetic model, evaluated industrial scale performances using CPFD-Barracuda. These permits to optimize process operation, design reactor, avoid risks and circumvent unnecessary costs.

PROFESSIONAL EXPERIENCE

Research Engineer | RECAT Technologies Inc., London, ON, Canada **Jan 2018 - Apr 2018**

- Provided hands on training to a group lead researchers of SABIC R&D, Riyadh, KSA regarding the operation of CREC Riser Simulator reactor and catalyst evaluation techniques.
- Guided to establish Gas Chromatogram method and FID-TCD calibration to enable accurate analysis of hydrocarbon products.
- Delivered impromptu support to client team members within limited timeline regarding temperature control tuning, spare parts installation and mass balance calculation. Analyzed operations manuals and coordinated with team members to determine further action plans.

Graduate Teaching Assistant | University of Western Ontario, Canada **Sep 2015 - Dec 2018**

- Delivered lectures and tutorials to numerous under-graduate level students. Assisted the students to solve research problems and evaluated lab reports. Was nominated for Graduate TA Award for outstanding contribution.
- Course Expertise: Chemical Process Simulation (Aspen-HYSYS), Process Dynamics and Control Lab, Computational Method for Engineers (MATLAB)

Chemical Process Engineer | ZICOM Equipment Pte Ltd., Bangladesh **Jun 2012 - Nov 2014**

20 MMSCFD Natural Gas TEG (Triethylene Glycol) Dehydration Plant | BAPEx, Bangladesh

- Developed Heat and Mass Balance model using Aspen-HYSYS software to determine and optimize process operation and overall cost structure. Reviewed entire process PFD and P&ID to improve performances of facilities. Coordinated with plant manager and other functional department managers for timely completion.

- Designed plant equipment according to codes and industrial practices such as API, ASME, and TEMA. Coordinated proactively with the vendor that facilitated timely completion of the project.
- Received employer sponsored training on Hazard and Operability (HAZOP) Method at GT Consultancy, Singapore. Reviewed technical documents regarding Standard Operational Procedure (SOP), HAZOP and Hazard Identification (HAZID) that enabled client's engineering team to operate the plant safely.

1250 BPD Condensate Fractionation Plant | SGFL-Petrobangla, Bangladesh

- Coordinated with a team of cross-departmental engineers responsible for plant startup & commissioning. Monitored process operations to identify and resolve technical problems. Subsequently handed over the project after ensuring optimum production level within stipulated timeline.
- Initiated and completed the development of user interface (i.e. Allen-Bredly PLC & HMI) of the process control system due to lack of available expertise. Directly contributed to save \$4000 CAD worth of consultancy expenses and 3 weeks of lead time.

PUBLICATION | CONFERENCE

-
- *Journal*: **I. Ahmed**, H. de Lasa, "Syngas Chemical Looping Combustion using a Highly Performing Fluidizable Oxygen Carrier", **Catalysis Today**, **2019** | *Conference*: **ISCRE25**, Florence, Italy, May 20-23, 2018.
 - *Journal*: **I. Ahmed**, H. de Lasa, "Kinetic Model for the Syngas Chemical Looping Combustion using Nickel-Based Highly Performing Fluidizable Oxygen Carrier", **Industrial & Engineering Chemistry Research**, **2019**.
 - *Conference*: **I. Ahmed**, S. Rostom, H. de Lasa, "Chemical Looping Combustion (CLC) of Biomass Derived Syngas using a Fluidizable Ni-Co-La/ γ -Al₂O₃ Oxygen Carrier: CLC Performance and CPFD Modelling. **AIChE2018**, Pittsburgh, PA, US, Oct 28-Nov 02, 2018.
 - *Journal*: **I. Ahmed**, S. Rostom, A. Lanza, H. de Lasa, "Computational Fluid Dynamics study of the CREC Riser Simulator: Mixing patterns", **Powder Technology**, **2017** | *Conference*: **Fluidization XV**, Quebec, Canada, May 22-27, 2016.